RICE UNIVERSITY

Carbon Nanotube Characterization and Processing-Structure-Property Relationships of Solution Spun Fibers for Electronic Clothing

By

Lauren Whitney Taylor

A THESIS SUBMITTED
IN PARTIAL FULFILLMENT OF THE
REQUIREMENTS FOR THE DEGREE

Doctor of Philosophy

APPROVED, THESIS COMMITTEE

Matteo Pasquali

A.J. Hartsook Professor and Professor of Chemical
and Biomolecular Engineering, Chemistry, and
Materials Science and Nanoengineering

Glen C. Irvin Jr. (Jul 16, 2021 07:45 CDT)

Glen Irvin, Jr.

Research Professor of Chemical and
Biomolecular Engineering

Sibani Lisa Biswal

Associate Dean for Faculty Development,
William M. McCardell Professor in Chemical
Engineering, and Professor of Materials
Science and NanoEngineering

Douglas Natelson

Professor and Department Chair of Physics
and Astronomy

HOUSTON, TEXAS

July 2021

RICE UNIVERSITY

Carbon Nanotube Characterization and Processing–Structure–Property Relationships of Solution Spun Fibers for Electronic Clothing

by

Lauren Whitney Taylor

A Thesis Submitted
in Partial Fulfillment of the
Requirements for the Degree

Doctor of Philosophy

Approved, Thesis Committee:

_____

Matteo Pasquali, Chair
Professor of Chemical and Biomolecular
Engineering

_____

Lisa Biswal
Professor of Chemical and Biomolecular
Engineering

_____

Douglas Natelson
Professor of Physics and Astronomy

_____

Glen C. Irvin Jr.
Research Professor of Chemical and
Biomolecular Engineering

Houston, Texas

June, 2021

ABSTRACT

Carbon Nanotube Characterization and Processing–Structure–Property
Relationships of Solution Spun Fibers for Electronic Clothing

by

Lauren Whitney Taylor

Carbon nanotubes (CNTs) have excellent mechanical strength, thermal conductivity, and electrical conductivity [1–5]. These properties make them particularly interesting for high performance fiber applications such as lightweight cables and wires, soft biological implants, next generation ballistic protection, and wearable electronics. Initial efforts to develop strong and conductive CNT fibers were slow due to limited CNT production and lack of a suitable solvent due to the strong van der Waals forces between CNTs. However, significant progress in CNT fiber production came from the development of gram-quantity synthesis from the high pressure carbon monoxide (HiPCO) growth process and demonstration of CNT fiber spinning with superacid solvents [6,7]. Since these developments in the early 2000's, tensile strength and electrical conductivity of CNT fibers have increased on average $\sim 20\%$ per year. Research conducted in this thesis has continued this trend and produced CNT fibers with a tensile strength of 4.2 GPa and an electrical conductivity of 10.9 MS/m. These properties are now competitive with high strength fibers such as carbon fiber and aramid fibers as well as metal conductors where weight savings, flexibility, or thermal conductivity are important parameters. To improve CNT fiber performance, this thesis studied the purification of CNTs for improved solubility in chlorosulfonic (CSA), and

the effect of CNT characteristics on fiber performance. This work demonstrates that CNTs with fewer impurities produce fiber with higher electrical conductivity. However, more intense purification (furnace oxidation) decreases the aspect ratio (length of the CNT/diameter of the CNT) which decreases both tensile strength and conductivity. Therefore, purification conditions must be carefully considered to optimize fiber properties. Furthermore, it was found that lower CNT concentration in the spin dope increased tensile strength of CNT fibers. This enhancement in strength is believed to be the result of improved CNT bundle structure within the fiber. Additional improvements in strength and electrical conductivity were also achieved by decreasing the angle of the inlet cone of the spinneret. This result suggests that fiber properties could be further improved by increasing the path length of the spinneret to allow for additional stress relaxation of the solution before coagulation. Finally, this thesis demonstrates that CNT fibers can used as wearable, textile electrodes. CNT fibers were plied into thread and sewn with a standard sewing machine into textiles to form soft electrodes. These electrodes were able to obtain high quality electrocardiograms (EKGs) on par with commercial wet electrodes. Furthermore, we show that CNT fiber can also be used as transmission lines to carry signal from the recording site to standard electronic components. These results demonstrate that CNT fiber is the ideal material for wearable electronics because it is conductive, soft, washable, and easy to integrate into clothing.
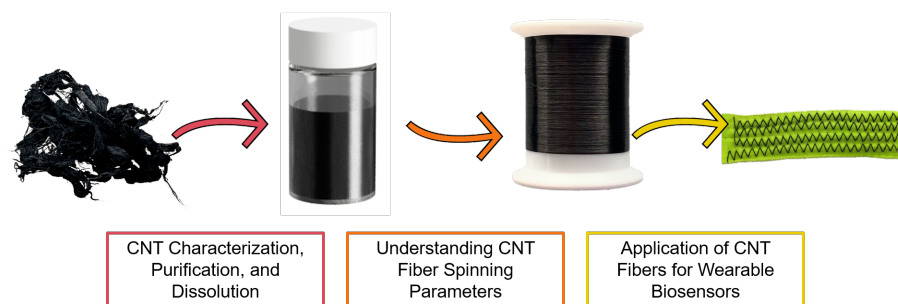

Figure 1 : Graphical abstract of this thesis.

Acknowledgments

There are many people I would like to thank for their help, support, and guidance in the completion of this thesis. First, I would like to thank Matteo for being a wonderful advisor for the past 7 years. Thank you for allowing me to be creative and pursue my own ideas; I also appreciate all of your encouragement when I have doubted myself. Thank you trusting me to fill in for you at conferences and funding events. Although these events always made me nervous because I had big shoes to fill, I learned so much and the experiences were invaluable to me. (I also got to pet a Koala!) Secondly, I would like to thank Glen for his unwavering support of me and the entire lab. At a conference, an attendee told you that he liked my talk and proceeded to call me delicate. Without missing a beat you corrected him and said, "you mean strong and intelligent." This truly meant so much to me, and I will always cherish this memory. Thirdly, I would like to thanks Lisa Biswal and Doug Natelson. Thank you so much for your guidance and serving on my thesis committee.

Next, I would like to acknowledge all of my amazing labmates over the years! Most people don't describe grad school as "fun", but working with you guys filled each day with something to smile about. I loved our Fridays (and other days of the week) at Valhalla chatting over a beer, our "Pasquali lab cult" lunches that sometimes ran too long, our pracrasta–starbucks larks (PSLs) to get coffee and enjoy nice weather, our annual activities such as beach day and the ugly holiday sweater party, our complex chalkboard of not–so complex drawings, our group dinners where I always seem to laugh until I cry, and our new activity of brewery biking.

I would like to first thank my past labmates. A big thanks to Francesca Mirri for taking me under your wing when I joined the lab; I would have been so lost without

you! I will always cherish our tea time with Vida Jamali and Shaghayegh Agah. I was so lucky to have three intelligent, and thoughtful female mentors. An extra thank you to Vida - you have continued to be such a great mentor to me even after graduating. Thank you for always being there for me. I would like to thank Flavia Vitale for her help and guidance throughout my PhD. You have also been such an amazing leader to me. I would like to thank Robby Headrick for being such a valuable resource (especially on Raman) and for continuing to be a dear friend after you left. I'm thankful for your friendship! I'm sorry Oliver and I made you miserable during our trip to the conferences in Spain. Thank you to Emily Yedinak for being someone I could always commiserate with and for decorating the office with llamas. I'm looking forward to meeting up with you on the east coast! I would also like to thank Stephen Yan for his friendship; I'm sorry I took your desk when I first joined the lab. I didn't know! I'm also sorry that you had to switch desks so often, but I enjoyed all the time we spent chatting when you had the desk next to me. Thank you also to Amram Bengio, Dmitri Tsentalovich, Colin Young, Mohammed Adnan, Dan Marincel, and Robert Pinnick for being wonderful senior graduate students and postdocs.

Thank you to my current labmates! Thank you to Zhao Tang for being such a kind officemate for many years. Steven Williams (Cat Steve), thank you for being my EKG model, for helping me troubleshot issues, and for our work with "frog and spiders productions." I would also like to thank my current officemates and ferrocene fairies, Arthur Sloan and Muxiao Li. I appreciate you guys letting me warm up by the reactor. Additionally, thank you Arthur for the office alpacas. Mine will move to my new office with me. Sushma Sri Pamulapati, I'm so happy we joined the Pasquali lab together. Thank you for always greeting me with a warm smile, making me a delicious cake on my birthday, and your all around thoughtfulness. Thank you to the baby spiders, Ivan Rosa de Siqueira and Michelle Durán–Chaves. You guys have been such a joy to work with, and I know you are going to do great things! Cedric Ginestra, Thank you for putting up with me! If there is ever a problem in the lab, you are

always ready and willing to solve it; thank you for your determination and ingenuity. Mitchell Trafford, thank you for being a great Linden, extentional rheometer, and glovebox dad even when you don't want to be. You are always there to lend a helping hand, and I really appreciate it! Thanks, to our current postdocs, Clayton Kacica and Jesus Acapulco, for your leadership, research ideas, and embracing our wacky lab family. Last but certainly not least, I'd like to thank my partner in crime, Oliver Dewey. I could not have asked for a better collaborator, undergraduate co-parent, and friend over the past 6 years! From our chats at Phoebe the fume hood and trip to Swagelok during the start of our PhDs to our many, many, many spinning experiments, I cannot imagine my graduate school experience without you. My one regret is that we can't travel for science together. I'm sorry you got food poisoning in Spain and your car exploded on I-45 on our way home UT Dallas. I truly hope our "future outlook" in the *International Fiber Journal* comes to fruition, and we meet up at many confrences as professors to reminisce about graduate school together.

For my final academic acknowledgments, I'd like to thank my undergraduate students and collaborators. Thank you to my REU students, Tammy Hendrix-Doucette and Jamie John G Manaay, my RET, Karla Rosa, and my Rice undergraduates, David "Doodles" Zhou, Ray Wang, Katy Gehring, Sam Fowler, and Raidah Ahmed. Thank you to my wonderful collaborators: Paul Butler (NIST), Lucy Liberman (Technion – Israel Institute of Technology), Asia Matatyaho-Yaakobi (Technion – Israel Institute of Technology), Ishi Talmon (Technion – Israel Institute of Technology), Andrew Sharit (AFRL), and Benji Maruyama (AFRL). You all have been so valuable and helpful towards reaching my research goals.

Finally, I would like to thank my friends and family. Thank you to my wonderful husband, Collin. Thank you for loving me and supporting my dreams. I'm so lucky to have such a kind and generous partner. I'm excited for the next chapter in our lives. I would also like to thank my sweet dog, Millie, for bringing a little bit of extra joy in each day – especially during a tough 2020. Thank you to my best friend, Paige,

for always being there for me even though we live far apart. Lastly, I would like to thank my mom and dad. Thank you for supporting all of my endeavors, encouraging me to do my best, and loving me unconditionally.

Contents

Illustrations

Tables

Chapter 1

Introduction

Since their discovery in 1991, carbon nanotubes (CNTs) have been extensively studied due to their exceptional mechanical strength, thermal conductivity and electrical conductivity [1–5]. This unique combination of properties makes them highly desirable for high performance fiber applications such as lightweight wires and cables, high efficiency electric motors, soft biological implants, next generation ballistic protection, and wearable electronics. However, it took almost 10 years after the discovery of CNTs to produce the first CNT fibers [8]. The slow progress on CNT macromaterials stemmed from two problems: First, there was poor understanding of CNT growth which limited production [9]. Second, CNTs bundle tightly together due to strong van der Waals forces meaning that CNTs do not dissolve in traditional solvents such as water or organics. By 2004, three methods for fiber production were introduced. The most common fiber production method is direct spinning from floating-catalyst chemical vapor deposition (FCCVD) CNT growth reactors [10]. In this process, large quantities of CNTs are grown so that an aerogel is formed in the reactor. The aerogel is pulled from the reactor and densified to form a fiber. The second production method is array spinning which grows vertically aligned CNTs on supported catalyst [10]. The aligned CNTs can be pulled away from the support causing the CNTs to bundle and form a fiber. Both of these methods are solid state approaches that are similar to the production of textiles such as cotton or wool. The third method is a solution spinning technique [7, 11, 12]. In this process, CNTs are dissolved in

superacid, the only true solvent for CNTs [13, 14], and extruded through a spinneret into a coagulation bath. The acid diffuses away from the liquid filament and the CNTs bundle together via van der Waals forces to form a stable fiber. This process is similar to the production method for high performance fibers such as carbon fiber, Kevlar® and other aramid fibers, and Dyneema®.

This thesis focuses on the production and application of CNT fiber produced with the solution spinning method due to several key advantages over solid state spinning approaches. First, the solution spinning process is easily scaled up. To increase throughput of fiber, the number of holes in the spinneret can be increased [11]. On the other hand, direct spinning methods can only produce a single filament of fiber per FCCVD reactor. Furthermore, the solution spinning method is able to produce more densely packed and better aligned fibers which improves the electrical conductivity and Young's modulus of the fibers. Finally, CNTs are purified before solution spinning to remove amorphous carbon and residual catalyst. High purity CNTs, in combination with residual acid in the fiber from the spinning process, results in fibers that are significantly more conductive than direct spun fibers.

Chapter 3 of this thesis discusses purification of CNTs for improving solubility of CNTs in chlorosulfonic acid (CSA). Most as produced CNTs do not dissolve into CSA due to the presence of impurities during the growth process. These impurities include catalyst and carbon impurities often referred to as amorphous carbon. Here, we discuss the mechanism behind the improved solubility of purified CNTs and how the purification method affects CNT aspect ratio (length of the CNT/diameter of the CNT).

Chapter 4 discusses the improvement of CNT fiber properties as a result of this thesis and puts the progress of CNT fibers properties in the broader context of the

field. Since the first production of continuous CNT fibers over 20 years ago, the field has made steady progress toward macroscopic articles with the properties of individual CNTs. Tensile strength and electrical conductivity of solution spun fibers have improved an average of $\sim$20% per year. However, CNT fibers from all production methods are continuing to improve in properties, and CNT production by corporations is growing quickly and rapidly dropping in price. Enhanced collaboration from academic, government, and industrial partners is essential for accelerating advancements to low material cost to enable broad adoption of CNT fibers in a wide array of applications. Chapter 5 explores key solution spinning processing parameters towards continuing to improve fiber properties and process efficiency. These parameters include post-processing methods, choice of coagulant, CNT purity, CNT aspect ratio, spinneret geometry, and concentration of CNTs in the spin dope.

Finally, in Chapter 6 we demonstrate that CNT fiber can be used as EKG sensors and signal wires in clothing. Current wearable technology is limited to accessories such as watches and glasses due to the difficulty of interfacing soft textiles with rigid electronic components. CNT fiber is the ideal material for this application because it is soft like cotton thread but has the electrical conductivity of metals. By sewing CNT fiber into athletic shirts with a standard sewing machine, we can obtain electrocardiograms that perform similar to commercial, wet electrodes using off the shelf devices. These results pave the way for further innovation in wearable technology and electronic textiles because devices such as fiber antennas [15], semiconductors [16], and light emitting diodes [17] can be combined to create advanced devices and interfaces.

Chapter 2

Background on Carbon Nanotubes

2.1 Properties of Carbon Nanotubes

In 1991, Sumio Iijima discovered carbon nanotubes (CNTs) which sparked the interest of the scientific community due to the outstanding combination of thermal, electrical, and mechncial properties [1–5, 18]. The thermal conductivity of CNTs is over 2000 W/mK and the electrical conductivity is ∼100 MS/m [19]. Additionally, the Young's modulus is ∼1 TPa, and the breaking strength is ∼100 GPa [3, 20]. These properties make CNTs of great interest as lightweight wires and cables, next generation biomedical devices, advanced ballistic protection, and high performance reinforcements.

CNTs can be thought of as a sheet of sp^2 carbon (graphene) rolled into a seamless cylinder [21]. CNTs can be made up of one cylinder, called single-walled carbon nanotubes (SWCNTs), two concentric cylinders, called double-walled carbon nanotubes (DWCNTs), or many concentric cylinders, called multi-walled carbon nanotubes (MWCNTs). CNTs typically have 10 – 40 carbon atoms around the circumference of the nanotube and can be centimeters in length, making them a pseudo-one-dimensional material [21]. CNTs can be described by a pair of integer indices, (n, m), at graphene lattice vectors, a_1 and a_2, which corresponds to the chiral vector,

$$C_h = na_1 + ma_2 \equiv (n, m). \tag{2.1}$$

This vector makes an angle, θ, with the zigzag direction shown as vector C_h in Figure

2.1. The angle ranges from 0 to 30 degrees, where $0\,^\circ<\theta< 30\,^\circ$ corresponds to a chiral CNT, meaning that the tube has two enantiomers: a right-handed and left-handed spiral.
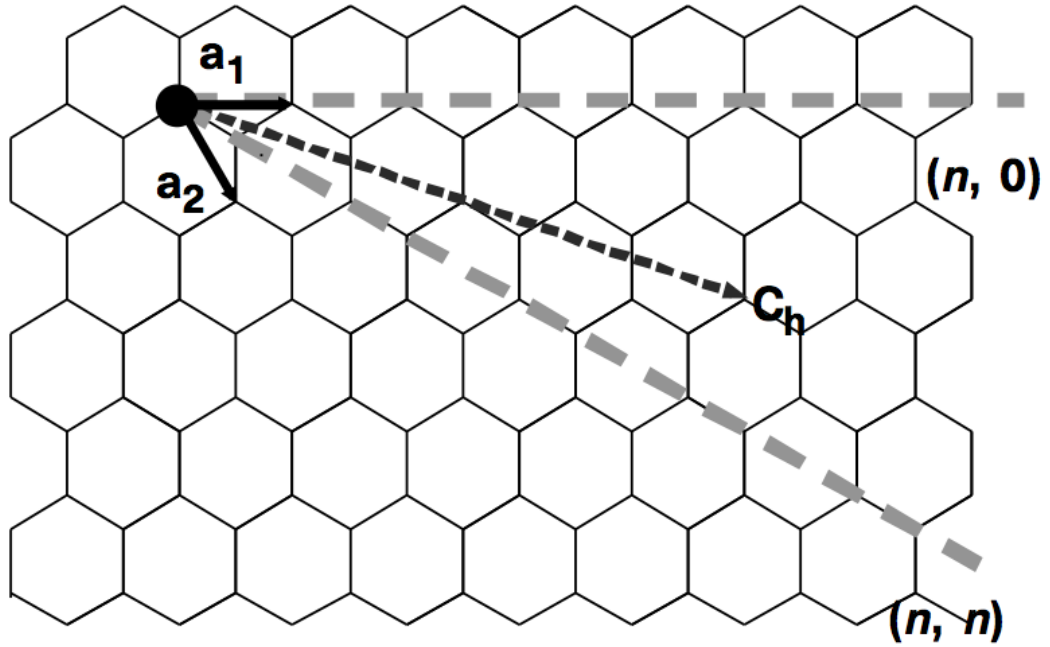
Figure 2.1 : A graphene sheet showing the lattice vectors a_1 and a_2 that compose the folding (chiral) vector C_h. When $n = m$, the CNT has an armchair conformation, and when $m = 0$, the CNT has a zigzag conformation [5].

The indices, (n, m), can also be used to determine if the CNT is semiconducting or metallic. CNTs have an electronic band similar to that of graphene. However, because they are "rolled up", they experience quantum confinement, and they must satisfy a periodic boundary condition. These conditions require the angular wave function to be single-valued. This results in cutting lines of allowed wave vectors as
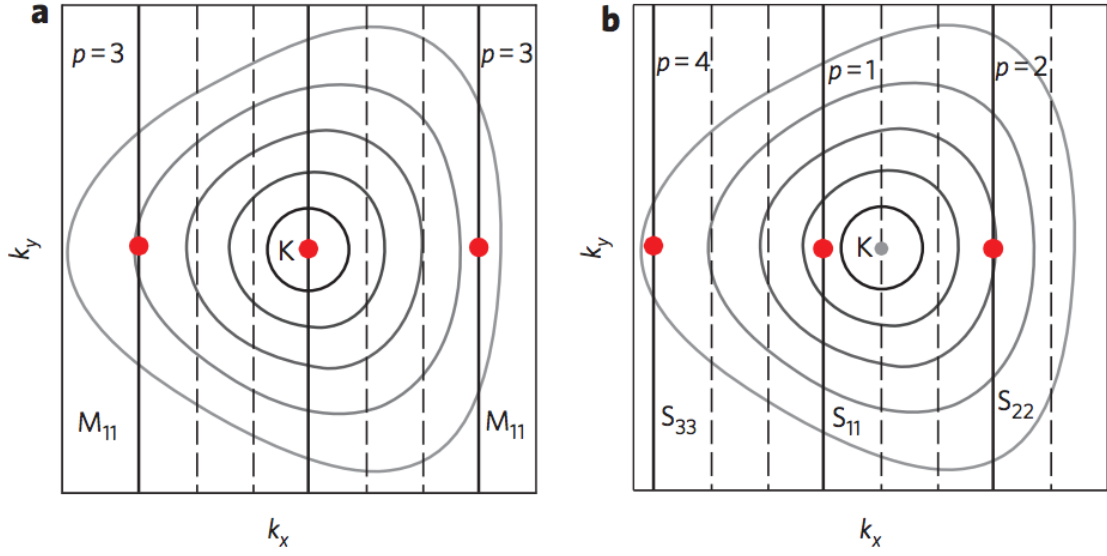
Figure 2.2 : Zone folding diagram for (a) metallic and (b) semiconducting CNT. The contours are lines of constant energy, and the solid lines are the folding lines consistent with the CNT boundary condition [22].

shown in Figure 2.2 [22]. For metallic CNTs, the folding line falls on the K point, meaning that there is no energy gap between the conduction and energy band. For semiconducting CNTs, the folding line falls to the right or left of the K point creating a band gap. Therefore, there are two types of semiconducting CNTs: $MOD1$ and $MOD2$. The type of CNT can be determined as follows:

$$\text{If the remainder of } \frac{n-m}{3} = \begin{cases} 0, & \text{the CNT is metallic.} \\ 1, & \text{the CNT is MOD1 semiconducting.} \\ 2, & \text{the CNT is MOD2 semiconducting.} \end{cases}$$

Although pure metallic nanotubes would be desirable for electronic devices, current methods used for large scale growth of CNTs produces a mixture of metallic and semi-

conducting tubes, and separation of CNTs after synthesis is time intensive, damages the CNTs, and is cost prohibitive. Therefore, typically mixtures of semiconducting and metallic CNTs are used in macroscale CNT articles.

2.2   Phase Behavior of Carbon Nanotubes

The excellent properties of CNTs make them desirable for applications such as separation membranes, sensors, field emission devices, electrochemical actuators, and drug delivery systems [23]. However, CNTs must be processed to create macroscale materials for them to be used in many of these applications. The processing is difficult because CNTs are held tightly together in bundles due to van der Waal attractions [14]. These attractions are estimated to have an energy of 500 ev/μm of tube-tube contact [24]. Additionally, the long aspect ratio (defined as the length of the CNT divided by the diameter) and high flexibility of CNTs leads to entanglement which further hinders the ability of CNTs to be dispersed in water or organic solvents [25]. Significant research has been performed to disperse CNTs so that they can be effectively incorporated into polymer composites and processed into macroscale materials. Successful techniques include ultrasonicating CNTs [25–27], functionalizing CNTs [28–30], and dispersing CNTs in chlorosulfonic acid (CSA) [14, 31, 32]. Once dispersed, CNTs behave according to classical soft matter physics for rigid rod polymers and form isotropic solutions or liquid crystals depending on the CNT concentration. Understanding these fundamental properties of the solution is important for improved solution processing, and thus, better end result materials. The theoretical phase behavior of rigid rods in solution and dispersion of CNTs in CSA will be discussed further in the next sections.

2.2.1   Phase Behavior of Rigid Rods

The first theory for the phase behavior of monodisperse rigid rods in solution was developed by Onsager in 1949 [33]. His theory was based on statistical mechanics and showed that the development of ordered phases stems from the competition between orientational entropy and excluded volume potential. Thus, as the concentration of rigid rods in solution increases, the rods tend to overlap and collide with one another. This causes them to lose translational energy. To regain the transitional degrees of freedom, the rods align, decreasing orientational degrees of freedom but resulting in an overall increase in free energy. In 1955, Flory modeled the phase behavior of rigid rods by using a lattice–based model [34]. Although his model did take into account solvent interactions, it does not accurately describe long range attractions and short range repulsions between rods which are common in colloidal systems. These theoretical
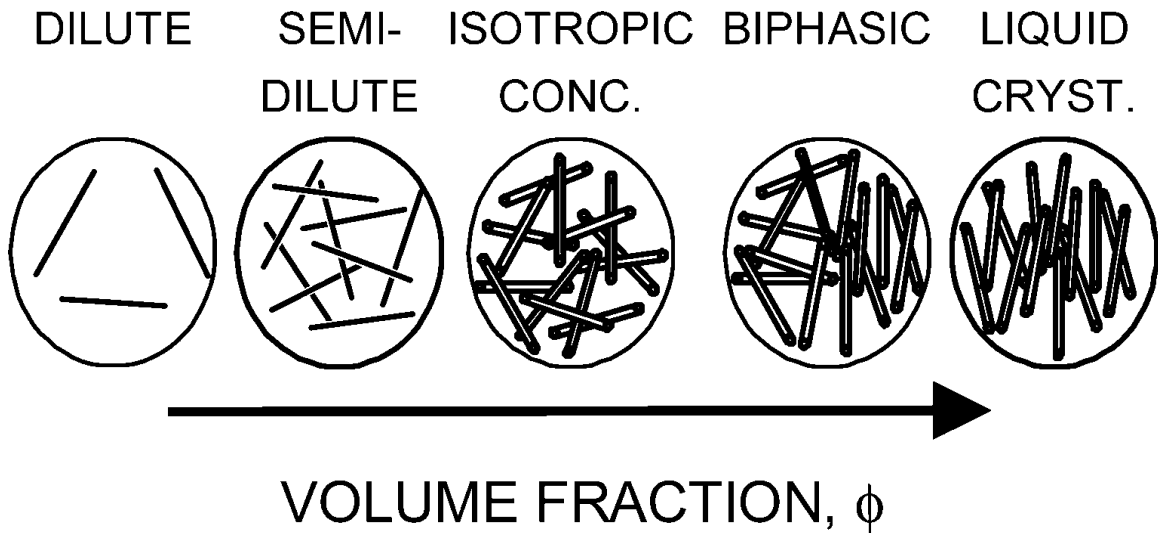
Figure 2.3 : Phase diagram for rigid rods in solution as a function of volume fraction of rods [31].

predictions along with experimental data has shown that rigid rods have three main

regimes: isotropic, biphasic, and liquid crystalline. Within the isotropic regime, the rods can be dilute, semidilute or isotropic concentrated. This is shown in Figure 2.3. The dilute phase transitions to the semidilute phase when rods begin to impair the motion of other rods. More specifically, a sphere with the diameter of one rod must only contain one rod for the solution to be considered dilute. For a solution to be isotropic concentrated, the rods restrict the movement of one another, but not to the point where orientational ordered is favored. When orientational order occurs, the rods enter the biphasic regime meaning that there are both isotropic and anisotropic phases present. Onsager determined that this transition occurs when

$$\phi_i = 3.3\frac{D}{L},\tag{2.2}$$

where ϕ_i is the maximum volume fraction of rods that can all remain in the isotropic phase, D is the diameter of the rod, and L is the length of the rod. On the other hand, Flory determined that this transition occurs when

$$\phi_i = 8\frac{D}{L}(1 - 2\frac{D}{L}).\tag{2.3}$$

Additionally, Onsager predicted that for biphasic solutions of polydisperse rods, the longer rods would tend towards the anisotropic phase whereas the shorter rods would prefer the isotropic phase. In 1950, Oster confirmed this prediction experimentally by using polydisperse solutions of the rod-shaped tobacco mosaic virus (TMV). He observed that, although the isotropic and anisotropic phases had similar concentrations of TMV, the isotropic contained shorter TMV particles than the anisotropic phase. This phenomena was later confirmed computationally by Wensink and Vroege [35]. Wensink and Vroege also demonstrated that as the polydispersity of the rods increases, so does the range of concentrations where the biphasic regime exists. Furthermore, it is interesting to note the spatial distribution of the isotropic and anisotropic

phases. The separation into two distinct phases is the thermodynamic minimum, but this complete separation is not always quick kinetically, especially in solutions of long rigid rods [36, 37]. For solutions of CNTs in superacids, it has been observed experimentally that the solutions transition from bicontinuous to a phase separated solution by forming nematic droplets called tactoids [36, 37]. The areas of alignment can be seen using a polarized optical microscope (POM), and a polarizing optical micrograph of tactiods formed by CNTs in CSA which can be seen in Figure 2.4. Over time, the liquid crystal droplets merge to minimize surface energy creating larger and larger droplets, eventually leading to a continuous phase. This process occurs faster for rods with lower aspect than for rods with higher aspect ratio.
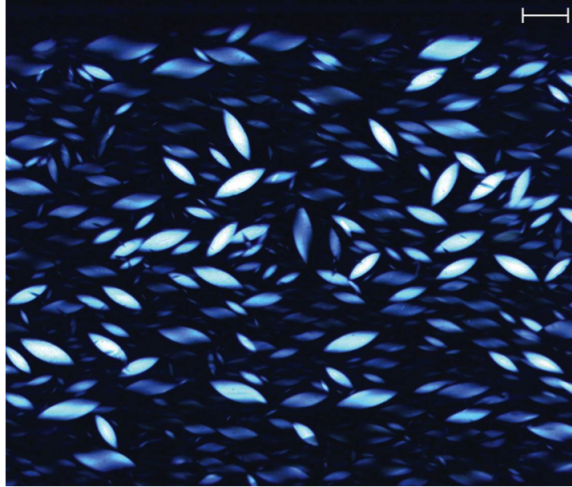
Figure 2.4 : Polarized optical micrograph of tactoids formed in a glass capillary from solutions of 1000 ppm CCNI CNTs in CSA. The scale bar is 100 μm [37].

Finally, the nematic liquid crystal phase occurs when the rods have an overall alignment in a single direction, but do not necessarily have positional order. Onsager predicted this to occur at

$$\phi_{nem} = 4.5\frac{D}{L}, \tag{2.4}$$

where ϕ_{nem} is the volume fraction of rods necessary to form the nematic phase. Flory's theory predicted that the transition occurred at

$$\phi_{nem} = 12\frac{D}{L}. \tag{2.5}$$

Although these theories clearly differ in the exact isotropic and nematic transition because they use different assumptions, they do agree that the transitions vary inversely propositional to the aspect ratio of the rods.

2.2.2 Carbon Nanotube Dispersions in Chlorosulfonic Acid

As mentioned previously, CNTs can be dispersed through surfactants and ultrasonication, chemical functionalization, and dissolution in CSA [14, 25–32]. However, ultrasonication can induce defects and shorten tubes which hinders the performance of any resulting materials [38, 39]. Functionalization degrades the electronic and thermal properties because it converts sp^2 carbon bonds into sp^3 bonds which delocalizes π orbitals [13, 25]. CSA (as well as other strong acids) are the only known true solvents [13, 14]. As shown by Ramesh $et\ al.$, CSA is able to overcome the strong van der Waal attractions by protonating the CNT. This occurs because CNTs act as a weak base which delocalizes a positive charge across the entire CNT, forming a polycarbocation. The charge of the polycarbocations creates a repulsive force which inhibits the tubes from bundling. Its stability depends on the conjugate base, and can be viewed as the following reaction:

$$\mathrm{C}_x + y\mathrm{SO_3ClH} \rightarrow \mathrm{C}_x^{\delta+}\mathrm{H}_y^{(1-k\delta)+} + y\mathrm{A}^-$$
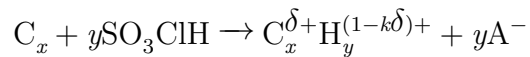
where $k = x/y$ and δ is the positive fractional charge on each carbon atom in the CNT.
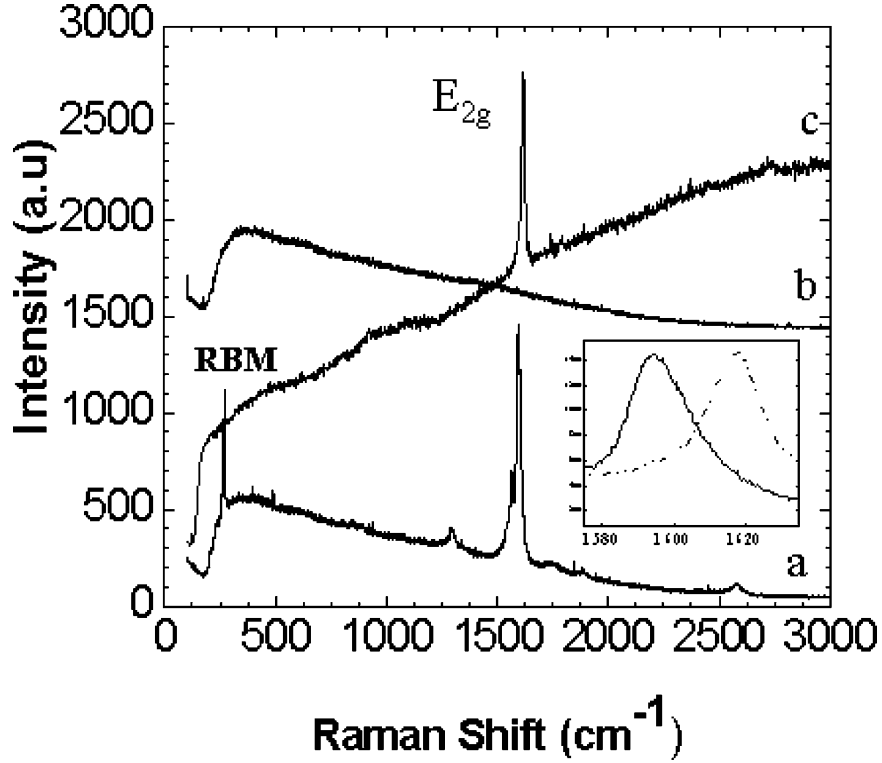
Figure 2.5 : Raman spectrum of HiPCo CNTs a) before dispersion in CSA ($\lambda_{exc} =$ 780 nm), b) in a 2.5 wt% paste in CSA ($\lambda_{exc} =$ 780 nm), and c) in a 2.5 wt% paste in CSA ($\lambda_{exc} =$ 514 nm). The inset shows a 23 cm^{-1} shift due to protonation [14].

Raman spectroscopy can be used to determine the fractional charge. Sumanasekera et $al.$ found that SWCNTs have an upshift in the Raman spectra of 320 cm^{-1} per hole, per C-atom with bisulfate (HSO_4^-) as a dopant [41]. This value is thought to be universal for SWCNT acting as a proton acceptor. Ramesh et $al.$ extended this finding to SWCNTs in CSA. Figure 2.5a shows a Raman spectrum for SWNT taken with a 780 nm laser, and the E_{2g} stretching mode was found to be at 1596 cm^{-1}. Figure 2.5b shows a Raman spectra for a 2.5 wt% SWCNT paste in CSA. This spectrum shows only background scattering because the 780 nm laser probes the $\nu_1 \rightarrow c_1$ electronic
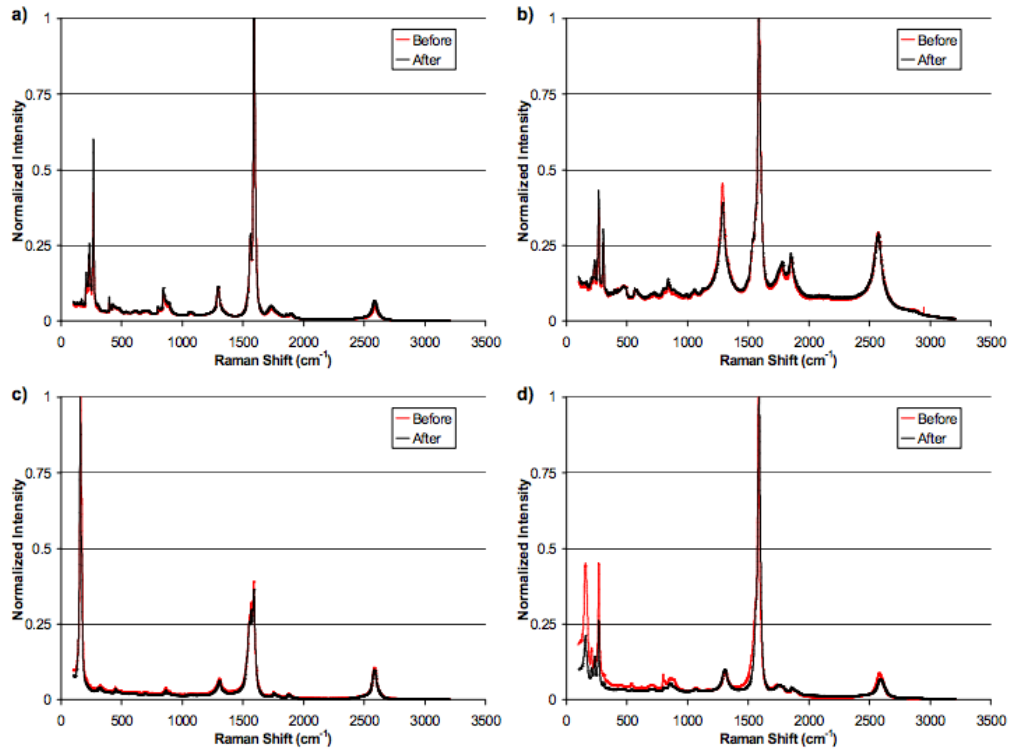
Figure 2.6 : Raman spectra for a) HiPCo (D-peak at 1290 $cm^{-1}$and G-peak at 1590 cm^{-1}), b) CoMoCat (D-peak at 1285 cm^{-1} and G-peak at 1588 cm^{-1}), arc discharge (D-peak at 1290 cm^{-1} and G-peak at 1588 cm^{-1}), and Sunnano (D-peak at 1295 cm^{-1} and G-peak at 1588 cm^{-1}) before and after dissolution in CSA. Reprinted with permission from [40]. Copyright 2010 American Chemical Society.

transition which is hindered by the protonation process. Figure 2.5c also shows a Raman spectra for a 2.5 wt% SWCNT paste in CSA. However, this sample was probed with a 514 nm laser. The 514 nm laser probes the $\nu_2 \rightarrow c_2$ electronic transition which is unaffected by the protonation. The E_{2g} appears at 1619 cm^{-1} which is a shift of 23 cm^{-1} from the dry SWCNT. Therefore, using Sumanasekera's reported value, it was estimated that a positive charge is shared by 14 carbon atoms. Additionally,
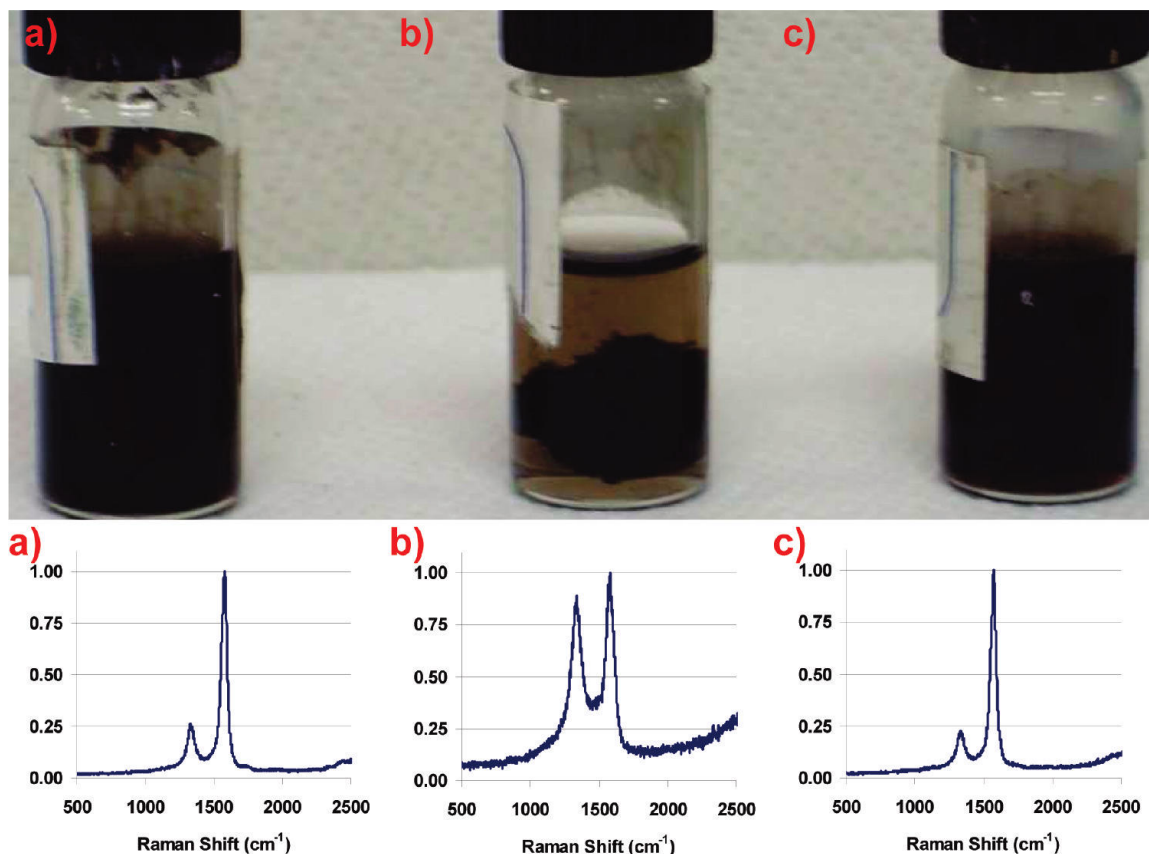
Figure 2.7 : The top panel visually demonstrates the solubility of a) SWCNTs grown for 15 min at 750 °C, b) SWCNTs grown for 30 min at 550 °C, c) and SWCNTs grown for 30 min at 750 °C after centrifugation for 24 hours. The bottom panel shows Raman spectra taken on each sample to demonstrate the quality of the tubes. Each sample shows a G-peak at 1590 cm^{-1} and a D-peak at 1350 cm^{-1} which is a measure of sp^3 carbon bonds. It can be seen that the highly defective sample, b, does not stay in solution. Reprinted with permission from [40]. Copyright 2010 American Chemical Society.

CSA directly protonates CNTs without causing oxidation. Furthermore, this process is reversible as confirmed through Raman spectroscopy [40]. As shown in Figure 2.6,

the Raman spectra do not show any shifts in the G-peak meaning that there is no longer CNT protonation. The spectra also do not show any increase in the D-peak, so the CSA did not cause any additional defects such as oxidization or sulfonation of the CNTs. Furthermore, it has been shown that the protonation process is not as effective with CNTs with high defects [40]. To demonstrate this concept, Para-Vasquez *et al.* centrifuged solutions of CSA and pristine CNTs grown at $750\,^{\circ}\text{C}$ and CSA and defective CNTs grown at $550\,^{\circ}\text{C}$. The results are shown in Figures 2.7 a-c. Additionally, Raman spectra are presented to demonstrate the relative defectiveness of the samples.

CSA, the strongest of the superacids that have been studied, has been shown to dissolve CNT bundles spontaneously (without stirring) at the fastest rate and at the highest concentrations [13, 42]. It has been shown by Davis *et al.* that the acid strength, and thus fractional charge per carbon, δ, affects the isotropic and nematic point [13]. This diagram is shown in Figure 2.8. The diagram demonstrates the high solubility of CNTs in super acids, and shows that at sufficient CNT concentration and acid strength that liquid crystals form. The alignment of the solutions is shown visually in the polarized optical micrographs, Figure 2.8 a-d. The model shown was developed by Green *et al.* as an extension of Onsager's theory for rigid rods [32]. The model takes into account attractive interactions which is essential for capturing behaviors of CNT-superacid solutions. Understanding the phase diagram and phase transitions is important for proper processing of CNTs which will be discussed in the following chapters.
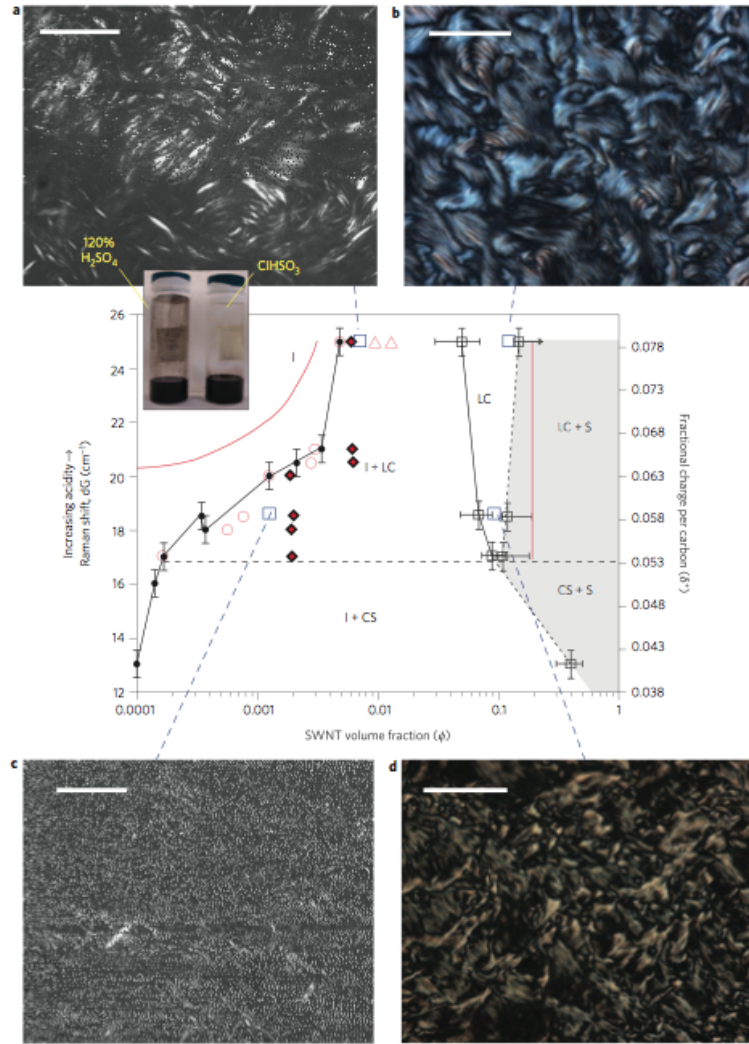
Figure 2.8 : Phases shown are Isotropic (I), liquid crystalline (LC), crystal solvate (CS), and solid (S). Black symbols represent experimental results and red symbols represent model predictions from Green *et al.* [32]. Diamonds represent the concentration of an initial system before phase separation. Circles represent the isotropic phase,ϕ_i after phase separation. Red triangles represent ϕ_i and ϕ_{hem} for Onsager's theory of monodisperse hard rods. Red lines are the model predictions for isotropic and nematic stability limits. Black dotted lines demonstrate experimental phase boundaries. It is also theorized that a liquid crystal and crystal solvate biphasic regime may exist within the shaded region. Blue squares represent the conditions for the polarizing optical micrographs a-d [13].

Chapter 3

Purification of Carbon Nanotubes for Solution Processing in Chlorosulfonic Acid*

3.1 Introduction

Carbon nanotubes (CNTs) have been widely studied due to the unique combination of thermal, electrical and mechanical properties [18]. Despite significant progress in translating these excellent properties at the molecular scale to macroscale articles such as fibers, the cost of the material has hindered widespread adoption of CNT fiber (CNTF) [12, 43]. To reduce the cost of CNTF, the fiber itself must be produced in an efficient and scalable manner. Furthermore, the efficiency of CNT growth must be improved, and the scale of production must be increased. Solution spinning of CNTs utilizes a technique that has already been successfully scaled up for other polymers such as aramids (Twaron® from Teijin and Kevlar® from DuPont) and polyacrylonitrile (carbon fiber precursor) [44, 45]. In the solution spinning process, CNTs are dissolved into chlorosulfonic acid (CSA) [12, 46, 47]. At CNT concentrations used for fiber spinning, CNTs form liquid crystals which aid in the alignment of CNTs during processing [13, 14, 31]. To further improve the alignment, the solution is extruded through a spinneret and drawn under tension in a coagulation bath [11–13]. The fibers are then collected continuously onto a rotating drum. The production of the fiber can be easily scaled up by introducing more holes in the spinneret to produce

---

*This chapter is an updated version of a draft article in preparation for submission

more filaments of fiber [11]. The other benefit to this fiber production method is that CNT synthesis is decoupled from the spinning process. This means that CNT production can be optimized for catalyst and cost efficiency instead of optimizing for aerogel formation, which is required for solid state spinning methods that produce fiber directly from a growth furnace [43]. However, many as produced CNTs do not dissolve in CSA and require purification [12, 13]. To continue to improve CNT fibers and drive down costs, it is necessary to utilize CNTs from a variety of sources. Therefore, it is crucial to understand the underlying mechanism that prohibits CNTs from spontaneously dissolving in superacid [40].

Previous work has studied various purification methods for improved dissolution of CNTs that included combinations of air oxidation, argon annealing and hydrochloric acid (HCl) washing [46]. The authors of this work attributed the improved solubility of the CNTs to the addition of oxygen sites into the sidewall of the CNT. Furthermore, the authors report that iron catalyst expands and breaks the carbon shells that are coating the particles during oxidation so that the particles are accessible during the HCl wash. However, when the material is washed with HCl after annealing with argon, the authors do not see the same phenomena as the sample still contains over 14% iron by weight. Here, we report that there is no evidence to suggest that the purification process of CNTs induces additional oxygen groups. Instead, the CNTs are coated with amorphous carbon which is removed during the oxidation step [48]. We propose that poor dissolution arises from amorphous carbon coating the sidewalls of the CNTs. The amorphous carbon is not protonated by superacid and inhibits the acid from accessing the sp^2 bonded carbon along the backbone of the CNT. Therefore, the coated CNTs are not individualized in solution. Furthermore, we study the effects of the oxidation time and temperature on the remaining catalyst

content, CNT crystallinity, and CNT aspect ratio after purification. Understanding the relationship between purification, solubility, and aspect ratio is necessary for optimizing fiber properties and reducing fiber costs.

3.2 Experimental Methods

3.2.1 Carbon Nanotube Purification

Sample	Oxidation Temperature (°C)	Oxidation Time (hours)
1	400	12
2	420	12
3	440	12
4	460	12
5	420	3
6	420	6
7	420	24

Table 3.1 : Temperature and length of time for each purification method tested.

CNTs were purchased from OCSiAl (Tuball Single Wall Carbon Nanotubes, Batch 01RW01.N1.257). 100 mg of material was weighed (Denver Instruments APX–100) and placed into an alumina boat. The boat was pushed into the center of a 2.5–inch tube furnace (Mellen NACCI) under a flow rate of 20 sccm N_2 (Matheson, industrial grade nitrogen) and 80 sccm O_2 (Matheson, industrial grade oxygen). The furnace was ramped to the desired purification temperature at 5 °C/min, held at temperature

for the indicated time, and cooled to 100 °C at 1.5 °C/min before the sample was removed. The purification temperature and time for each study is shown in Table 3.1. The CNTs were weighed after oxidation and the weight loss was recorded. Next, 50 mg of the oxidized material was weighed and put into a 250 mL Erlenmeyer flask with 150 mL of hydrochloric acid (HCl 37%, Sigma–Aldrich). The CNTs were stirred at 400 rpm overnight and vacuum filtered to remove the HCl. The material was rinsed thoroughly with water and returned to the Erlenmeyer flask with 150 mL of water. The water was heated to 100 °C and the CNTs were stirred again at 400 rpm overnight. The CNTs were vacuum filtered and lyophilized (Millrock Bench Top Manifold Freezer Dryer BT48) to remove residual water. The CNTs were weighed and the weight loss was recorded.

3.2.2 Carbon Nanotube Characterization

The G/D ratio of the CNTs was measured with Raman spectroscopy (Renishaw InVia Confocal Raman microscope). Spectra were obtained with 532 nm, 633 nm, and 785 nm wavelength lasers and the average G/D ratio was taken as a ratio of the maximum of the G peak to the maximum of the D peak averaged over 10 measurements. Thermogravimetric Analysis (TA Instruments, SDT Q600) was performed from 100 °C to 1000 °C at a ramp rate of 10 °C/min under 100 mL/min of air to determine the quantity of iron remaining after purification. X-ray photoelectron spectroscopy (PHI Quantera) was performed using an aluminum kα X–ray source from 282–294 eV for carbon, 527–536 eV for oxygen, and 707–726 eV for iron at a step size of 0.1 eV and a pass energy of 26. Qualitative sample purity was assessed by HR-TEM imaging (JEOL 2100–F) at 200 kV. CNTs were dispersed in acetone with two minutes of tip sonication. Drops of the dispersion were placed on lacey

carbon grids and blotted dry. SEM images were taken with an FEI Helios NanoLab 660 DualBeam system with an accelerating voltage of 5 kV and current of 100 pA. Solutions of CNTs in CSA were imaged with a Zeiss Axioplan polarized optical microscope in 100 μm glass capillaries (VitroCom) that were sealed at the ends with a butane torch. The viscosity averaged aspect ratios of the CNTs were measured with dilute solutions of CNTs in CSA using extensional rheology (Cambridge Trimaster) as described previously [49]. Measurements were performed in triplicate.

3.3   Results and Discussions
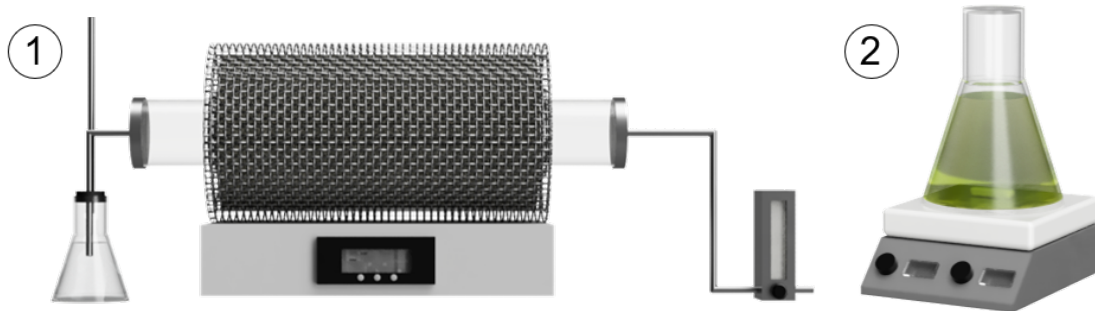
Figure 3.1 : Schematic of the purification process. First, CNTs are oxidized in a tube furnace to remove amorphous carbon. Second, CNTs are washed with HCl to remove iron catalyst.

CNTs were purified using a two–step process to remove both amorphous carbon and iron catalyst impurities (Figure 3.1). First, CNTs were oxidized to remove amorphous carbon and low crystallinity (as described by low Raman G/D ratio) CNTs at various temperatures and lengths of time in a tube furnace under a flow of 100 sccm of air. Second, CNTs were washed in HCl to remove the iron catalyst in accordance

with the following reaction:

$$Fe + 2HCl \rightarrow FeCl_2 + H_2.$$
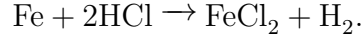
The CNTs were then filtered to remove the HCl, washed in water until a neutral pH was obtained, and lyophilized to remove residual water.
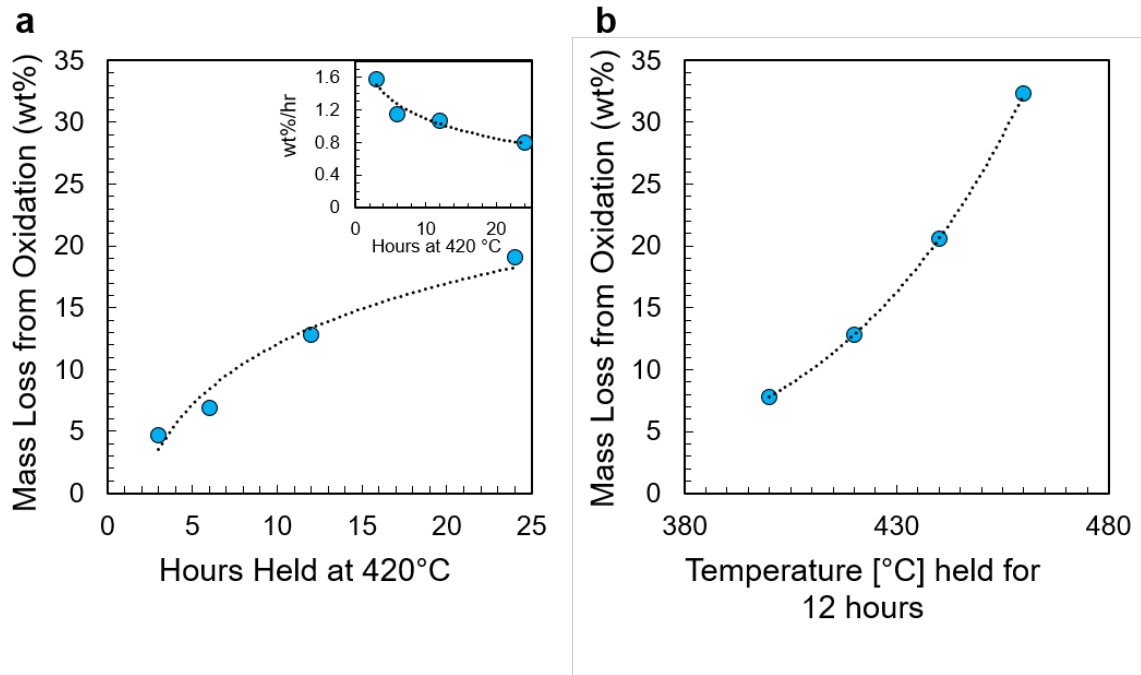
Figure 3.2 : (a) The percent mass loss from oxidation at 420 °C with varying purification time. The inset shows the rate of mass loss for each purification time. (b) The percent mass loss from oxidation at 12 hours with varying purification temperature.

Figure 3.2a shows the sample mass loss while increasing the oxidation time but holding the temperature constant (420 °C). With increasing time, the total mass loss begins to plateau. This is further demonstrated by the inset in Figure 3.2a; the average rate of mass loss per hour drops significantly for the 24 hour purification time. The mass loss of the sample with increasing temperature and constant purification

time (12 hours) is described nicely by an exponential trend (Figure 3.2b). Furthermore, oxidizing at 440 °C or 460 °C for 12 hours burned more CNT sample than when oxidizing the sample for 24 hours at 420 °C. Hotter temperatures enable the oxidation of more stable carbon allotropes in the sample such as lower crystallinity CNTs or faster oxidation of the ends of higher–crystallinity CNTs. Thermogravimetric Analysis (TGA) was performed on each of the oxidized samples after washing with HCl. As shown in Figures 3.3, the unpurified CNT material contained a significant quantity of iron catalyst with a residual sample mass of ~19 wt% after ramping to 1000 °C. Assuming complete oxidation of the iron into Fe_2O_3, the raw material is estimated to contain ~14 wt% iron. In contrast, all samples oxidized for 12 hours or longer, regardless of the oxidation temperature, did not contain substantial quantities of iron catalyst. However, the samples that were oxidized for 3 hours and 6 hours at 420 °C still had residual catalyst. This indicates that carbon that encapsulates some of the iron catalyst particles were not fully removed during the oxidation process. Therefore, the HCl could not access these particles to dissolve and remove them from the sample.

Figure 3.4 display the Raman G/D ratio of the purified samples normalized to the G/D ratio of the raw material. The G band appears at ~1590 cm^{-1} and results from stretching of sp^2 hybridized carbon lattices. The D band appears at ~1350 $^{-1}$ and results from defects in the structure such as sp^3 hybridized carbon or 5 or 7 membered rings. Therefore, a higher G/D ratio indicates a more pristine or crystalline carbon lattice and is used as a qualitative measure of the crystallinity of CNTs. All samples saw an improvement in the G/D ratio after purification indicating that we are successfully removing defective CNTs from the samples and not inducing additional defects such as oxygen into the CNT lattice. Oxidation at 440 °C for 12 hours showed
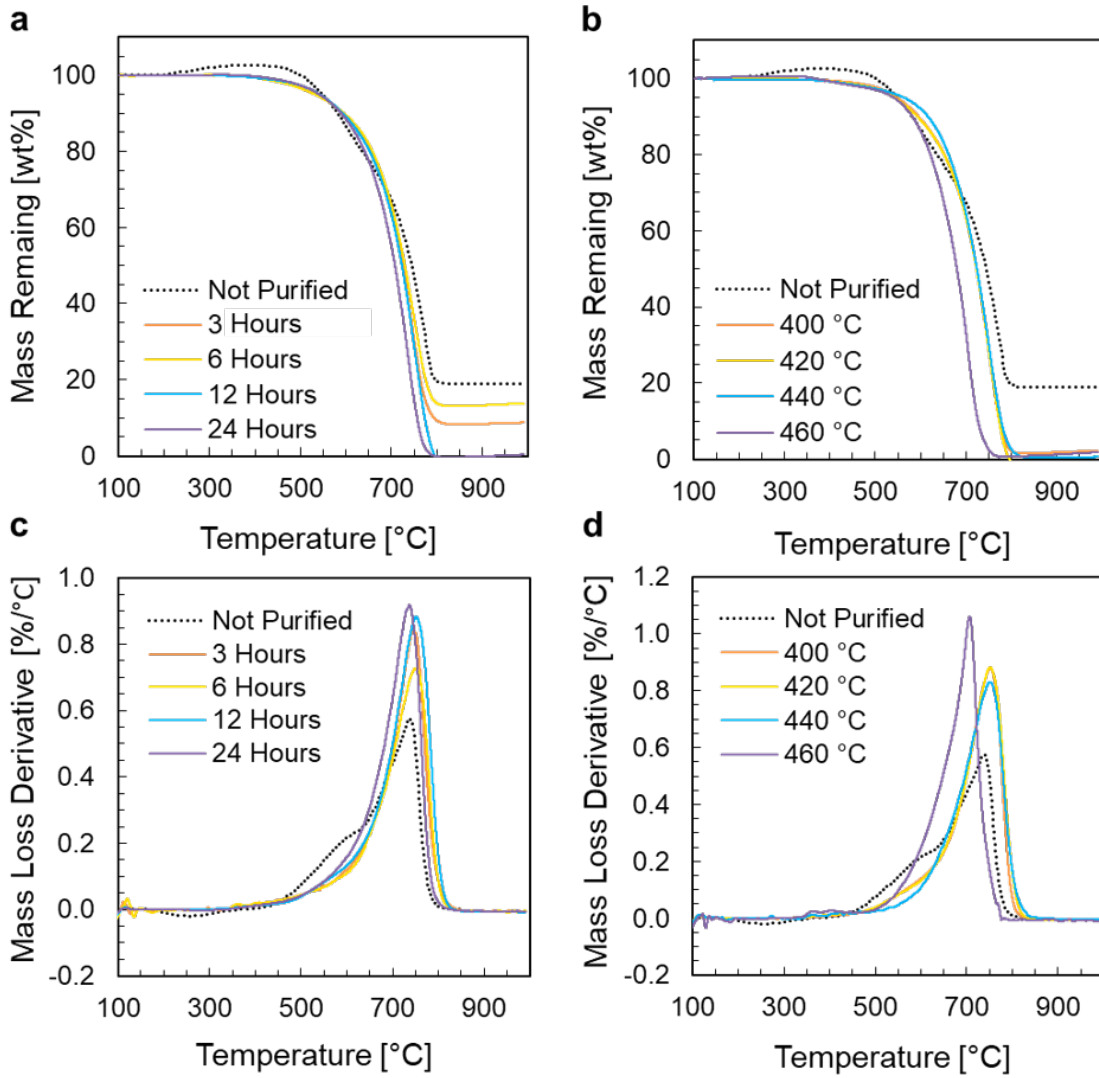
Figure 3.3 : Thermogravimetric analysis on samples oxidized (a) at 420 °C for varying times and (b) for 12 hours at varying temperatures. Mass loss derivatives of samples oxidized (c) at 420 °C for varying times and (d) for 12 hours at varying temperatures.

the best improvement in G/D from the raw material; the G/D ratio improved from an average of 48, 26, and 10 for the raw material to 88, 58, and 21 for the 532, 633, and 785 nm lasers, respectively.
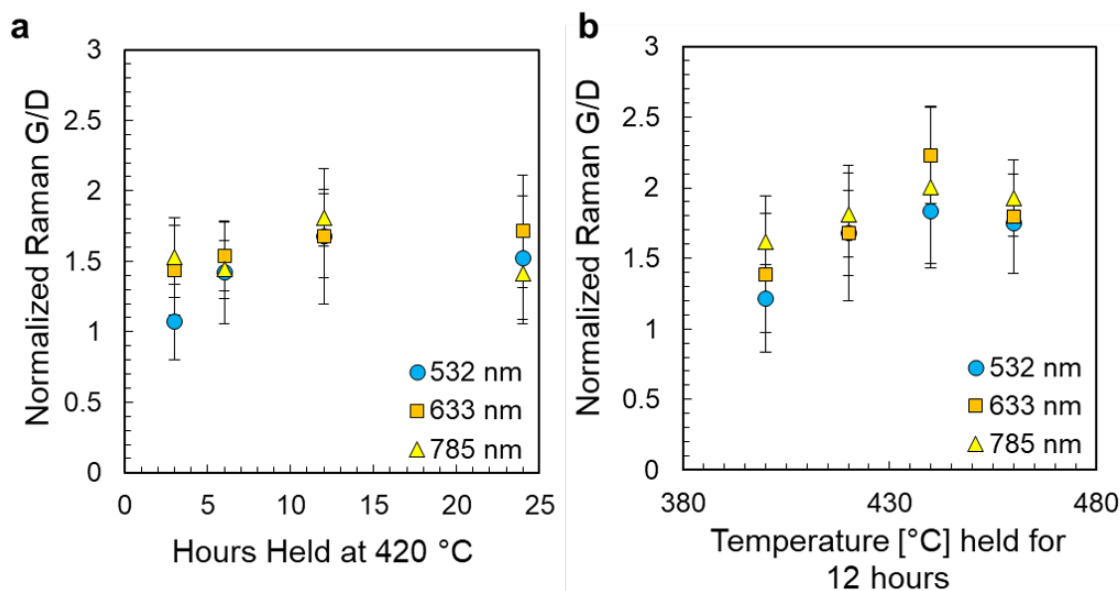
Figure 3.4 : G/D ratios from Raman spectroscopy normalized to the as received material for samples oxidized (a) at 420 °C for varying times and (b) for 12 hours at varying temperatures.

Sample	Carbon	Oxygen	Iron
As Received	96.5±1.6 at%	2.6±1.8 at%	1.0±0.1 at%
Oxidized 420 °C 12 hrs	91.7±1.2 at%	6.2±0.6 at%	2.4±0.4 at%
Oxidized 420 °C 12 hrs + HCl Wash	97.0±0.2 at%	2.8±0.1 at%	0.3±0.1 at%

Table 3.2 : Atomic composition of Tuball from XPS analysis. After oxidation, there is a significantly higher percentage of oxygen due to oxidation of the iron catalyst.
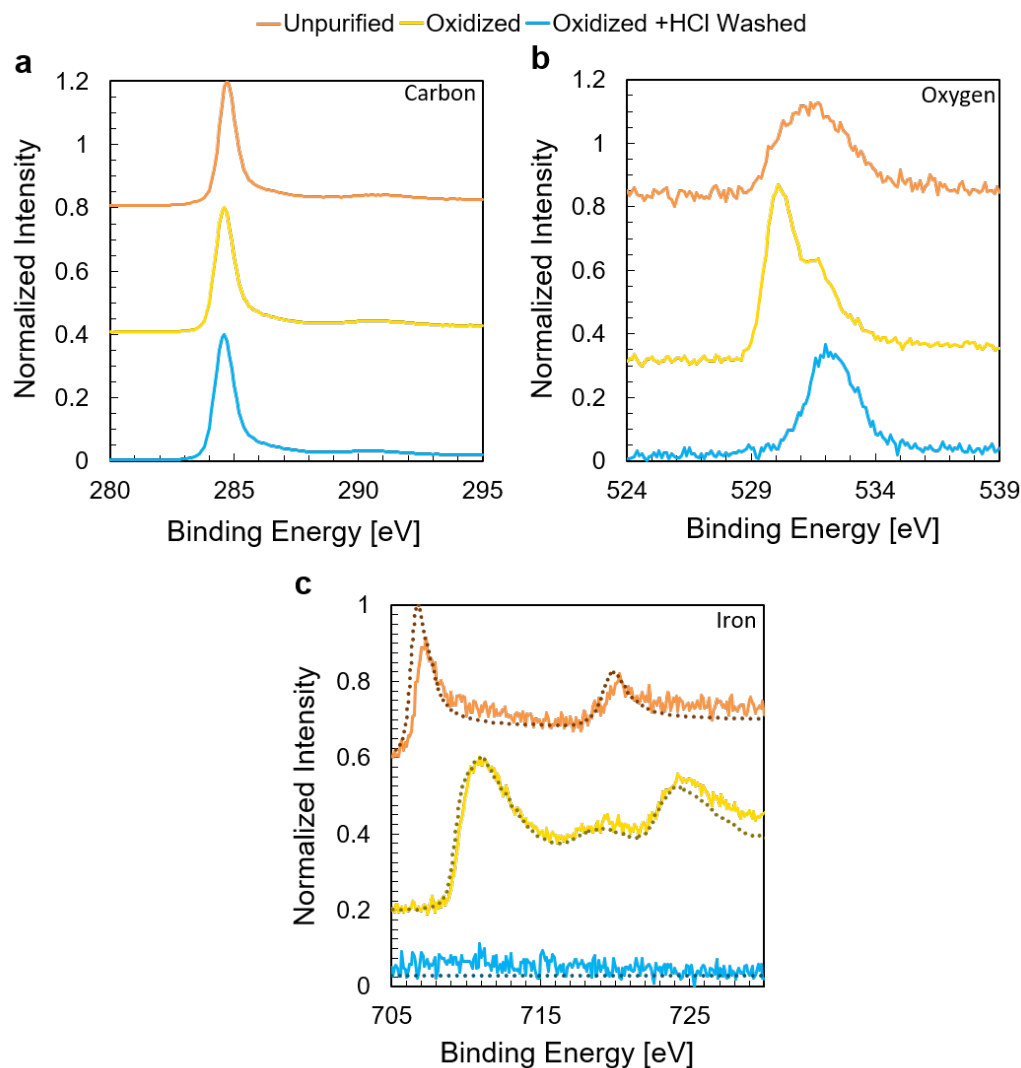
Figure 3.5 : X–ray photoelectron spectra for as received CNTs (Unpurified, orange), CNTs oxidized at 420 °C for 12 hours (Oxidized, yellow), and CNTs oxidized at 420 °C for 12 hours and washed with HCl (HCl Washed, blue) for a) carbon, b) oxygen, and c) iron. The brown dotted line is the expected spectra for metallic iron and the dark yellow dotted line is the expected spectra for Fe_2O_3 [50].

X-ray photoelectron spectroscopy (XPS) was used to examine the changes in chemical state of the elements present in the samples during both steps of the purification process. A survey scan over the entire energy range indicated that the samples contained carbon, oxygen and iron. A comparison of the raw material, material oxidized at 420 °C for 12 hours, and material oxidized at 420 °C for 12 hours with an HCl wash is shown in Figure 3.5. The spectra for carbon (Figure 3.5a) are very similar for each sample. However, the large carbon peak was shifted slightly downwards (284.6 eV) indicating an increase in the relative quantity of sp^2 bonding from sp^3 bonding in the sample. After oxidation, we saw an increase in the oxygen content in our sample and a well-defined oxygen peak appeared at a binding energy of 530.1 eV (Figure 3.5b). The location of this peak is consistent with the formation of α-Fe_2O_3 from the oxidation of the iron catalyst. This is confirmed by the spectra obtained for iron (Figure 3.5c). The spectrum of the raw material displayed peaks at 707.3 eV and 720.3 eV corresponding to Fe $2p_{3/2}$ and Fe $2p_{1/2}$ spin states. The experimental data (solid orange line) aligns very well with the expected spectrum for metallic iron (dotted brown line) [50]. However, for the oxidized sample, the peaks are shifted to 710.9 eV and 724.2 eV and the spectrum has an additional peak at 719 eV corresponding to a Fe(III) 2p3/2 satellite feature. The experimentally obtained spectrum is in good agreement with the spectrum expected for α-Fe_2O_3 (dotted dark yellow line) [50]. Additionally, the sample washed with HCl does not display a significant peak in the energy range expected for iron which further confirms that the iron was successfully removed from the sample. Finally, a summary of the atomic composition of the elements studied is shown in Table 3.2. The oxygen content is the highest for the sample that was only oxidized. This increase in oxygen content is due to the oxidation of the iron within the sample. Once the iron is removed from the CNTs,

the sample has a similar oxygen content to the as received material. Moreover, the oxidized sample also has the highest iron content. This can be attributed to the small depth of analysis ($\sim$5 nm) for XPS measurements. Before oxidation, the iron catalyst is covered with a carbon shell, limiting the quantity of iron probed. Once the carbon is removed, a larger quantity of iron can be probed by the X–rays. This result further supports the idea that amorphous carbon is being removed from the sample.
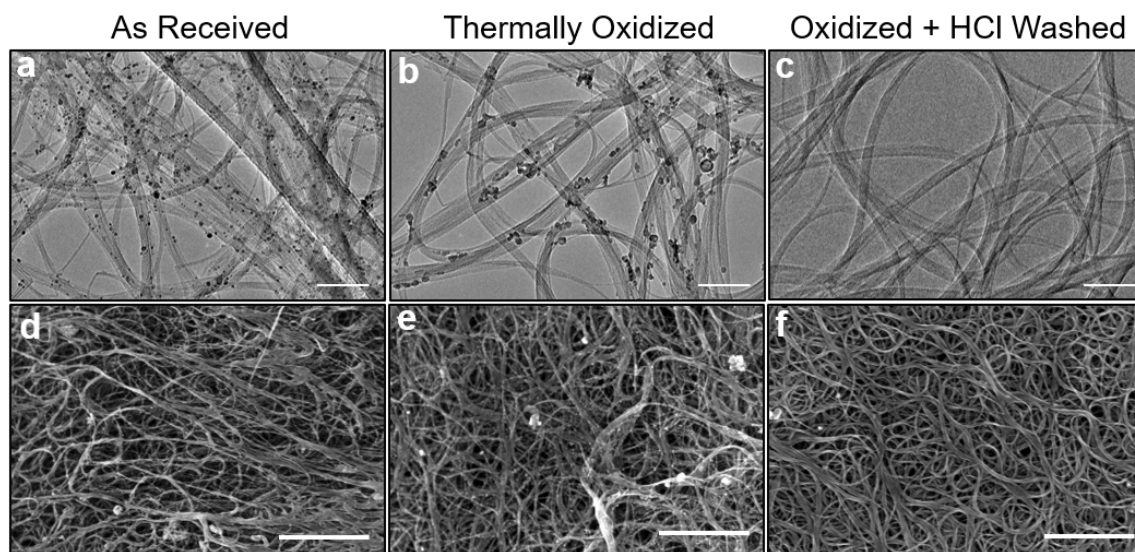
Figure 3.6 : Transmission electron microscopy images of (a) as received CNTs, (b) CNTs oxidized at 420 °C for 12 hours, and (c) CNTs oxidized at 420 °C for 12 hours and washed with HCl. Scale bars are 100 nm. Scanning electron microscopy images of (d) as received CNTs, (e) CNTs oxidized at 420 °C for 12 hours, and (f) CNTs oxidized at 420 °C for 12 hours and washed with HCl. Scale bars are 1 μm. TEM images courtesy of O. S. Dewey.

CNTs were examined via transmission electron microscopy (TEM, Figure 3.6a–c) and scanning electron microcopy (SEM, Figure 3.6d–f) before purification, after oxidation at 420 °C for 12 hours, and after washing with HCl. The raw CNTs

(Figure 3.6a) and the oxidized CNTs (Figure 3.6b) contained significant quantities of catalyst particles dispersed throughout the sample. These particles are not seen in the sample washed with HCl (Figure 3.6c). Under SEM, the effectiveness of the purification is easily visualized. Figure 3.6d shows bundles of CNTs that are coated with amorphous material and the presence of spherical particles. In Figure 3.6e, the amorphous material has been removed, and the catalyst particles are now seen very clearly covering the entire sample. Significantly more catalyst can be seen on the oxidized sample because many of the particles are encapsulated within the amorphous material and therefore, obscured in the as received material. Finally, Figure 3.6f shows clean bundles of CNTs with minimal impurities.

The samples were tested for their solubility in chlorosulfonic acid (CSA) by speed-mixing samples at a concentration of 500 ppmw and visualizing the samples under a microscope with transmitted light and polarized light. As seen in Figure 3.7a, the raw material does not dissolve in CSA. The CNTs remain tightly bundled together. Furthermore, under polarized light, the bundles themselves birefringe due to the alignment within the bundles, but there do not appear to be liquid crystals, which are expected for true solutions of CNTs of this aspect ratio and concentration [31]. However, by removing defective CNTs and amorphous carbon covering the CNTs, the acid is accessible to the CNTs allowing for protonation and thus, dissolution (Figure 3.7b). Although there are undissolved particles in the sample, the CNTs themselves appear fully debundled. The formation of liquid crystals is evident under cross polarizers (Figure 3.7e and h). Additionally, the presence of oxidized iron catalyst does not inhibit the solubility of CNTs, but as discussed in Chapter 5, removal of the catalyst particles is desirable because they can react with the CSA and decrease the acid strength. If the acid strength decreases significantly, the CNTs do not fully individu-
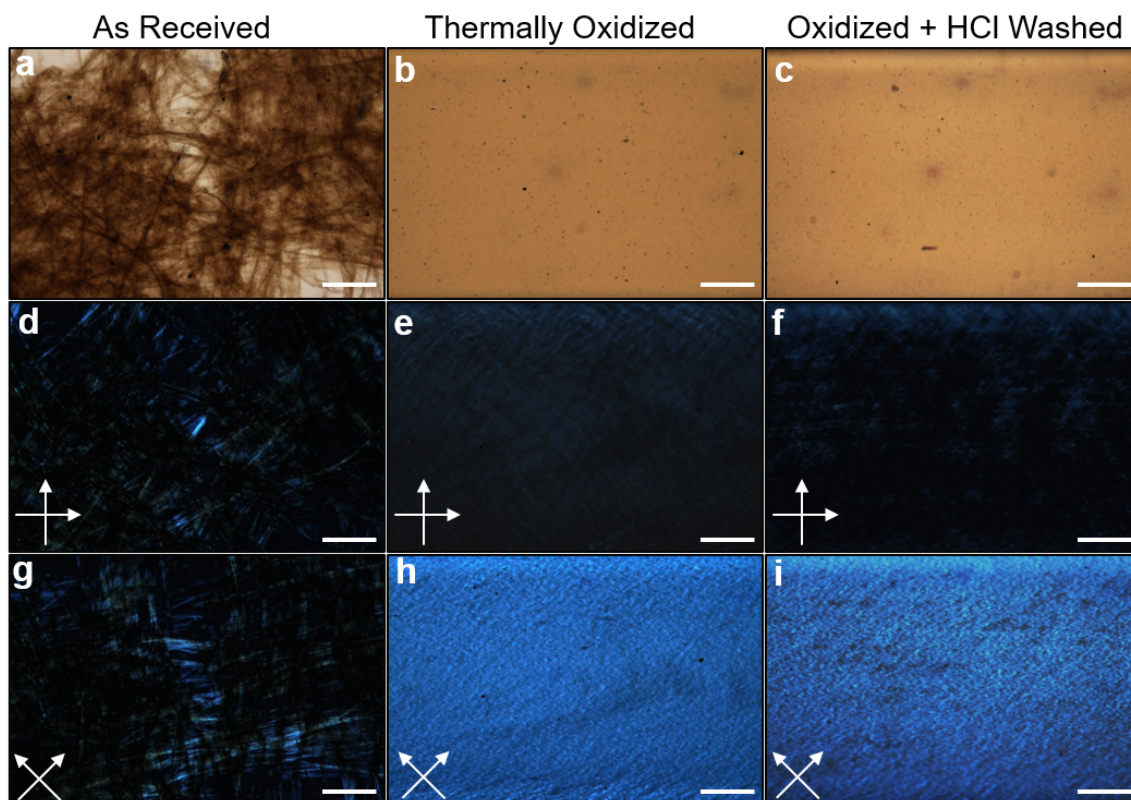
Figure 3.7 : Transmitted light microscopy images of (a) as received CNTs, (b) CNTs oxidized at 420 °C for 12 hours, and (c) CNTs oxidized at 420 °C for 12 hours and washed with HCl in CSA at a concentration of 500 ppmw. Scale bars are 200 μm. Polarized light microscopy images of (d) and (g) as received CNTs and (e) and (h) CNTs oxidized at 420 °C for 12 hours, and (f) and (i) CNTs oxidized at 420 °C for 12 hours and washed with HCl in CSA at a concentration of 500 ppmw. Scale bars are 200 μm.

alize which hinders solution spinning. As with the oxidized sample, the sample after the HCl wash also has some undissolved particles (Figure 3.7c) but forms well-defined liquid crystals in solution (Figure 3.7f and i).

These results, along with the conclusions drawn from Raman spectroscopy, and
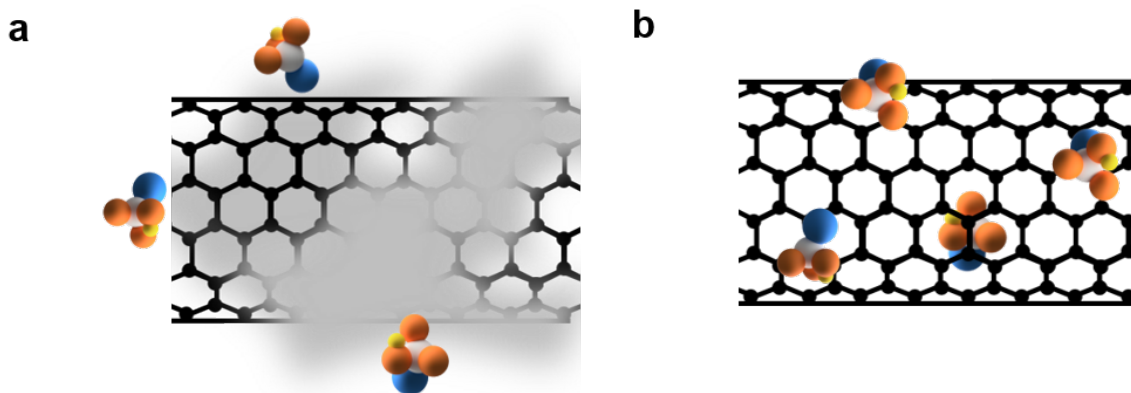
Figure 3.8 : (a) Schematic of amorphous carbon shielding a CNT from protonation by superacid. (b) Schematic of protonation of an oxidized CNT.

XPS, indicate that purification is essential for dissolution of Tuball into CSA because the amorphous carbon and hinders the dissolution process. The amorphous carbon covers the bundles of CNTs and does not allow the CSA to access the sidewall of the CNT (Figure 3.8). This is essential for obtaining true solutions because sufficient protonation is required for CNTs to overcome the van der Waals forces to individualize in the solvent [14]. Therefore, a purification method that sufficiently removes the amorphous carbon is necessary for effective solution processing as poorly dissolved CNTs cannot be restructured into a highly aligned fiber and undissolved particulates can clog the spinneret.

Finally, the aspect ratio (the length of CNT/the diameter of the CNT) was determined for each of the purification methods using capillary breakup extensional rheology [49]. As shown in Figure 3.9, the longer the time or higher the temperature of the oxidation, the shorter the aspect ratio of the resulting CNTs. Moreover, the decrease in aspect ratio with increasing time trends with the mass loss; there is a lev-
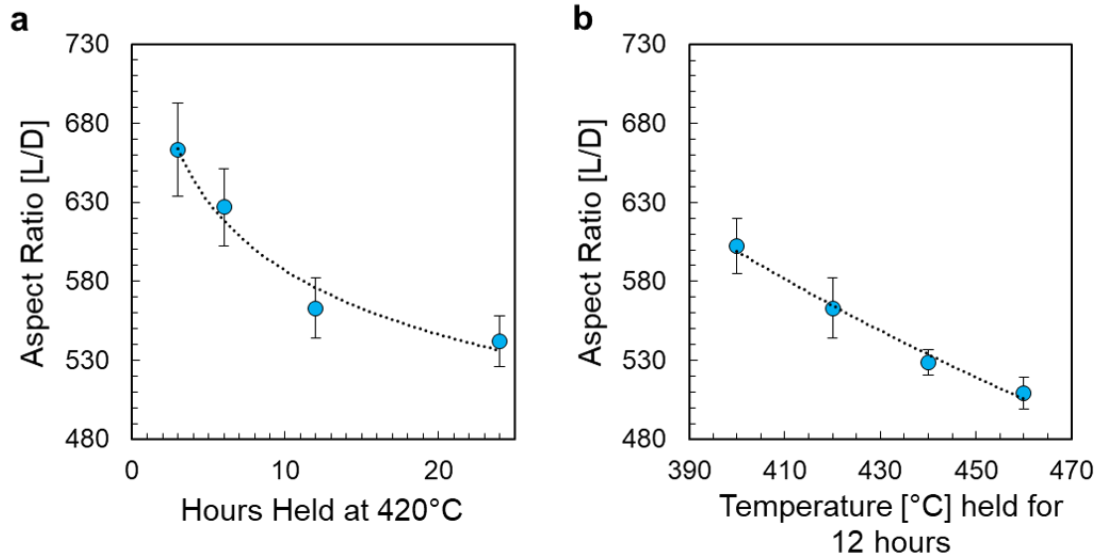
Figure 3.9 : (a) The viscosity averaged aspect ratio of CNTs oxidized at 420 °C for various lengths of time. (b) The viscosity average aspect ratio of CNTs oxidized for 12 hours at various temperatures.

eling off in both the mass loss and aspect ratio with increasing oxidation time. When comparing the mass loss to the decrease in aspect ratio for increasing temperature, we see a similar percentage change in mass loss (($\sim$ 5% and $\sim$ 12%) to the percent change in aspect ratio ($\sim$ 6% and $\sim$ 12%) for 420 °C and 440 °C. However, for the 460 °C purification, we see a much larger change in mass loss ($\sim$ 25%) than change in the aspect ratio ($\sim$ 16%). This suggests that we are not only burning the ends of the CNTs but perhaps amorphous carbon species or entire CNTs. As discussed later in this thesis (Section 5.7), both the purity of the CNTs and the aspect ratio play important roles in improving CNT fiber properties. Therefore, optimizing the oxidation condition is crucial for obtaining the best fiber properties from CNT samples.

3.4 Conclusions

Understanding the underlying mechanism that prevents CNTs from dissolving in superacids is essential for improving the efficiency and lowering the cost of CNT macroscale materials produced through solution processing. We report that oxidation of CNTs removes amorphous material from the sample. This was demonstrated through the increase in Raman G/D ratio and visually through SEM. Furthermore, we did not see evidence that oxidation resulted in the inclusion of additional oxygen in the sidewall of the CNTs. By examining the samples with XPS, we saw an increase in the oxygen content after oxidation, but this was due to the iron catalyst oxidizing to form Fe_2O_3. After removing the iron with HCl, the oxygen content in the sample returned to the initial atomic percentage. Furthermore, the average Raman G/D increased for all samples which indicates that the CNTs remaining in the sample include fewer defects. Finally, we measured the aspect ratio of the CNTs under various purification conditions. The viscosity averaged aspect ratio decreased with increasing purification time and temperature. The optimization of purity and aspect ratio should be considered when selecting purification conditions as these parameters are directly related to the processability and properties of CNTF. By better understanding dissolution, further efforts can be put forth in improving the efficiency of the production and processing of CNTs into CNTF. The adoption of CNTF can have widespread impacts on CO_2 emissions as methane can be used as a precursor material to produce hydrogen fuel and CNTs [52,53]. Furthermore, CNTF has the capability of limiting the emission-heavy process of refining metal ore and reducing emissions by light-weighting cars, planes, and spacecraft. This three–pronged approach to reduce emissions makes CNTs a material that can truly make an impact in fighting climate

change.

Chapter 4

Improved Properties, Increased Production, and the Path to Broad Adoption of Carbon Nanotube Fibers[*]

4.1 Introduction

State-of-the-art carbon nanotube fibers (CNTF) have mechanical and electrical properties that compete with both high-strength fibers (such as aramid or carbon fiber) and metallic conductors, particularly in applications where flexibility or weight savings are primary considerations. Realization of widespread CNTF adoption will require large scale production with controllable and reproducible properties. Following the breakthrough introduction of aqueous suspension CNTF spinning by Poulin's group [8], three main techniques have emerged for producing CNTF on a commercial scale: solution spinning [11], hereafter termed SS-CNTF; direct spinning [55] from floating-catalyst chemical vapor deposition CNT growth reactors, hereafter termed DS-CNTF; and array spinning [10] from supported-catalyst CNT vertical array growth reactors, hereafter termed AS-CNTF. Recently, Stallard et al. showed that the best reported mechanical properties of macroscale CNTF produced from all the methods converge when made into articles with the same density [56]. Despite achieving similar mechanical properties, the fibers and production methods are different in key respects that are important considerations for the future development

---

[*]This chapter is an updated version of a published article [54]

of CNTF.

First, the microstructure and carbon nanotube (CNT) content vary considerably for these production methods. Direct spinning and array spinning tend to yield fibers with relatively low alignment and packing density; however, the constituent CNTs are extremely long ($\sim$0.1 to 1 mm) [55, 57, 58], which is known to contribute to high tensile strengths [12, 51]. Conversely, solution spinning produces a highly-aligned densely-packed microstructure composed of shorter CNTs (so far, below $\sim$10 μm). Direct spinning and array spinning require specialized synthesis methods that yield dry spinnable CNTs, yet the spinning methods work independently of CNT crystallinity and have higher tolerance for impurities such as amorphous carbon. In contrast, solution spinning only requires that the CNTs have high crystallinity (as measured by Raman G to D ratio $> \sim$20), as any impurities can be reduced to acceptable levels through purification prior to processing (low amorphous carbon and < 5wt% residual catalyst) [12]. This means that solution spinning works for a wide range of CNT synthesis methods. These findings have driven the improvement of several CNT synthesis techniques, and relatively long ($\sim$10 μm) CNTs with these characteristics are now available in bulk quantities. Interestingly, the mechanical properties of SS-CNTF are similar to those of DS- and AS-CNTF because the improved microstructure of SS-CNTF appears to improve inter-CNT stress transfer and to compensate for the shorter length of the constituent CNTs [59]. Conversely, the electrical conductivity and thermal conductivity of SS-CNTF significantly exceeds that of DS and AS-CNTF because CNT crystallinity, alignment, and packing affect these properties more than they affect strength – of course, the electrical conductivity of SS-CNTF is also increased by residual acid doping that is inherent in solution processing, while it is often done as a post-processing step for DS and AS-CNTF.

Because the solution spinning process decouples fiber production from CNT growth, it allows for a clear link between raw CNT aspect ratio and CNTF properties [12,59]. The fundamental connection between the properties of the raw CNT material and the properties of the macroscopic fiber reveals a clear path forward: high crystallinity, high aspect ratio, and low impurity CNTs will deliver CNTF that approach individual CNT properties, provided that manufacturing is possible and that the scaling laws hold beyond the regime tested so far. Here, we show that higher quality, longer CNTs can be solution-processed into CNTF with record mechanical and electrical properties while retaining flexibility.

4.2   Results and Discussions
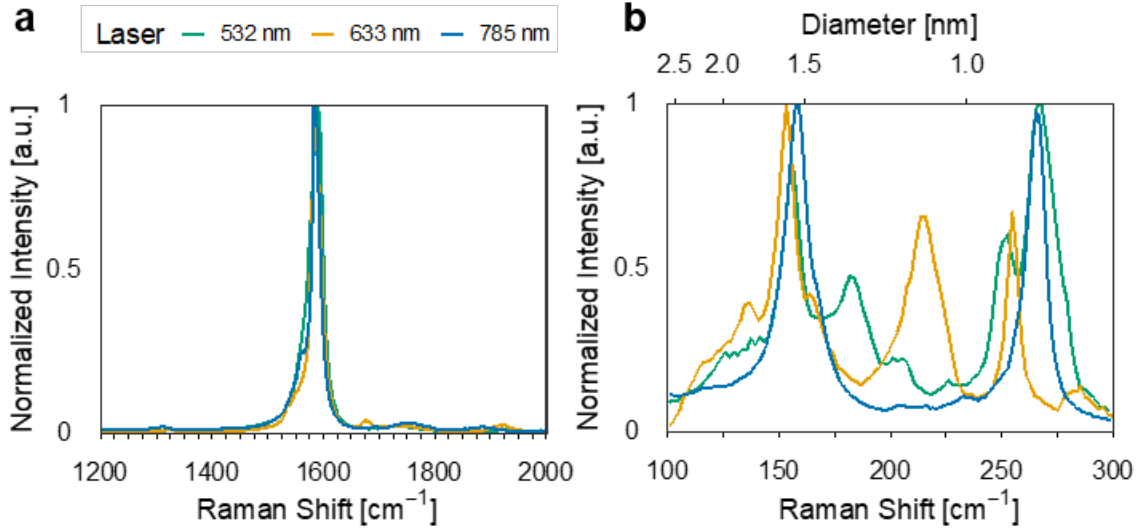
Figure 4.1 : (a) Raman spectra of the raw Meijo 101 CNT material. (b) Raman spectra of the radial breathing mode region showing peaks corresponding to small-diameter CNTs.

The CNTs used here were produced by Meijo Nano Carbon Co. (Meijo EC 101) and spun from chlorosulfonic acid (CSA) (Sigma-Aldrich, 99%), coagulated into acetone and collected onto a rotating drum, as previously described in [11,12]. Additional details can be found in Section 5.2.1. Raman spectroscopy (Renishaw InVia Confocal Raman microscope) was performed on the raw CNT material. Figure 4.1a shows representative spectra of the G and D peaks using 532 nm, 633 nm and 785 nm excitation wavelengths. The average G to D ratio was determined to be 56, 85 and 54 for the 532 nm, 633 nm and 785 nm, respectively, demonstrating the high crystallinity of the CNTs (comparable to the leading material used in Ref [12]). The radial breathing mode (RBM) region of the Raman spectra indicates the presence of 0.8–2 nm single and double walled CNTs (Figure 4.1b). This result was confirmed using high reso-
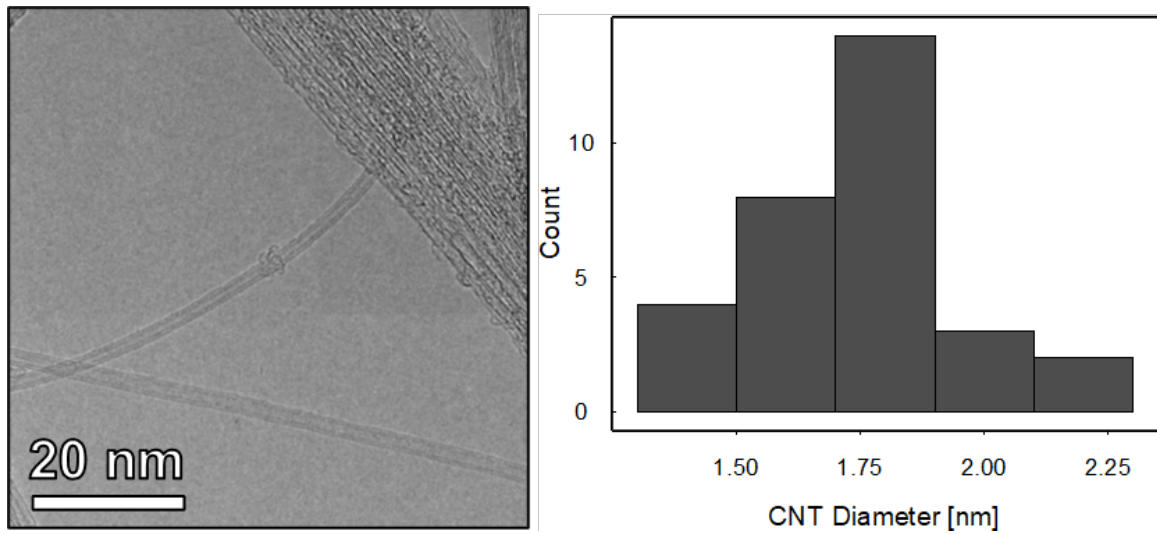
Figure 4.2 : HR-TEM image of the CNTs showing individualized double-walled CNTs. The histogram shows the 31 CNTs measured with HR-TEM showing the diameter distribution, with a minimum of 1.3 nm, a maximum of 2.2 nm, and a mean of 1.76 nm. Images courtesy of O. S. Dewey.

lution transmission electron microscopy (JEOL 2100F FEGTEM) (Figure 4.2) where the average diameter was determined to be 1.76 nm with an average of 1.9 walls. The viscosity averaged aspect ratio of the CNTs was 6700 ($\pm$100), as measured with a capillary breakup extensional rheometer (Trimaster) [49], indicating an average CNT length of $\sim$12 μm. Transmitted (Figure 4.3a) and polarized light (Figure 4.3b)
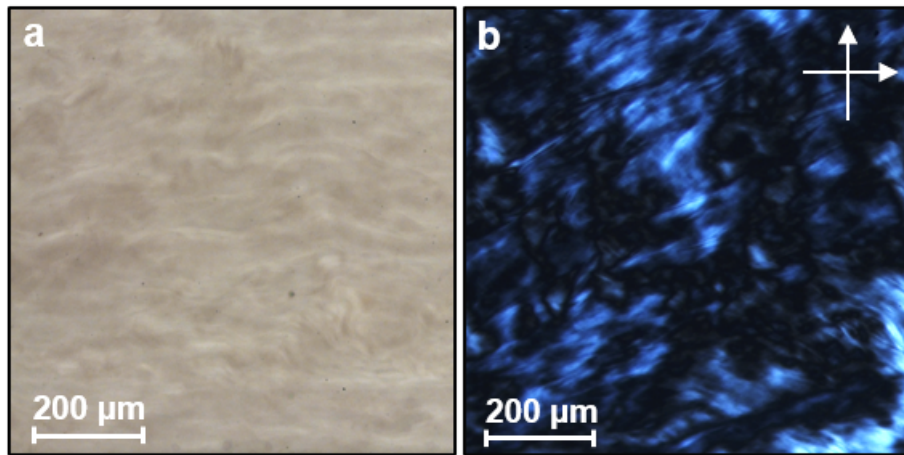
Figure 4.3 : (a) Optical microscope image of a 500 ppmw solution of raw CNTs in CSA (diluted from the spin dope concentration of 5000 ppmw), showing texture and few undissolved impurities. (b) Optical microscope image under crossed polarizers (depicted by the arrows) showing strong birefringence and a Schlieren texture.

microscopy (Zeiss AxioPlan 2) of the CNT/CSA solutions shows that the CNTs are fully dissolved, contain few impurities, and form well defined liquid crystals. The spin dope was too dark to image, so it was diluted from 5000 ppmw to 500 ppmw for solution visualization. Figure 4.4a shows a representative scanning electron microscopy (SEM) (FEI Helios NanoLab 660) image of the surface of CNTF, used to assess morphology and measure the average diameter. The fiber is highly aligned in the axial direction (Figure 4.4b) and has an average diameter of 8.9 $\pm$ 0.9 μm.
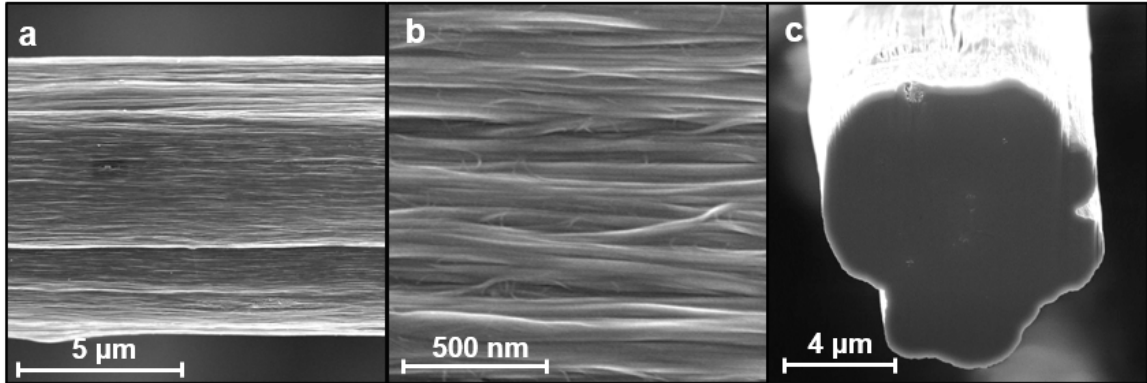
Figure 4.4 : (a) SEM image of the surface morphology of the fiber. (b) High magnification SEM image that depicts highly aligned CNT bundles. (c) Cross-section of the fiber obtained using focused ion beam milling. The fiber is not perfectly round, indicating imperfect coagulation; however, it shows few void spaces indicating a densely packed structure, as in earlier reports [11, 12].

Figure 4.4c shows an SEM image of the CNTF cross–section obtained using focused ion beam milling with an argon source. Although the fiber is not perfectly circular in diameter, the fiber is highly packed with few void spaces. The fiber was characterized for mechanical properties, electrical conductivity, and thermal conductivity. Representative tensile testing curves obtained from an ARES G2 rheometer with tension fixture are shown in Figure 4.5a. Additionally, the tensile strength obtained for each breaking test performed on the fiber were analyzed by fitting to a Weibull distribution (Figure 4.5b). Here, we see that our data is linear except for two data points at the low end of the spread. This suggests that the data is well-represented by a Weibull distribution. The nominal Weibull tensile strength was determined to be 4.2 ± 0.15 GPa. The Young's modulus of 260 ± 40 GPa was calculated from the slope of the tensile stress curve from 0–0.2% elongation. The elongation at break
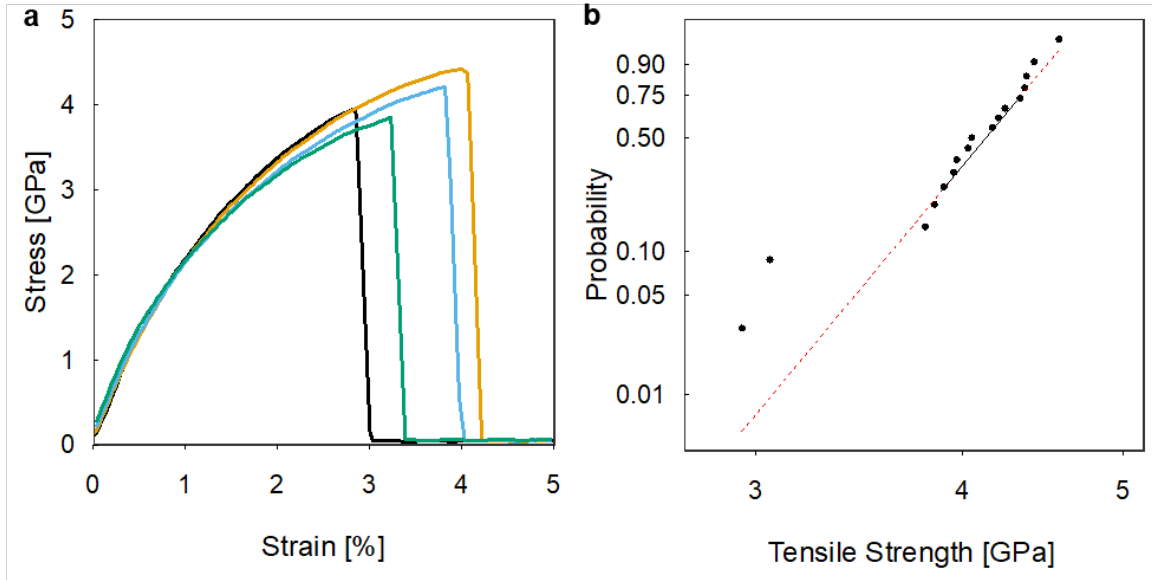
Figure 4.5 : (a) Representative stress-strain curves for the fibers reported here. The four breaking curves shown are each from a different quartile of the data. A total of 17 samples from the same fiber spool were tested. (b) Weibull analysis of the fiber ultimate tensile strengths. Black circles are the tensile strength data for each test performed plotted against the theoretical cumulative Weibull probability distribution for the data. The highest recorded strength (top rightmost point) was 4.57 GPa. The black reference line joins the first and third quartiles of the data and shows where data should lie if the data is from a Weibull distribution. The red dashed lines are extrapolations of the reference line to the minimum and maximum values of the data.

averaged $3.5 \pm 0.65\%$ resulting in an average toughness of 50 ± 14 J/g. Compared to earlier SS-CNTF, we did not find an increase in Young's modulus (reported at $\sim$250 GPa in [68]) but did find a higher elongation to break (reported at 1.5% to 2.0% in [12]). The electrical conductivity of the fiber was measured using an HP34401–A multimeter with a 4–point probe, and the average room–temperature electrical con-
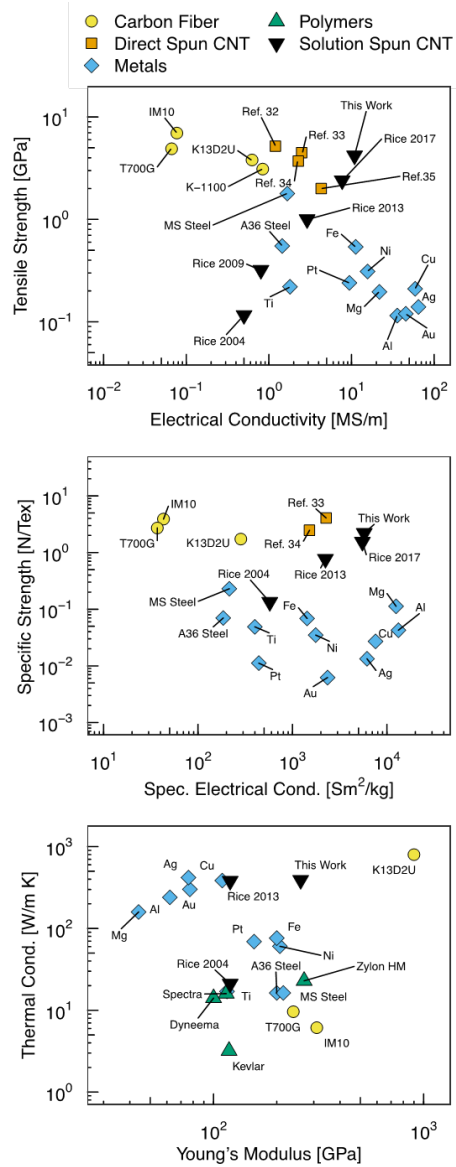
Figure 4.6 : The properties of CNT fiber reported here compared to commercially available carbon fibers (Hexcel IM10 [60], Toray T700G [61], Mitsubishi Dialead K13D2U [62]), metals (where A36 steel is a typical structural steel and MS steel is high strength Martensitic steel), other laboratory produced CNT fibers ([63–66]), and polymeric fibers (Dyneema, Spectra, Zylon HM, Kevlar [67]).

ductivity was 10.9 ± 1.2 MS/m. Although the fibers are p–doped by residual acid, their resistance was stable in laboratory conditions over the 15–month period between the production of the fiber and the submission of ref [54]. The linear density of the fibers (measured vibroscopically [69] at $\sim$35 to 70% of the fiber breaking force) was 1.2 ± 0.1 dtex. This method calculates linear density via a mathematical relation that neglects the effect of intrinsic bending stiffness (which is negligible for CNT fibers due to their low bending stiffness [70]). The specific strength was 2.1 ± 0.3 N/tex and the specific conductivity was 5640 ± 600 S m^2/kg. We used a steady-state fiber heating method [71] to measure a thermal conductivity of 390 ± 60 W/m K at 300 K, comparable to earlier results on SS-CNTF made of $\sim$5 μm CNTs [11]. In this case, the thermal conductivity did not increase with the use of longer CNTs, suggesting that thermal transport may be dominated by intra–CNT transport rather than interfacial resistance between CNTs. Fibers were suspended in vacuum by supporting their ends between silver paste electrodes on a sapphire substrate. The suspended length was measured for each fiber and was in the range of 2.9 to 3.2 mm. A four–point probe method was used to measure the temperature–dependent sample resistance during Joule heating (Keithley 2400) under 2 mTorr vacuum. Thermal modeling shows that convection and radiation losses from the fiber were negligible. Figure 4.6 shows the CNT fiber properties reported here compared to the properties of carbon fibers, DS-CNTF, polymeric fibers, and metals. Consistent with previous reports, SS-CNTF provide an excellent combination of the tensile strength of commercially available carbon fibers and DS-CNTF with the electrical conductivity of metals. However, the specific strength and conductivity of these new SS-CNTF are now within a factor of leading fibers (IM10 for strength and aluminum for electrical conductivity) and on par with the leading fibers for specific thermal conductivity (K13D2U). We plotted
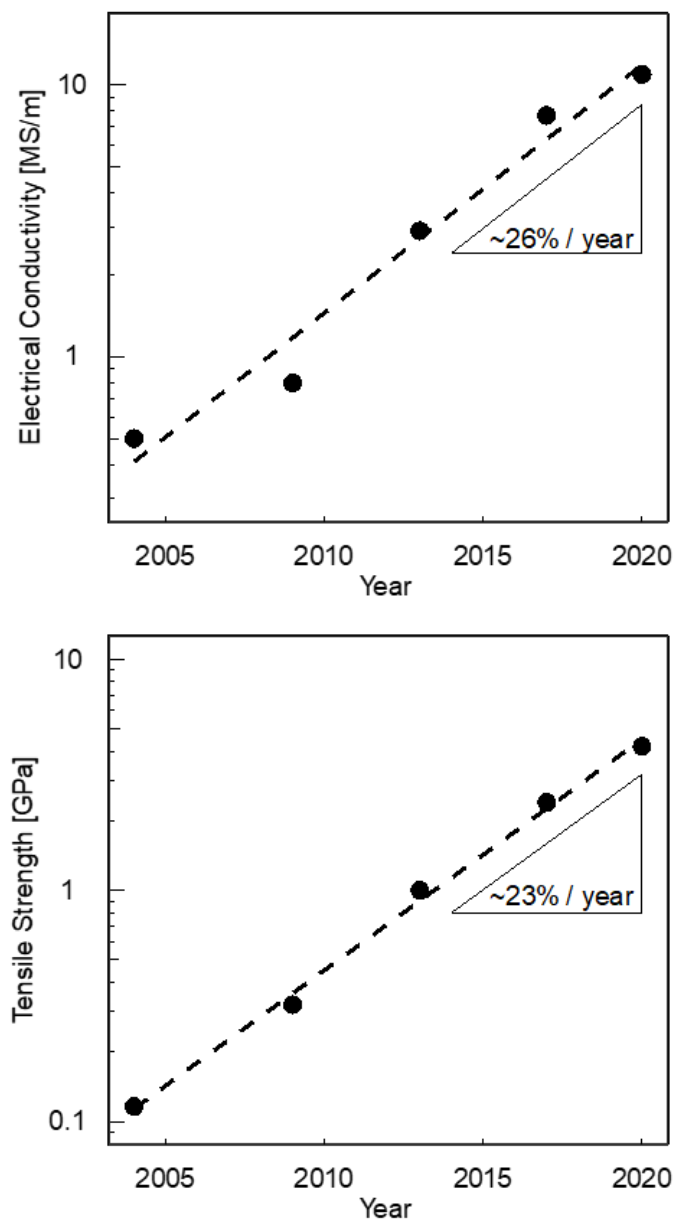
Figure 4.7 : The improvement in electrical conductivity and tensile strength of solution spun CNT fibers at Rice University over time. The properties have been improving on average over 20% per year.

property improvements vs. time for SS-CNTF (Figure 4.7) and noted that electrical conductivity and tensile strength have been growing by $\sim$20 to 25% per year, i.e., they doubled every three years, while thermal conductivity seems to have plateaued at $\sim$400 W/m K. Because the theoretical limits are $\sim$100 MS/m for conductivity [72] and $\sim$40 GPa for tensile strength [73] (an order of magnitude away from current properties) another doubling of properties could be achievable in 3 to 5 years. SS-CNTF would then be stronger than any other fiber material and as electrically and thermally conductive as most metals.

4.3   Conclusions and Future Outlook

CNTF technology has advanced dramatically in the two decades since the revolutionary spinning of the first continuous fibers [8] – which amazingly was achieved within a decade after the material was discovered and within five years of the first gram–level production [18, 74, 75]. For comparison, it took nearly a century from the production of the first carbon filaments by Joseph Swan and Thomas Edison to the development of high-strength carbon fibers by Roger Bacon [76–78]. Continued research has led to CNT fibers with competitive properties at increasing scale of production, which is essential for the broad adoption of CNT materials. Moreover, CNTF appear to have other advantages over conventional fibers. A knot strength of 100% (related to flexibility and likely high compression strength) has been reported by multiple authors [10, 79]. CNTF have demonstrated promising performance in composites as well. In one report, CNTF composites retained 69% of the specific strength of the CNTF, compared to 45% retained for IM7 carbon fiber, the leading commercial product [80]. Likewise, CNTF composites are competitive with IM7 composites in certain applications, such as pressure vessel overwraps [81]. Recently,

Xie et al. demonstrated that SS-CNTF have superior dynamic tensile strength to aramid fibers under supersonic impacts, despite lower static tensile strength. Their work demonstrates that the failure mechanism includes molecular CNT damage under such conditions, indicating that higher fiber strengths can be achieved through better coupling between the constituent CNTs [82]. In fact, Bai et al. demonstrated that the tensile strengths of bundles of CNT spanning the whole testing gap exceeds 40 GPa, as the bundles fail via the breaking of the constituent CNTs [73].

Challenges still remain for CNTF to become a viable substitute for polymeric and metal materials; the production rate of CNTs must increase and the overall cost of the material must significantly decrease. Companies such as OCSiAl, Meijo Nano Carbon, Huntsman Corporation (formerly NanoComp), Tortech, Muratec, DexMat, and Lintec NSTC, as well as their academic counterparts, are continuously working to improve quality and lower production costs; LG Chem is a major CNT producer with recent research and developemnt efforts in CNTF production demonstrating very high specific strengths [83]. As of 2019, the annual production of fiber-grade CNTs is ∼100 tons at sale prices of ∼$2,000 to $100,000/kg; production costs are significantly lower. Although total production is still small, it represents about two orders of magnitude increase in capacity and about two orders of magnitude price reduction in the past five years. At the low end, production cost is now within one order of magnitude of the typical cost required for widespread material applications (carbon and aramid fibers are ∼$10 to $200/kg depending on properties and are produced at ∼100,000 ton/yr). The property improvements and increase in production of CNTs and CNTF, as demonstrated here, have been remarkable. No other material has the combination of strength, thermal and electrical conductivity, and flexibility offered by CNTF. The use of CNTF for a wide range of applications, from biomedical devices

to next generation wiring and cables, is only just beginning. By expanding and improving collaboration between academic and corporate partners, this progress can be accelerated further. Ultimately, these efforts will bring to market a new class of affordable, high performance materials with transformational properties.

Chapter 5

Key Process Parameters for Solution Spun Carbon Nanotube Fibers

5.1   Introduction

As mentioned in the previous chapter, solution spinning has several benefits over other CNT fiber production methods. One of the most important advantages of so-

Fiber Collection
● Collection Rate (Draw Ratio)

Dope Properties
● CNT Concentration
● CNT Aspect Ratio (L/D)
● CNT Purity
● CNT Quality (G/D)
● Dope Temperature
● Solvent

Spinneret Properties
● Extrusion Rate
● Diameter
● Spinneret Geometry
● Exit Conditions

Coagulation Conditions
● Coagulant
● Bath Length
● Solvent Concentration
● Temperature
● Bath Orientation
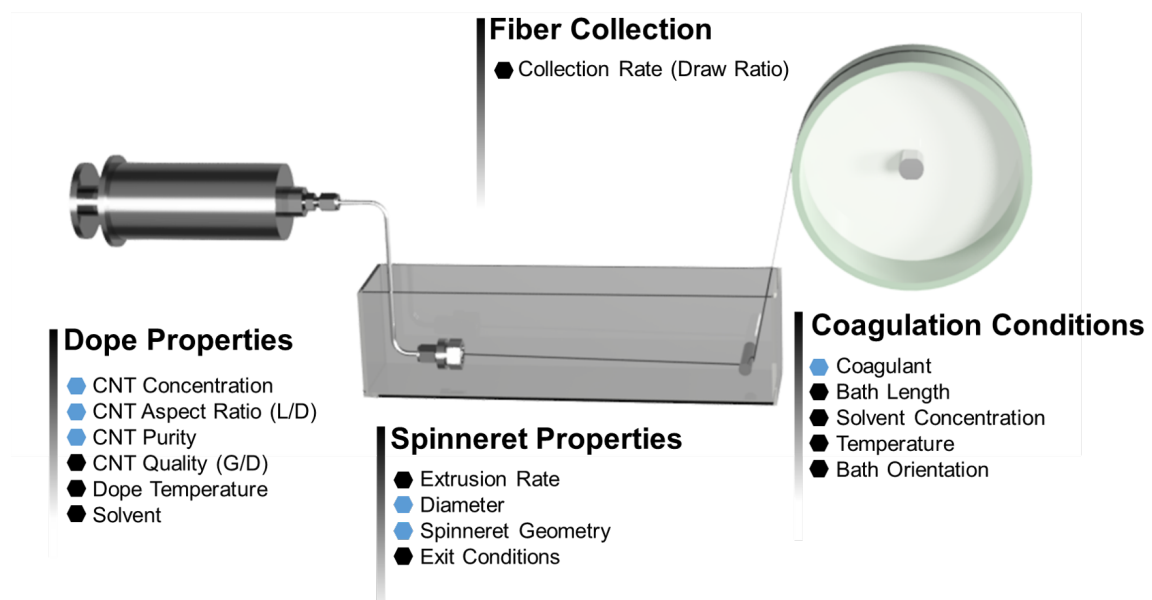
Figure 5.1 : Diagram of CNT fiber spinning process parameters. Process parameters discussed in the chapter are highlighted in blue.

lution spinning is that this method has already been shown to successfully scale up production of high performance fibers such as polyacrylonitrile (precursor for carbon

fiber), Kevlar® and other aramid fibers, and Dyneema®. However, to fully scale up CNT fiber production, a deep understanding of the system is necessary as fiber properties, process consistency, process efficiency, environmental impact and production cost are important considerations. Unfortunately, the CNT process parameter space is vast and complex consisting of fluid flow of a complex fluid, mass transfer and chemical reactions within the coagulation bath, and large sample to sample variation of the constituent CNTs. Some of the key processing parameters can be seen in Figure 5.3 where the parameters discussed in this thesis are highlighted in blue. This chapter focuses on developing a clearer understanding of how key parameters affect fiber processing with the aim to improve process efficiency and overall fiber properties. In particular, this chapter discusses the effect of:

- post-processing on the stability of fiber electrical conductivity,

- the coagulant on fiber morphology and process efficiency,

- spinneret geometry and diameter on fiber coagulation,

- variances in CNT properties such as purity and aspect ratio on fiber performance, and

- the concentration of CNTs in the spin dope on fiber structure.

5.2 General Fiber Spinning Methods

5.2.1 Carbon Nanotube Fiber Spinning Process

The fiber spinning process is shown in Figure 5.2. CNTs (Meijo Nanocarbons) were purified by thermal oxidation (Thermolyne, Thermo Scientific) to remove carbon impurities and washed in hydrochloric acid (HCl 37%, Sigma-Aldrich) as needed for
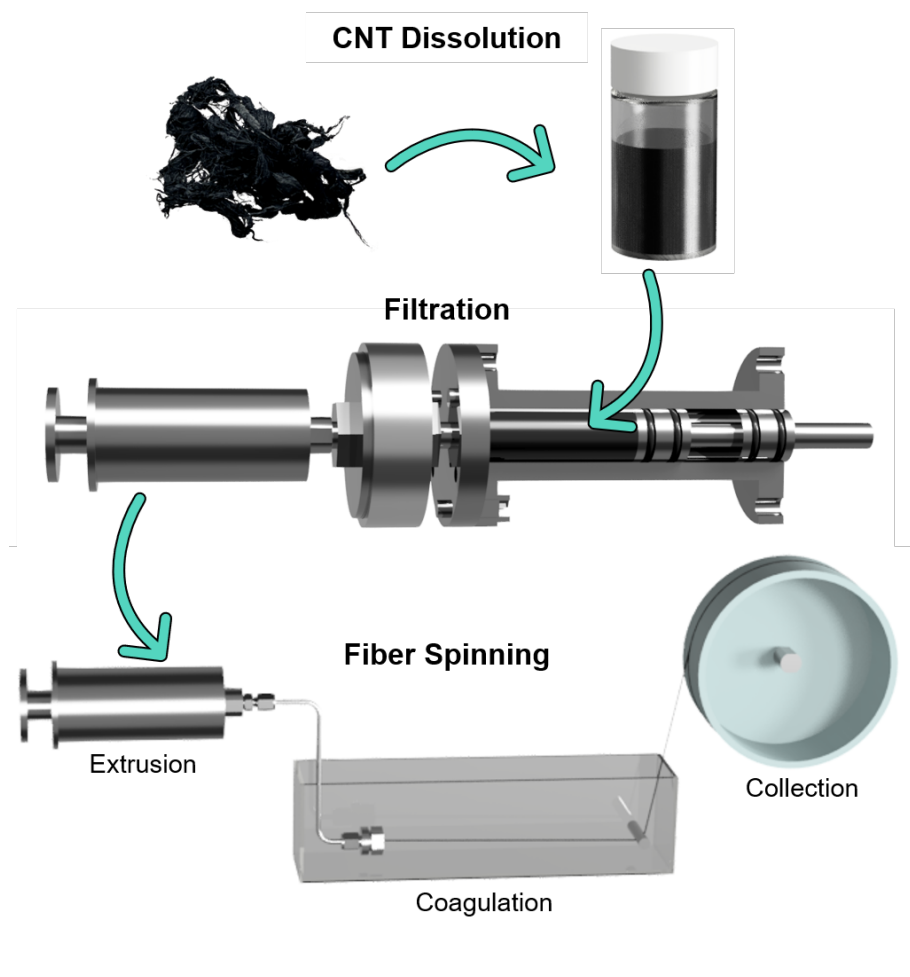
Figure 5.2 : Diagram showing the fiber spinning process. First, CNTs are dissolved in CSA. The solution is filtered to remove undissolved particles. Finally, the solution is extruded through a spinneret into a coagulation bath and collected onto a rotating drum.

dissolution into chlorosulfonic acid (CSA). CNTs and CSA were mixed at the desired concentration (0.25 wt% - 10 wt%) in a speed mixer (Flaktech) for 2 hours to form the spin dope. The dope was loaded into a 316 stainless-steel chamber and filtered through a 500-mesh stainless steel filter into a syringe. This filtration process removes

any large undissolved particles that can potentially clog the spinneret. The dope filled syringe was connected to a 1/8" tube fitted with a spinneret. The spinneret had a single, 150 μm diameter hole unless otherwise specified. The syringe was loaded into a syringe pump (Harvard Apparatus) and the spinneret was placed into a coagulation bath (typically acetone - HPLC grade, Sigma Aldrich). The dope was slowly extruded into the coagulation bath at 0.009 mL/min to 0.36 mL/min (corresponding to a linear extrusion of 0.5 m/min to 2 m/min). Next, the CSA diffused away from the liquid filament causing the CNTs to hold together via van der Waals forces to form a stable fiber. Finally, the fiber was collected onto a rotating drum. The ratio between the drum speed and the extrusion speed, called the draw ratio, was optimized for each set of experiments.

5.2.2   Carbon Nanotube Fiber Characterization

CNT fiber was characterized for surface morphology, engineering strength, specific strength, electrical conductivity, specific conductivity, and linear density. Scanning electron microscopy (SEM) (FEI Quanta 400 ESEM) was used to measure CNT fiber diameter and view surface morphology. Samples were obtained from 1 cm pieces of fiber from 4 sections of fibers spanning 3 meters in length. Break force was measured using an ARES G2 rheometer (TA Instruments) with a rectangular tension fixture. The average break force was obtained from at least 10 samples of fiber using a 20 mm gauge length at a speed of 0.1mm/sec. The resistance of the CNTF was measured using a 4-point probe (HP34401) with a 7 cm spacing. An average resistance was obtained from 10 measurements over several meters of fiber. The linear density was obtained by measuring a known length of fiber (typically 2-4 meters) on a microbalance (Citizen, CM 21 X) or by using a vibroscopic method

described in Ref [69].

5.3 Stabilization of Carbon Nanotube Fiber Electrical Conductivity

Many high performance solution spun fibers such as polyacrylonitrile (PAN) based carbon fiber or aramid fibers utilize additional washing steps after the coagulation bath to remove excess solvent [84]. This step is important because excess solvent can degrade the polymers [36]. Previous studies in the Pasquali lab indicated that additional processing steps were needed after spinning to ensure stable electrical conductivity over long periods of time [68]. Post treatment steps (shown in Figure 5.3) were developed to remove any volatile acid dopant still present in the fiber after spinning. This section explores the stability and overall resistance of CNT fiber over a 3 year time period for as-produced fibers and different post-treatment techniques. These treatments include water washes, additional coagulant washes, and heat treatments.

5.3.1 Experimental Details

Meijo 1.5 P (Lot 8302305) was dissolved at 1 wt% in CSA. The mixed dope was extruded at 0.36 mL/min (2.0 m/min) into a coagulation bath of acetone and collected onto a rotating drum at 3.0 m/min. A few meters of the as produced fiber was taken off of the drum and taped into a Manila file folder (Pendaflex) and the resistance was measured with a 4 point probe (HP34401) with a 7 cm distance. The drum with the remaining fiber was then soaked in distilled water for 30 minutes at room temperature. A few meters of fiber was taken off of the drum and taped into another file folder. Next, the drum with the remaining fiber was then placed in an
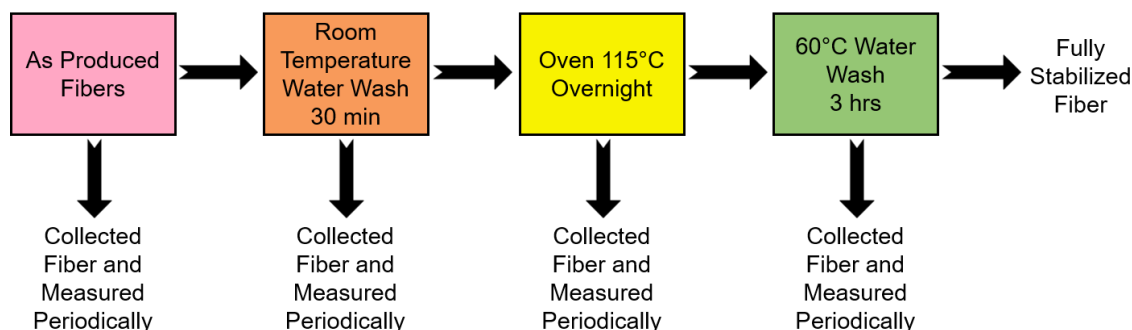
Figure 5.3 : Flowchart of the fiber stabilization procedure. As produced fiber is washed with room temperature water, heated in an oven at 115 °C overnight, and washed with 60 °C water for 3 hours. Fiber was collected after each step, and the resistance was measured periodically.

oven at 115 °C overnight in air. Once again, a few meters of fiber was taken off of the drum and taped in a file folder. Finally, the drum was washed in 60 °C water for 3 hours, and a few meters of fiber was taped into a file folder. A flow diagram of this described process is shown in Figure 5.3. The file folders of fiber were stored at ambient lab conditions and the resistance of the fiber at the various conditions was measured periodically spanning a time period of 3 years.

A similar procedure was followed to study the effect of washing fiber in coagulant (acetone) rather than distilled water. Fibers were produced as described above. A few meters of as produced fiber was taped into a folder. The drum of fiber was then soaked in a bath of clean acetone for 30 minutes. Again, a few meters of fiber was taped into a drum. Finally, the drum of fiber was heated at 115 °C overnight in air and fiber was collected and taped into a file folder. As described previously, the resistance of the fiber was measured periodically. This process is shown in Figure 5.4.
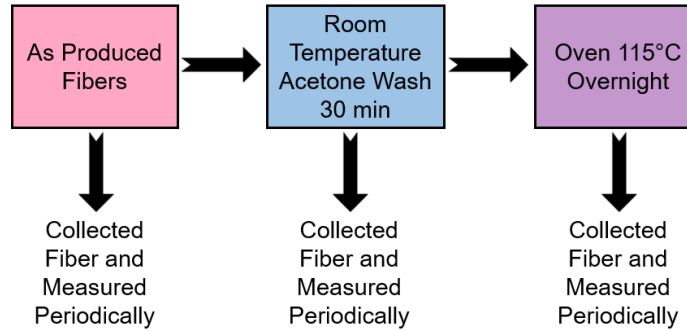
Figure 5.4 : Flowchart of the fiber stabilization procedure using acetone as a washing medium. As produced fiber is washed with room temperature acetone and heated in an oven at 115 °C overnight. Fiber was collected after each step, and the resistance was measured periodically.

5.3.2 Results and Discussions

As described in the experimental methods and shown in Figure 5.3, fiber was collected after each step in a series of post-processing procedures and the resistance was measured over time. The resistance was measured directly after production, 1 day after production, a few days after production, 1 year after production, and 3 years after production. These results are plotted in Figure 5.5. The as produced fiber and water washed fiber are significantly less resistive than the fibers that underwent heat treatment (labeled as "heated" and "hot water" in Figure 5.5) over the entire course of the study. The percent change from the initial resistance measurement of the as produced fiber after 1 day and 3 years in shown in Figure 5.6. We see a small increase (∼2.6%) in the resistance for the as-produced fiber. However, this is within the error of the resistance measurements. After water washing, we see a decrease in the resistance of ∼8% in comparison to the as produced fiber. After 3 years,
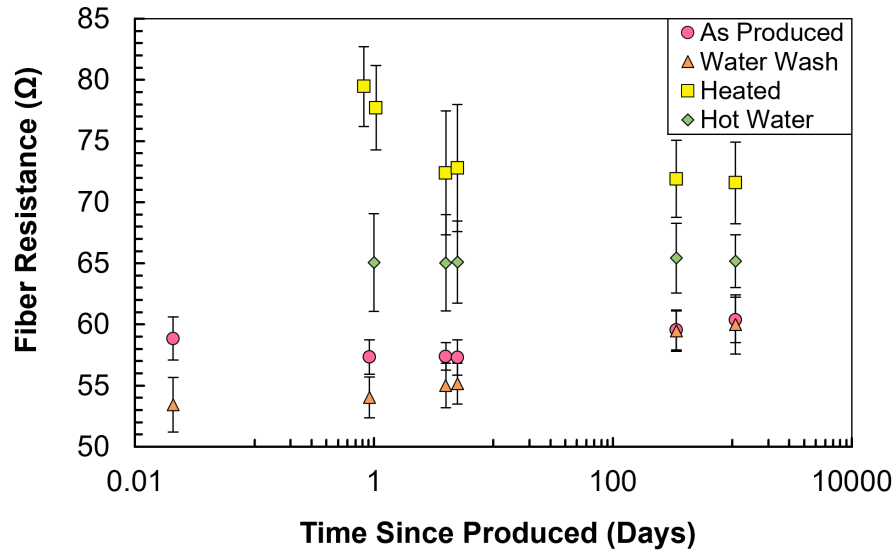
Figure 5.5 : Fiber resistance over time for as produced fiber (pink circle), water washed fiber (orange triangle), heat treated fiber (yellow square), and hot water washed fiber (green diamond).

the resistance increased and is nearly identical to the as-produced fiber. After heat treating the fiber, the resistance initially increases over 32%. However, by washing the heat treated fiber in warm water, the conductivity can be partially recovered. This is because the heat treatment partially drives off residual acid as well as absorbed water. The acid is permanently removed in the heating process leading to an unrecoverable increase in resistance. Water, on the other hand, can be reabsorbed into the fiber through the hot water wash process. Figure 5.7 shows the percent change in resistance of each fiber over time. The hot water treated fiber is highly stable over the 3 year period. The resistance of the heat treated fiber decreases, particularly in the first several days after post processing, due to the absorption of water into the fiber. Finally, we see good stability for the as-produced fiber and improved resistance at
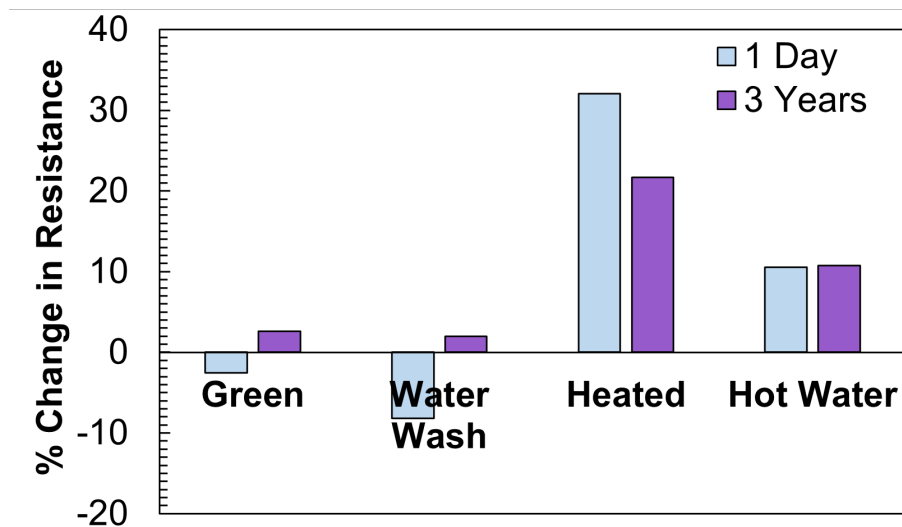
Figure 5.6 : Percent change in resistance of post-processed fiber compared to as produced fiber after 1 day and 3 years.
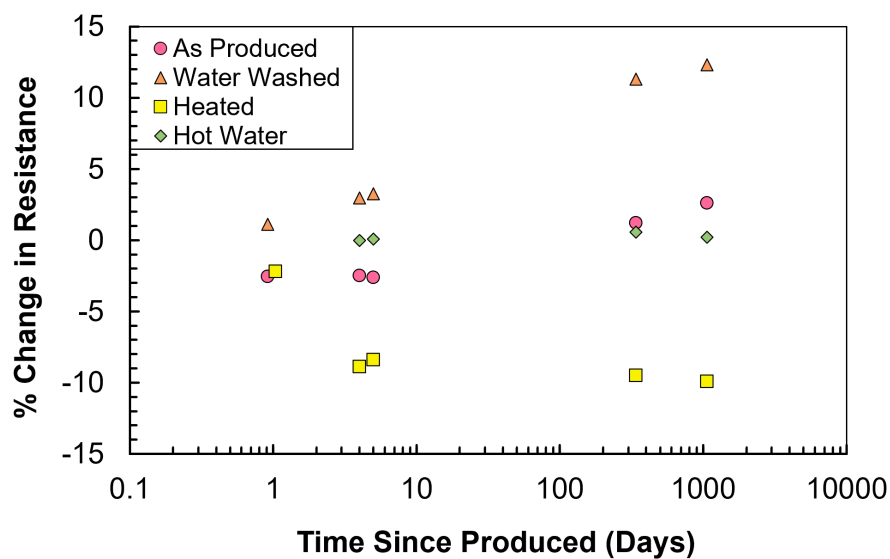
Figure 5.7 : Percent change in fiber resistance from the first measurement over time for as produced fiber (pink circle), water washed fiber (orange triangle), heat treated fiber (yellow square), and hot water washed fiber (green diamond).
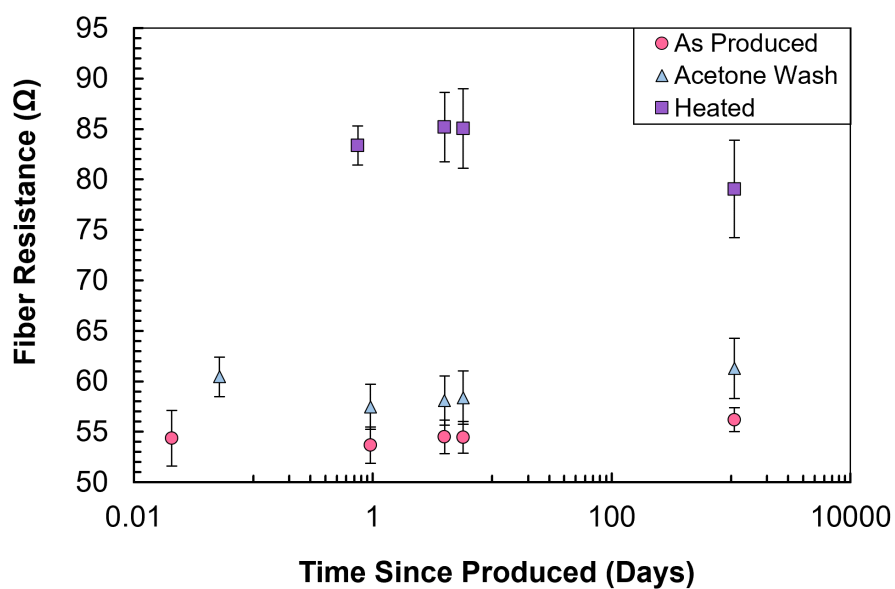
Figure 5.8 : Fiber resistance over time for acetone stabilization method for as produced fiber (pink circle), acetone washed fiber (light blue triangle), and heat treated fiber (purple square).
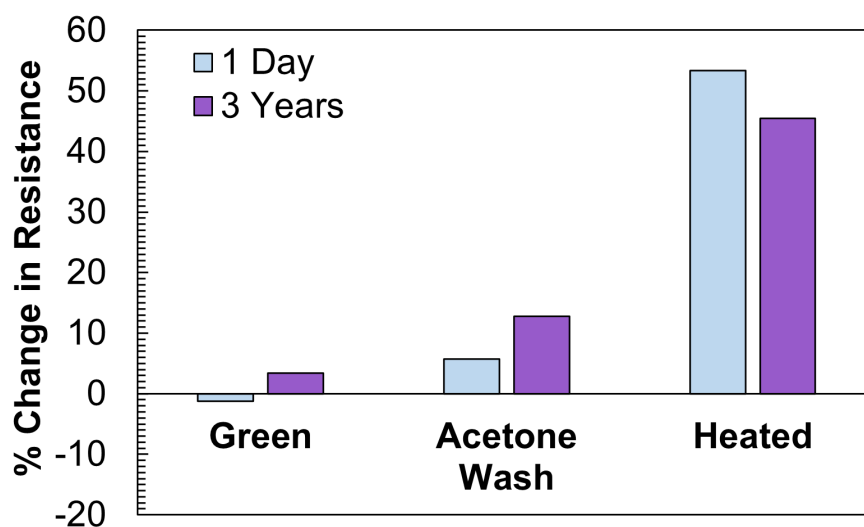
Figure 5.9 : Percent change in resistance of acetone washed fiber compared to as produced fiber after 1 day and 3 years.

room temperature.

Fibers were also washed in fresh coagulant to remove residual acid and heated to remove any residual volatile material. The resistance over time is shown in Figure 5.8, and the change in resistance compared to the initial as produced fiber measurement is in Figure 5.9. Similar to the previous study, the as produced fiber is relatively constant over time. After washing with acetone, the resistance after 1 day was $\sim6\%$ higher and increased to $\sim13\%$ more resistive after 3 years. Finally, heating the acetone fiber led to over a 50% increase in resistance. However, the resistance decreased slightly over time due to the reabsorption of water into the fiber. Overall, additional washing in acetone does not improve stabilization and resulted in an overall lower conductivity.

5.4   Choice of Coagulant and Coagulant Longevity

CNT fibers can be used to replace carbon fiber to lightweight cars, airplanes, and spacecraft to limit fuel usage. They can also provide additional weight savings in these vehicles by replacing copper and aluminum; this replacement would have further environmental impacts as copper and aluminum mining is an extremely CO_2 and energy intensive process [85]. However, to realize the full benefits of the material, the efficiency of the fiber spinning process needs to be improved.

One particularly inefficient step of the spinning process is the coagulation step. Currently, acetone has been shown to be the best coagulant for solutions of CNTs in CSA for fiber performance [11, 47]. When evaluating acetone in terms of process efficiency, it has a number of issues. As a flammable and volatile organic solvent, it poses process safety concerns. More importantly, acetone and CSA react to form polymeric compounds. As this reaction proceeds, the coagulation bath discolors to yellow and eventually dark red. Once the acetone and CSA reacts, it is difficult to

separate the CSA from the acetone and polymeric species. This means the coagulant and solvent cannot be recycled and reused causing a big waste disposal issue. Additionally, the coagulant strength decreases with progression of the CSA/acetone reaction which decreases fiber performance.

This section explores the effect of various coagulants on the properties of CNT fibers. Acetone with ammonium acetate was explored to inhibit the reaction of CSA with acetone. Diethyl ether was studied due to its limited reactivity with CSA and slow rate of coagulation. Methyl ethyl ketone (MEK) and diethyl ketone (DEK) were tested as they are chemically similar to acetone. Finally, water was studied as it is the best coagulant from a process standpoint since it is inexpensive, safe, and easy to recycle. Although water is the best from an efficiency standpoint, it reacts readily and violently with CSA. This reaction produces gaseous HCl which, in standard spinning conditions, destroys the alignment of the fiber and produces a porous, low performance material.

5.4.1 Experimental Details

Meijo 1.5 P (Lot 7110205) was dissolved at 2 wt% in CSA. A syringe pump, short coagulation bath (∼40 cm of coagulation length), and collection motor with drum were placed into the fume hood. Dope was extruded through a single 150 μm spinneret at 0.036 mL/min corresponding to a linear rate of 2.0 m/min. Fibers were produced at a draw ratio of 1.2 and a maximum draw ratio (1.5). The maximum draw ratio was determined by slowly speeding up the collection drum until the filament broke. The collection drum was then set to a speed slightly below where the filament broke. The ratio between this drum speed (as measured by a CyberTech tachometer) and the extrusion speed is the maximum draw ratio. After fibers were produced

Figure 5.10 : Photograph of the spinning setup in the fume hood. The coagulation bath is filled with 80 vol% diethyl ether and 20 vol% water.

with the desired coagulant, the bath was drained, dried, and filled with the next coagulant. Between coagulants, the dope was left extruding in air to prevent the spinneret from clogging. The coagulants used in this study were acetone (HPLC grade, Sigma-Aldrich), acetone with 60 mL distilled water ($\sim$5 vol% water), acetone with 60 mL of 4 M ammonium acetate ($\geq$97%, Fisher Scientific), diethyl ether ($\geq$99%, Fisher Scientific), diethyl ether with 20 vol% water, and methyl ethyl ketone ($\geq$99%, Sigma-Aldrich). The coagulant and draw ration can be found in Table 5.1.

Additionally, Meijo EC DX303 (Lot 5R80C25C) was dissolved at 3 wt% in CSA and extruded at 0.18mL/min through a single 150 μm spinneret. (The extrusion rate was reduced due to filament breakage.) The fiber was coagulated in a warm (30 °C) bath of acetone with 200 mL of 1.5 M ammonium acetate at a draw ratio of 1.3. Fiber was collected at various increments to determine fiber properties over time.

Meijo EC DX303 (Lot 5R80C25C) was dissolved at 1 wt% in CSA, and the spinning setup was placed into a fume hood. Dope was extruded at a rate of 0.36 mL/min through a single 150 μm spinneret into a bath of acetone (HPLC grade, Sigma-Aldrich) or DEK ($\geq$99%, Sigma-Aldrich). The fiber was collected at a draw ratio of 1.3 and 1.5.

For fibers produced with a water coagulant, Meijo ECL 1.5P (Lot 8602905) was dissolved at 5 wt% and at 1 wt% in CSA. Dope was extruded at a rate of 0.36mL/min through single 150 μm spinneret into a bath of distilled water. A jet of distilled water was aimed at the face of the spinneret. Due to the short length of the fibers, the diameter was measured with an optical microscope (Zeiss Axioplan).

Finally, all fibers were characterized as described in Section 5.2.2.

5.4.2   Results and Discussions
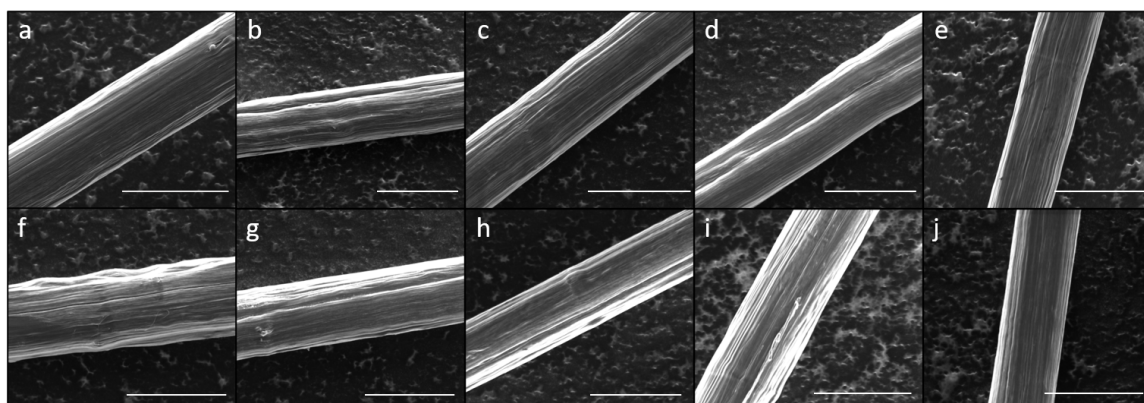
Figure 5.11 : Scanning electron microscopy images of fibers coagulated in (a) acetone, (b,c) acetone with 5 vol% water, (d,e) acetone with 5 vol% 4 M ammonium acetate, (f) diethyl ether, (g,h) diethyl ether with 20 vol% water, and (i,j) methyl ethyl ketone. Scale bars are 30 μm.

Fibers were produced with various coagulants using the same CNT spinning dope under the same spinning conditions (spinneret, extrusion rate, and draw ratio). The fiber produced in acetone, the standard choice of coagulant, was used as a control. Fibers were also produced at a maximum draw ratio to optimize the spinning conditions for each coagulant. SEM images of the fibers produced with acetone, acetone with 5 vol% water, acetone with 5 vol% 4 M ammonium acetate, diethyl ether, diethyl ether with 20 vol% water, and MEK are shown in Figure 5.11. Fibers coagulated in
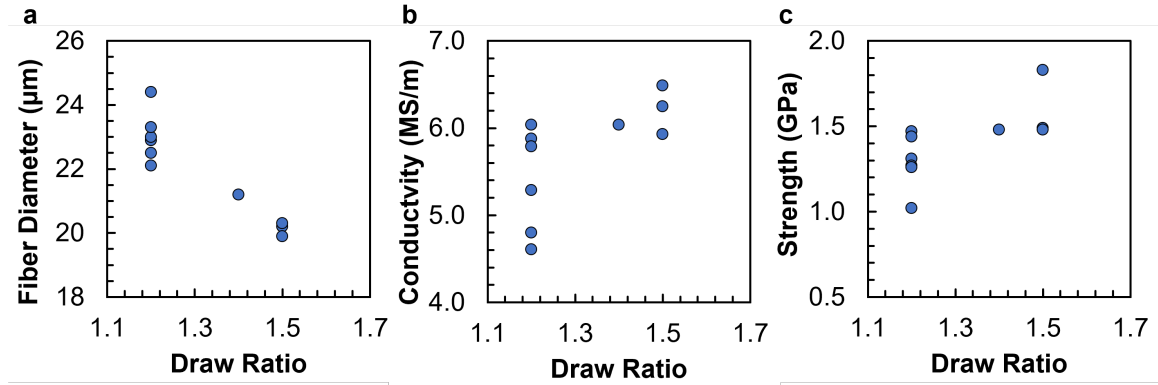
Figure 5.12 : (a) Fiber diameter, (b) electrical conductivity, and (c) tensile strength for fibers produced in various coagulants as a function of draw ratio.

acetone (Figure 5.11a) and MEK (Figure 5.11i and j) have a smooth, cylindrical surface even at low draw (1.2). Fibers coagulated at low draw in mixtures of water and acetone (Figure 5.11b and d), diethyl ether (Figure 5.11f), and water and diethyl ether (Figure 5.11g) show some surface roughness and misalignment of CNT bundles indicating sub-optimal processing conditions. At a higher draw ratio, a better fiber morphology is obtained for the mixtures of water and acetone (Figure 5.11c and e), and water and diethyl ether (Figure 5.11h). However, fibers could not be produced at a higher draw ratio when coagulated in pure diethyl ether due to the filament break-

age. Furthermore, the fiber properties (diameter, electrical conductivity, and tensile strength) as a function of draw ratio is shown in Figure 5.12. As expected, when
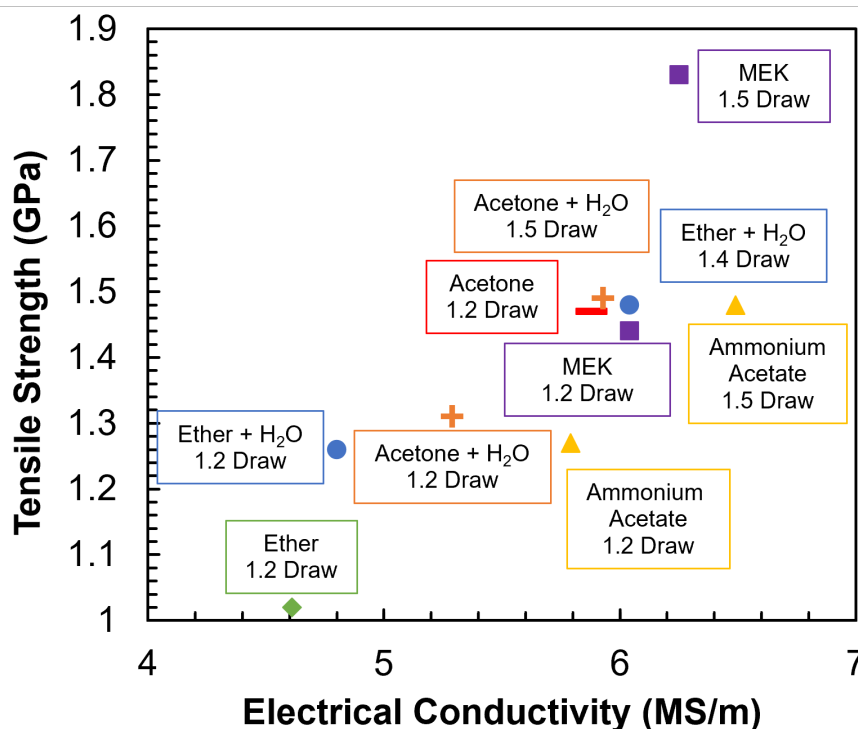
Figure 5.13 : Tensile strength vs electrical conductivity for fiber produced with various coagulants.

increasing the draw ratio, the filament stretches further, resulting in a decrease in fiber diameter. Additionally, the properties tended to improve with increasing draw ratio regardless of the coagulant used. The tensile strength and electrical conductivity for each coagulant and draw ratio is shown in Figure 5.13. When at the same draw ratio, there is not a significant difference in fiber properties between acetone and MEK. However, there is a significant decrease in performance when using diethyl ether as a coagulant. Diethyl ether is a slower acting coagulant. By adding water to the diethyl ether, we are able to speed up the coagulation process as water reacts

Coagulant	Draw Ratio	Diameter (μm)	Electrical Conductivity (MS/m)	Tensile Strength (GPa)
Acetone	1.2	22.5±1.8	5.9±0.9	1.5±0.3
Acetone + 5 vol% Water	1.2	22.9±2.2	5.3±0.7	1.3±0.3
Acetone + 5 vol% Water	1.5	20.2±1.3	5.9±0.7	1.5±0.2
Acetone + 5 vol% 4 M Ammonium Acetate	1.2	22.1±0.9	5.8±0.9	1.3±0.1
Acetone + 5 vol% 4 M Ammonium Acetate	1.5	19.9±1.0	6.5±0.5	1.5±0.2
Diethyl Ether	1.2	24.4±3.0	4.6±0.7	1.0±0.3
Diethyl Ether + 20 vol% Water	1.2	23.0±1.0	4.8±0.7	1.3±0.1
Diethyl Ether + 20 vol% Water	1.4	21.2±1.6	6.0±0.6	1.5±0.3
Methyl Ethyl Ketone (MEK)	1.2	23.3±1.2	6.0±0.5	1.4±0.2
Methyl Ethyl Ketone (MEK)	1.5	20.3±2.1	6.3±1.1	1.8±0.4

Table 5.1 : Diameter, electrical conductivity, and tensile strength of fibers spun in various coagulants

readily with CSA. We see a fairly significant improvement in fiber properties with the diethyl ether and water mixture in comparison to pure diethyl ether. This decrease in performance with a slower acting coagulant indicates that the structure of the fiber is formed within the spinneret rather than along the length of the bath. Finally, a small quantity of water was added to acetone to study the use of ammonium acetate to inhibit the reaction between CSA and acetone. The water was necessary because ammonium acetate is insoluble in acetone.

There was a small decrease in tensile strength for the fiber coagulated in acetone and water and acetone and ammonium acetate. However, the fiber coagulated in the acetone and ammonium acetate bath performed similar to the acetone (control) fiber. Importantly, there was no noticeable color change with the acetone and ammonium acetate bath meaning that there was no significant production of polymeric compounds. A summary of the fiber properties from each set of spinning conditions can be found in Table 5.1.

The acetone and ammonium acetate bath demonstrated promising initial results for increasing the longevity of the coagulation bath. To demonstrate that the ammonium acetate inhibits the CSA/acetone reaction, fiber was spun over an extended period of time (5 hours), and the fiber properties were measured periodically. Additionally, the acetone/ammonium acetate bath was heated to ~ 30 °C as the rate of reaction between the CSA and acetone increases with increasing temperature. The properties of the sampled fibers, shown in Figure 5.14, demonstrate that the conductivity and tensile strength did not change over time. This indicates that the coagulant bath did not degrade over the 5-hour experiment. Furthermore, we confirmed these results visually throughout the course of the experiment. Pristine acetone is transparent. However, as the CSA and acetone reacts, the coagulation bath turns yellow
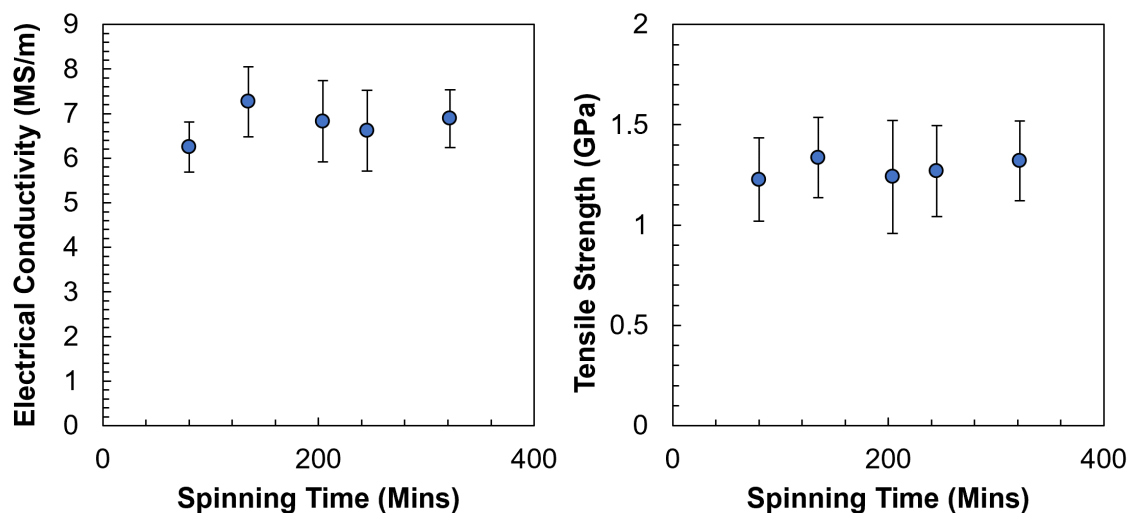
Figure 5.14 : Electrical conductivity (left) and tensile strength (right)for fiber co-agulated in acetone and ammonium acetate over time. The properties are constant indicating that the coagulant bath did not degrade.
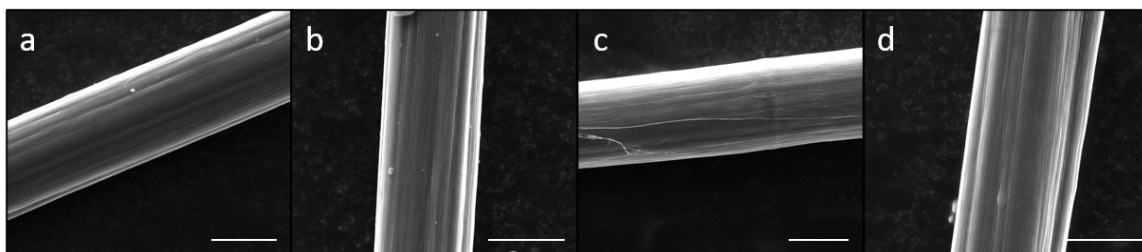
Figure 5.15 : Scanning electron microscopy images of fibers coagulated in (a) acetone at 1.3 draw, (b) acetone at 1.5 draw, (c) diethyl ketone at 1.3 draw, and (d) diethyl ketone at 1.5 draw. Scale bars are 10 μm.

and continues to discolor to dark red when the acetone is fully reacted. During this experiment, the coagulation bath did not discolor. These results demonstrate that ammonium acetate can be used to increase the longevity of the coagulation bath.

Further experiments were carried out comparing acetone coagulation to diethyl

Coagulant	Draw Ratio	Electrical Conductivity (MS/m)	Specific Conductivity (S m^2/kg)
Acetone	1.3	7.9±0.6	5000±100
Acetone	1.5	8.0±0.9	4800±140
DEK	1.3	8.5±0.6	5100±120
DEK	1.5	8.1±0.9	5200±150

Table 5.2 : Electrical conductivity and specific electrical conductivity of fibers spun in acetone and diethyl ketone.

Coagulant	Draw Ratio	Tensile Strength (GPa)	Specific Strength (N/tex)	Young's Modulus (GPa)
Acetone	1.3	2.2±0.4	1.4±0.2	240±30
Acetone	1.5	2.3±0.5	1.4±0.1	240±30
DEK	1.3	2.3±0.3	1.4±0.1	240±30
DEK	1.5	2.1±0.4	1.4±0.1	230±20

Table 5.3 : Tensile strength, specific strength, and Young's modulus of fibers spun in acetone and diethyl ketone.
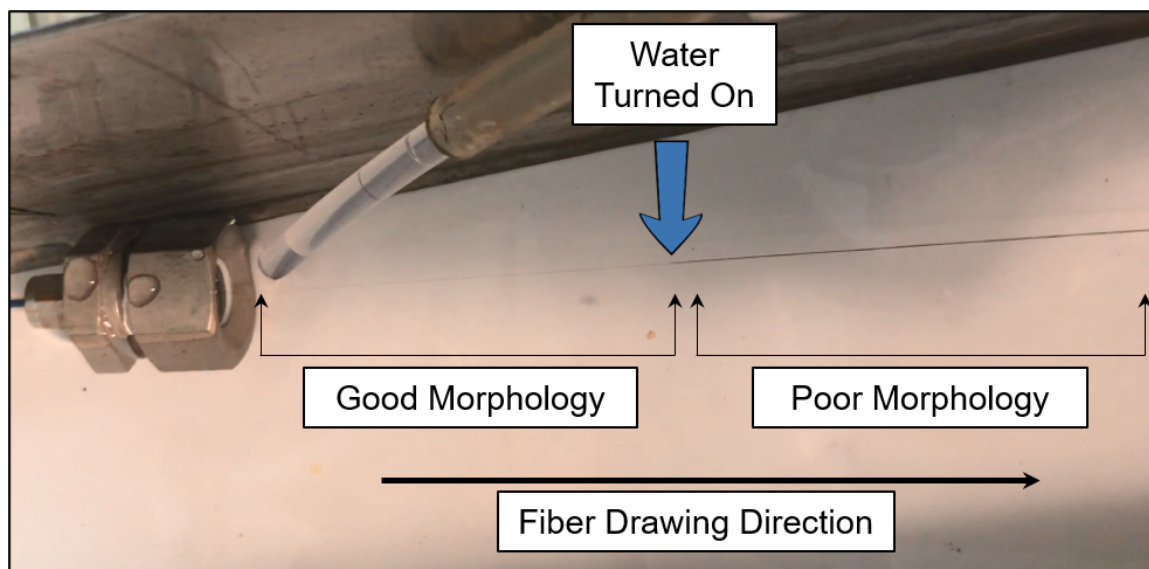
Figure 5.16 : Photograph of spinning with a water jet pointing at the spin-neret/coagulant interface. When the jet is turned on, the fiber is densified resulting in a good fiber morphology.

ketone (DEK) to determine if larger ketones had an effect on coagulation. Fiber was collected using each coagulant at a draw ratio of 1.3 and 1.5. SEM images of the fiber collected in acetone and DEK are shown in Figure 5.15. All fibers were cylindrical in shape with a smooth surface which is indicative of a good coagulation. As shown in Table 5.2 and Table 5.3, there was not a significant difference in the electrical conductivity, tensile strength, or Young's modulus for either coagulant or draw ratio.

As discussed in the introduction to this section, water would be an ideal coagulant due to its low cost, environmental footprint, and toxicity. However, CSA and water react violently to form HCl gas. The HCl gas bubbles out of the water and disrupts the structure of the fiber creating a low density, highly porous structure with poor

Dope Concentration	Electrical Conductivity (MS/m)	Tensile Strength (GPa)	Specific Conductivity (S m^2/kg)	Specific Strength (N/tex)
5 wt%	5.2	0.75	5100	0.76
1 wt%	3.5	0.86	4400	1.16

Table 5.4 : Electrical conductivity, tensile strength, specific conductivity, and specific strength of fibers spun in water with a water jet.

macroscopic properties. Fiber was spun at 5 wt% to slow down coagulation and minimize the quantity of CSA reacting with the water coagulation bath. Although a decrease in bubble formation was observed for higher concentration spinning dope, the fiber performance was still hindered by a porous structure. To further minimize bubbling, a stream of distilled water was pointed at the interface of the spinneret and the coagulation bath as shown in Figure 5.16. With the water at a sufficient flow rate, the HCl is fully soluble in the water so no bubbling occurs. This allows the CNTs to completely densify. This spinning technique was also attempted with a 1 wt% spinning solution. The properties of these fibers are shown in Table 5.4. Although the performance of these fibers are lower than state of the art fibers, these studies are a big step forward towards fiber production in water. Further studies are underway to optimize water as a coagulant. These studies include decreasing the diameter of the spinneret, decreasing the extrusion rate, and designing a co-flow (core and sheath) spinneret.

5.5   Spinneret Diameter and Cone Angle

Results from the previous section on coagulants suggests that the fiber structure forms in the spinneret. Therefore, the design of the spinneret should play an important role in fiber properties and coagulation. In the standard 150 μm spinneret configuration used here, the solution undergoes high shear through a 30° inlet cone followed by stress relaxation from flow through a capillary with a 2:1 aspect ratio (length of capillary/diameter of capillary). By changing the angle of the inlet cone, more shear (larger cone angle) or more relaxation (smaller cone angle) can be induced. A large cone angle will be important if it can produce better alignment of the CNTs within the fiber, whereas a small cone angle would help reduce possible disorder caused by die swell. Hence, the effect of the angle of the inlet cone on the structure and properties of the fiber is studied. Furthermore, we study the effect of increasing spinneret diameter as a means to increase fiber output.

5.5.1   Experimental Details

Meijo 1.5P (Lot 8302305) was dissolved at 0.5 wt% in CSA. Fiber was produced through 3 different spinnerets: 150 μm, 250 μm, and 500 μm. Due to limitations with spinneret manufacturing, each spinneret has an outlet capillary with an aspect ratio (length of capillary/diameter of capillary) of 2 and an overall thickness of 1 mm. Therefore, the spinneret with a diameter of 500 μm is a throughhole, whereas the 150 μm and 250 μm spinnerets have an inlet cone region. The inlet cone for both the 150 and 250 μm spinnerets is 30°. The design of the spinnerets are shown in Figure 5.17. The dope was extruded into acetone at a linear velocity of 2 m/min corresponding to an extrusion rate of 0.036 mL/min, 0.1 mL/min, and 0.4 mL/min
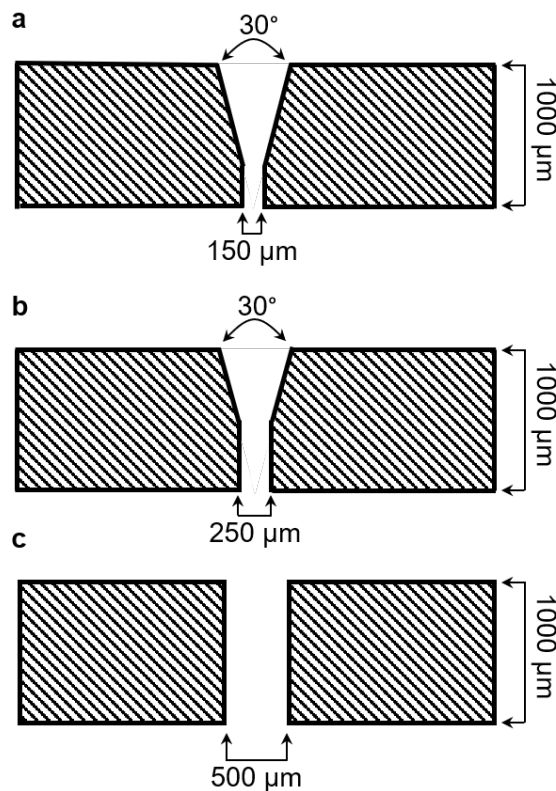
Figure 5.17 : Diagrams of spinnerets with varying outlet diameter. Each spinneret has a capillary with an aspect ratio of 2.

for the 150 μm, 250 μm, and 500 μm spinnerets, respectively. Fiber was collected at a draw ratio of 1.4. The fibers were characterized as described in Section 5.2.2.

Fibers were also produced using spinnerets with varying inlet cones (15°, 30°, and 45°) and outlet diameters of 150 μm and 250 μm. The design of the spinnerets are shown in Figure 5.18. Meijo EC DX301 (Lot 5R79H06C) was purified by heating in a box furnace (Thermolyne, Thermo Scientific) in air at 450 °C for 72 hours. The purified CNTS were dissolved in CSA at 1 wt% and 3 wt% in CSA. Solutions were extruded at 2 m/min corresponding to a volumetric extrusion rate of 0.036 mL/min and 0.1 mL/min for the 150 μm, 250 μm diameter spinnerets, respectively. All fibers
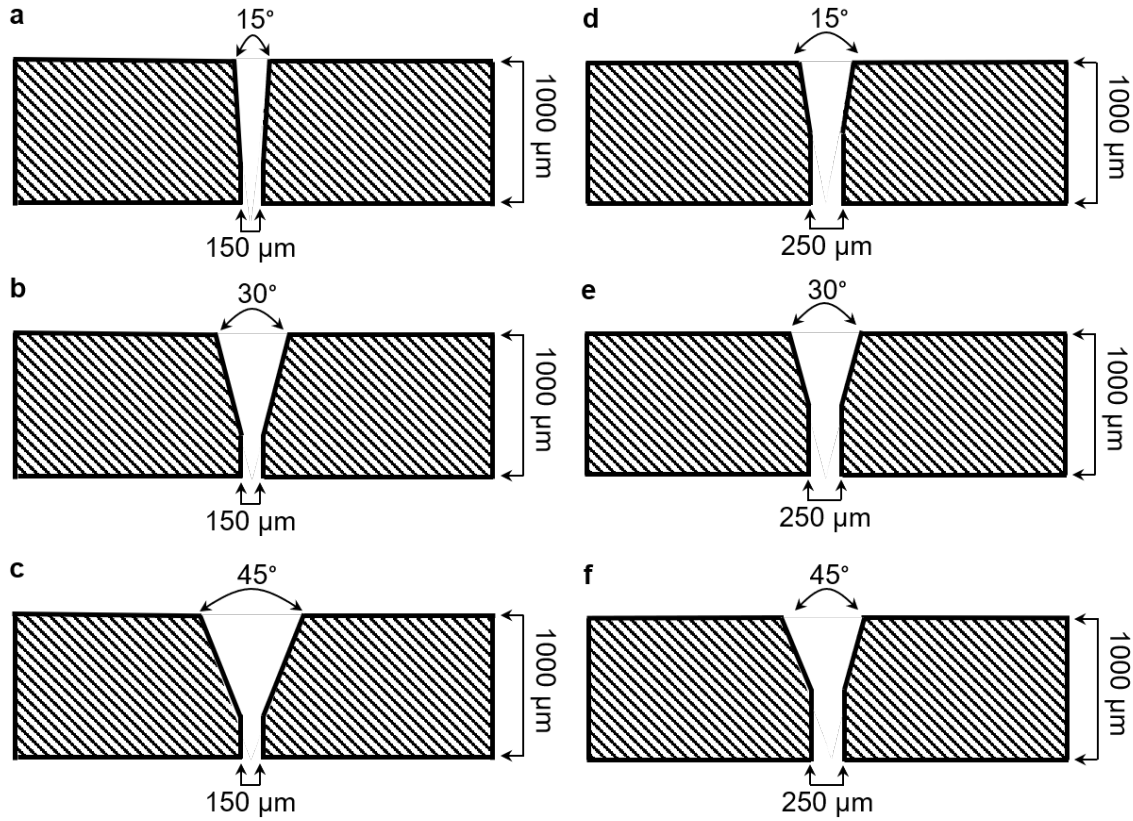
Figure 5.18 : Diagrams for (a,b,c) 150 μm diameter spinnerets with 15°, 30°, and 45° inlet cones and (d,e,f) 250 μm diameter spinnerets with 15°, 30°, and 45° inlet cones.

were collected at 2.7 m/min resulting in a draw ratio of 1.35. The order of use of the spinnerets were randomized to ensure that trends were not a result of order of production. The acetone bath was changed when discoloration occurred. The fibers were also characterized as described in Section 5.2.2.

5.5.2   Results and Discussions

Fibers produced with a 150 μm, 250 μm, and 500 μm diameter spinneret are shown in Figure 5.19. The fiber produced with the smallest spinneret (150 μm) appears to
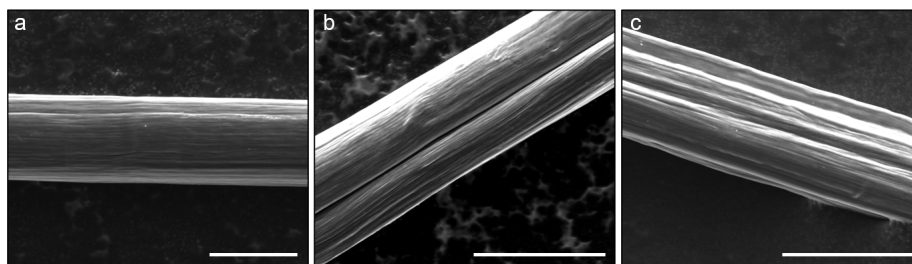
Figure 5.19 : Scanning electron microscopy images of CNT fiber produced at 0.5 wt% with a (a) 150 μm, (b) 250 μm, and (c) 500 μm diameter spinneret.
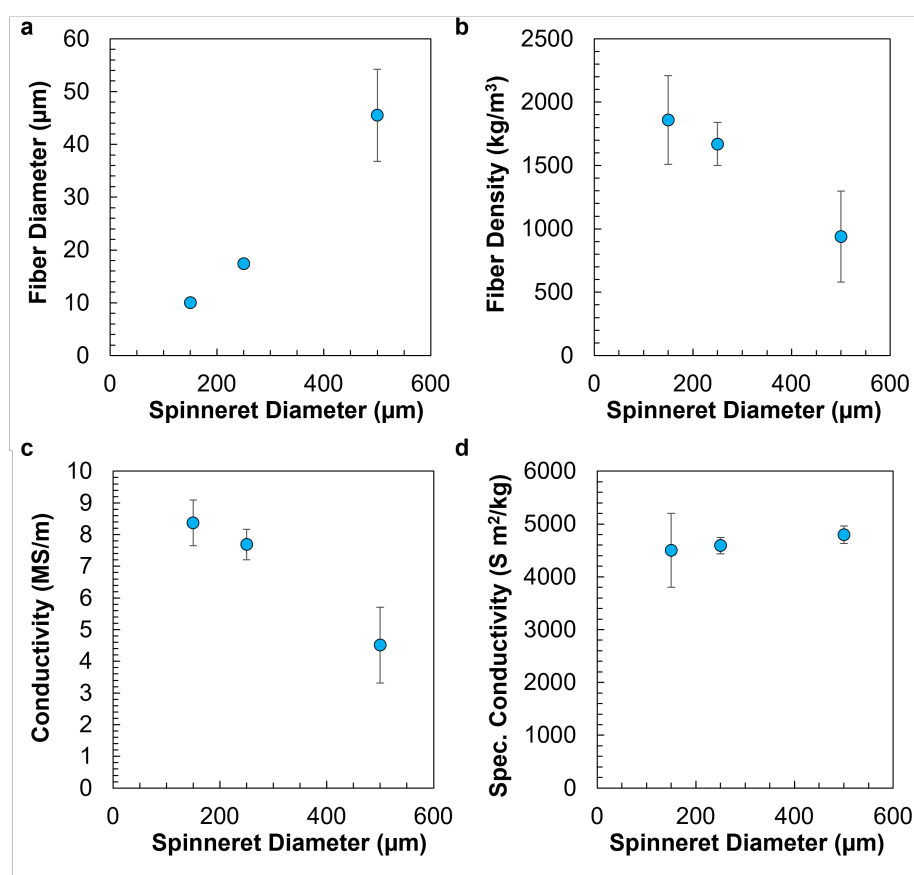
Figure 5.20 : Fiber diameter, density, electrical conductivity, and specific conductivity of CNT fibers spun of 0.5 wt% as a function of spinneret diameter.
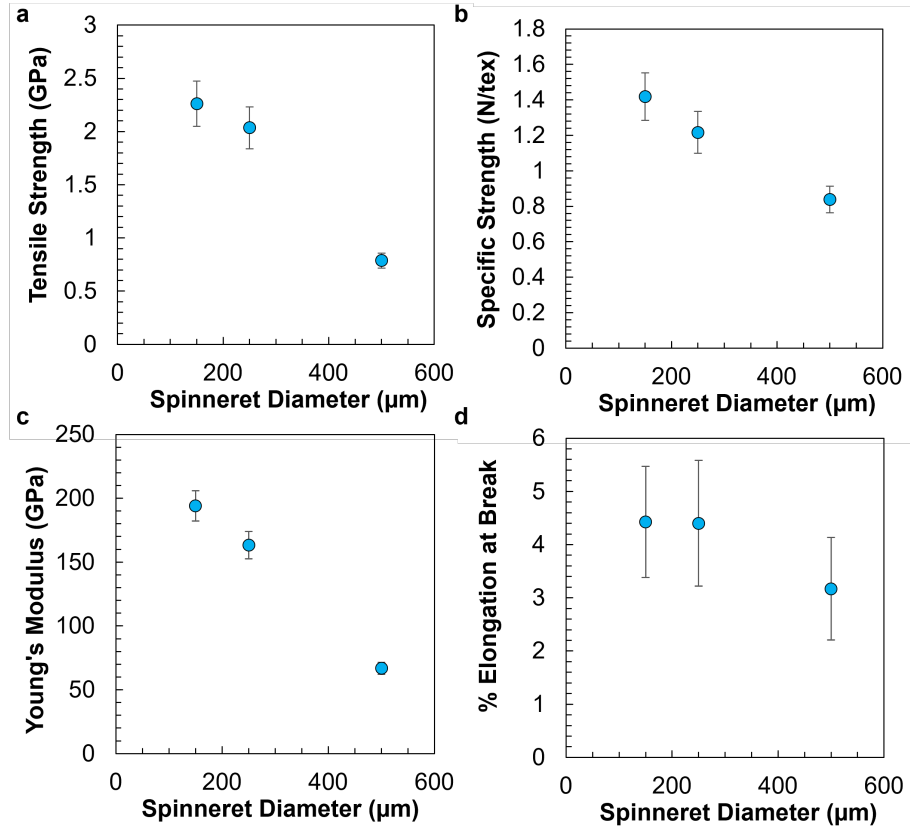
Figure 5.21 : Tensile strength, specific strength, Young's modulus, and elongation at break of CNT fibers spun at 0.5 wt% as a function of spinneret diameter.

have the best surface morphology; the fiber is relatively smooth and cylindrical in shape. The fiber spun with the 250 μm appears to have a slight bean shape which is indicative of the outer shell of the fiber coagulating before the inside of the fiber. The coagulated outside collapses giving rise to the irregular shape. This phenomenon is more pronounced with the fiber spun from the 500 μm; the fiber (Figure 5.19c) has a rough surface and a completely collapsed (ribbon) structure.

As expected, the fiber diameter increases with increasing spinneret diameter (Figure 5.20a). However, due to the poor coagulation of the fiber spun from a 500 μm
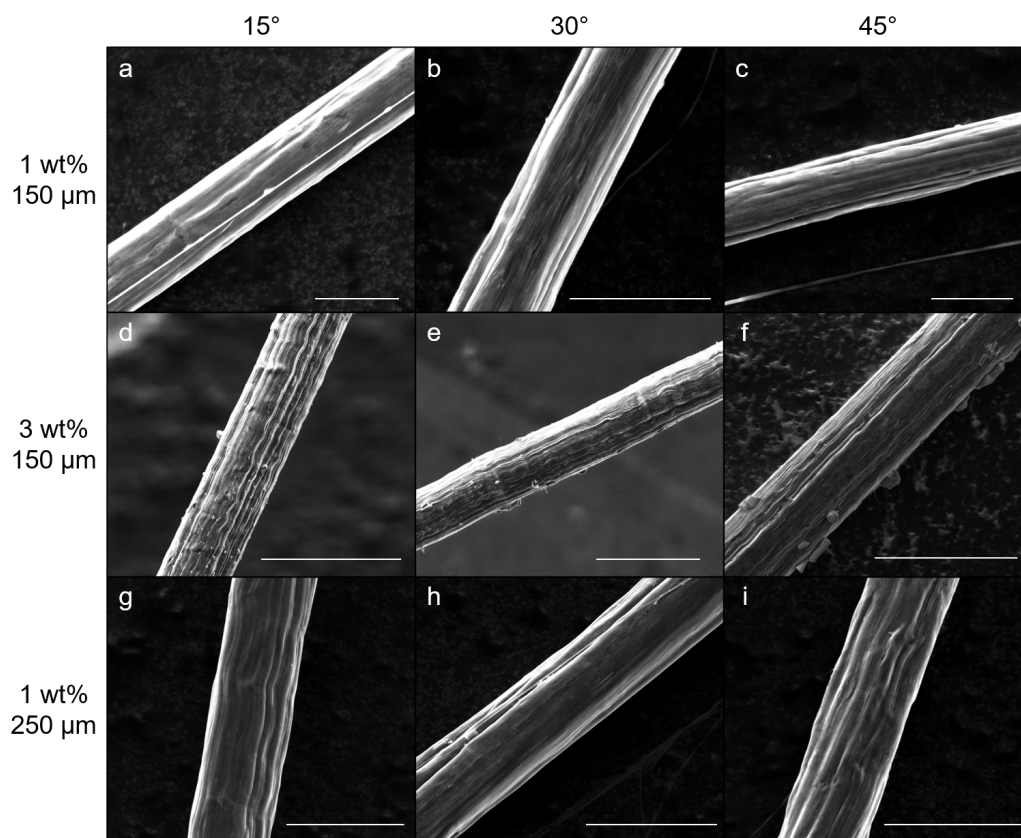
Figure 5.22 : Scanning electron microscopy images of fibers produced from spinnerets with 15°, 30°, and 45° inlet cones. Fiber produced at 1 wt% with a 150 μm spinneret and a (a) 15°, (b) 30°, and (c) 45° inlet cone. Scale bars are 20 μm. Fiber produced at 3 wt% with a 150 μm spinneret and a (d) 15°, (e) 30°, and (f) 45° inlet cone. Scale bars are 50 μm. Fiber produced at 1 wt% with a 250 μm spinneret and a (g) 15°, (h) 30°, and (i) 45° inlet cone. Scale bars are 40 μm.

diameter spinneret, there is a much larger error in the diameter measurement ($\sim$20% compared to $\sim$5% for the fibers produced with a 150 μm and 250 μm diameter spinneret). Furthermore, Figure 5.20b shows the density for each fiber. The fiber spun from a 500 μm has a low density for a solution spun fiber which, again, indicates
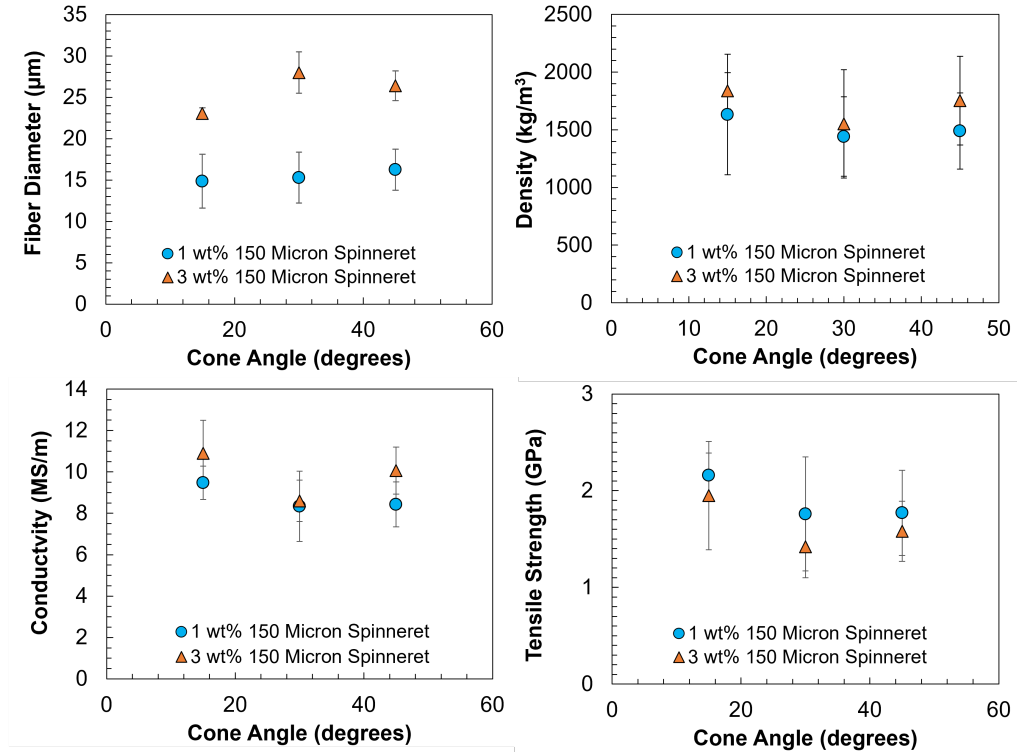
Figure 5.23 : Diameter and density of fiber spun at 1 wt% and 3 wt% from 150 μm diameter spinnerets and 1 wt% through 250 μm diameter spinnerets at varying inlet cone angles.

poor coagulation. The poor coagulation is also evident in low electrical conductivity (Figure 5.20c), tensile strength (Figure 5.21b), specific strength (Figure 5.21a), Young's modulus (Figure 5.21c), and elongation at break (Figure 5.21d). Conversely, the specific conductivity is the same for all fibers. This result suggests that the specific conductivity of the fibers is not sensitive to CNT fiber structure. Instead, the specific conductivity is dependent on the constituent CNTs, as discussed in Section 5.8 and Section 5.7. Fibers produced with a 150 μm spinneret showed the best properties, but the properties were reasonably similar to those of the fibers produced with a 250 μm spinneret.
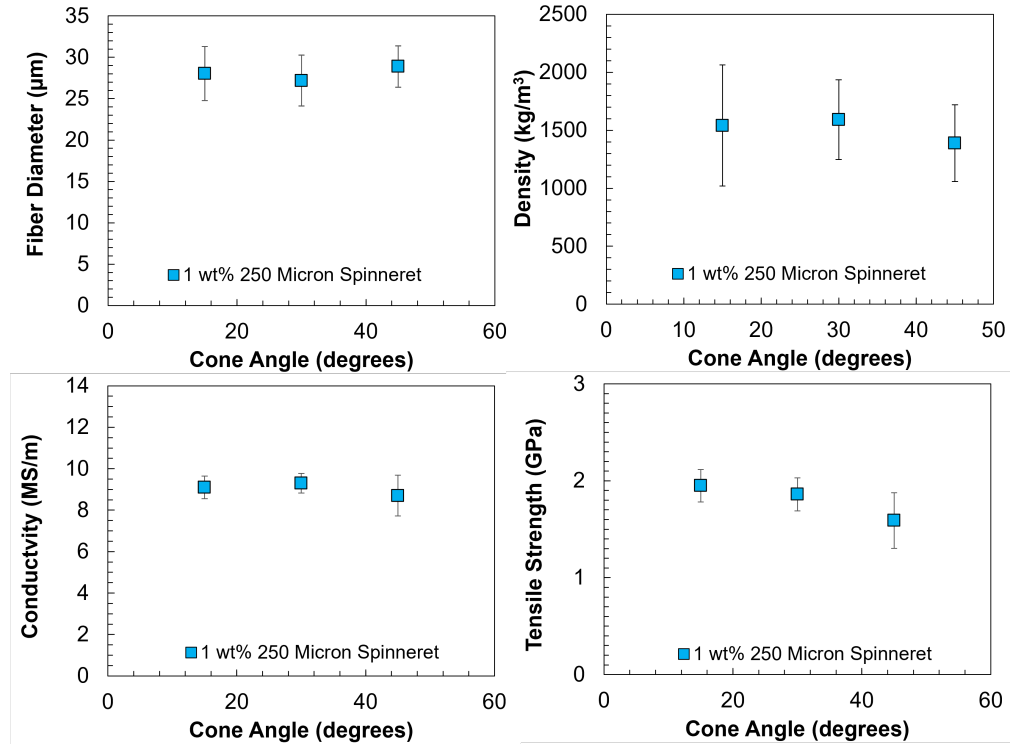
Figure 5.24 : Tensile strength and electrical conductivity of fiber spun at 1 wt% and 3 wt% from 150 μm diameter spinnerets and 1 wt% through 250 μm diameter spinnerets at varying inlet cone angles.

SEM images of fibers produced at 1 wt% from a 150 μm diameter spinneret with an inlet cone of 15°, 30°, and 45° are shown in Figure 5.22a-c, fibers produced at 3 wt% from a 150 μm diameter spinneret with an inlet cone of 15°, 30°, and 45° are shown in Figure 5.22d-f, and fibers produced at 1 wt% from a 250 μm diameter spinneret with an inlet cone of 15°, 30°, and 45° are shown in Figure 5.22g-i. Visually, there is not any significant difference in the fibers as a function of cone angle. All fibers are approximately cylindrical in shape with some surface texture. They show good alignment in the axial direction. Figure 5.23 compares the fiber diameter, density, electrical conductivity, and tensile strength for fibers spun from a 150 μm diameter

spinneret. For both solution concentrations, the 15° inlet cone produced fibers with a slightly lower average diameter with a higher density. Furthermore, the 15° inlet cone showed an ~20% improvement in electrical conductivity and tensile strength over the other spinnerets.

The results from fibers produced at 1 wt% with a 250 μm spinneret are shown in Figure 5.24. The fibers had similar diameters for all cone angles. However, the fiber produced with the 45° spinneret had a lower density than the other two inlet cones. Moreover, the fibers produced with a 15° and 30° inlet cone had similar electrical and tensile properties, whereas the fiber produced with a 45° inlet cone had an ~15% decrease in tensile strength.

These initial results suggest that, similar to other complex polymer systems, the liquid filament undergoes some degree of die swell caused by stress stored in the fluid. By increasing the length of the capillary region of the spinneret, a greater portion of this stress can be dissipated by viscous forces. This could be increasingly important when looking for efficiency improvements in the process as die swell increases with increasing concentration. Further studies will use spinnerets with smaller inlet cone angles as well as inlet cones that are 500 μm longer to obtain a better understanding of optimal spinneret design.

5.6 Carbon Nanotube Fiber Solution Processed with TiO$_2$ Nanoparticles

The unique combination of flexibility, conductivity, and mechanical strength make CNT fibers of significant interest for composites with additional functionality such as charge storage, sensing or catalysis [86–89]. In particular, there is interest in combin-

ing TiO$_2$ with CNT fibers to create high efficiency photocatalyst composites for water purification [89]. This is because TiO$_2$ is a low cost and safe photocatalyst, but it has low efficiency due to the quick recombination of the electron and hole pairs and limited surface area [90]. Due to the high electrical conductivity of CNTs, electrons can travel freely through CNT structure which suppresses electron-hole recombination, thus enhancing the photocatlytic ability of the TiO$_2$. Furthermore, CNTs can act as a support structure for TiO$_2$ nanoparticles which further improves the efficiency.

Previous work indicated that high levels ($>6\%$) of iron nanoparticles (residual catalyst), impeded processing of fibers [68]. Spin dopes with ~ 15 wt% catalyst particles did not form a viscoelastic solution, and a draw ratio above 1 could not be obtained. Due to poor processability, the fiber properties were severely hindered. Here, the feasibility of CNT/TiO$_2$ composite fibers was studied by spinning mixtures of CNT and TiO$_2$ in CSA.

5.6.1 Experimental Details

A spin dope was prepared by adding 1 wt% Meijo 1.5P (Lot 8302305) and 1 wt% titanium dioxide nanopowder (US Research Nanomaterials, Inc., 80% anatase 20% rutile, $>99\%$, 20nm) to CSA. Fiber spinning was carried out as described in Section 5.2.1. Dope was extruded at 0.036 mL/min and collected at a draw ratio of 1.35, 1.5, and 1.6. Fibers were washed in room temperature water, heated in an oven at 115 °C overnight, and then washed in warm water (60 °C) for 3 hours. Fiber was characterized as described in Section 5.2.2. Fiber was also cut using an argon source focused ion beam (FEI, Helios NanoLab 660 DualBeam) to view the internal structure.

5.6.2 Results and Discussions
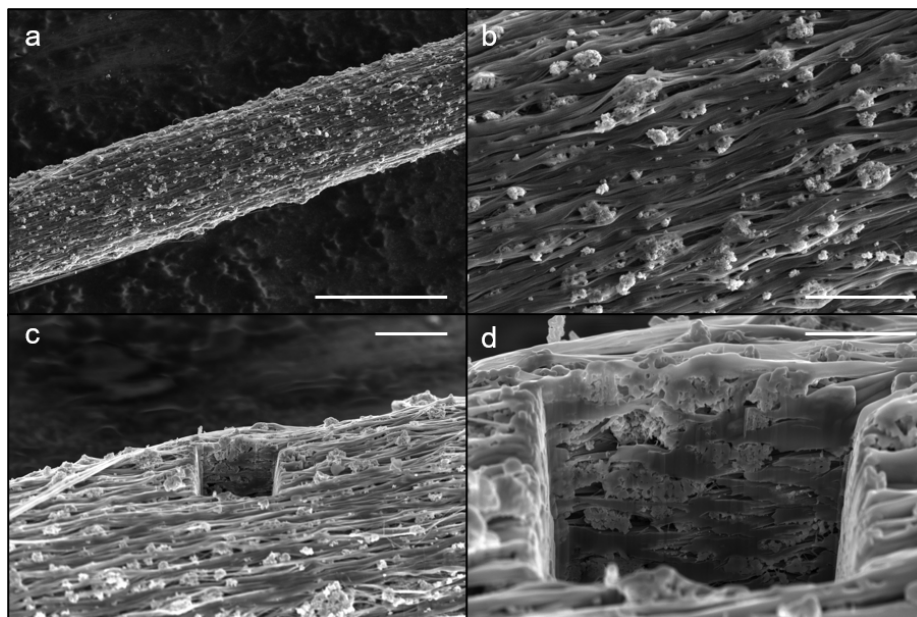
Figure 5.25 : Scanning electron microscopy images of CNT fiber with intercalated TiO$_2$. Scale bars are (a) 30 μm, (b,c) 5 μm, and (d) 2 μm.

Fiber was produced with a 1:1 weight ratio of CNTs and TiO$_2$ nanoparticles at three draw ratios - 1.35, 1.5 and a maximum draw of 1.6. Fiber was produced continuously without any processing difficulties such as spinneret clogging or filament breakup; collection was manually stopped at 30 minutes for each draw ratio resulting in fibers that were $\sim$100 m long. Visually, the surface of the TiO$_2$/CNT fibers were matte gray rather than the shiny black appearance of neat CNT fibers. Figure 5.25a and b show SEM images of fiber produced at 1.5 draw. As with neat CNT fiber, the fiber is cylindrical in shape, and there is good alignment of the CNT bundles along the length of the fiber. In between the CNT bundles, there are aggregates of TiO$_2$ nanoparticles. These aggregates are evenly distributed along the fiber. Figure

Draw Ratio	Diameter (μm),	Electrical Conductivity (MS/m)	Tensile Strength (GPa)
1.35	23.0±2.0	2.2±0.6	0.69±0.13
1.5	22.8±1.5	2.1±1.0	0.65±0.09
1.6	21.4±0.8	2.2±0.8	0.66±0.08

Table 5.5 : Diameter, electrical conductivity, and tensile strength of CNT/TiO$_2$ composite fibers. Properties were consistent for all draw ratios.

Type of Fiber	Diameter (μm),	Electrical Conductivity (MS/m)	Tensile Strength (GPa)
Neat CNT	16.4±1.9	6.8±0.9	1.5±0.4
CNT/TiO$_2$	22.8±1.5	2.1±1.0	0.65±0.09

Table 5.6 : Diameter, electrical conductivity, and tensile strength of neat CNT fibers and CNT/TiO$_2$ composite fibers.

Type of Fiber	Resistance (Ω/m)	Break Force (gf)
Neat CNT	700±20	32.4±1.6
CNT/TiO$_2$	1170±50	27.1±1.2

Table 5.7 : Resistance and break force of neat CNT fibers and CNT/TiO$_2$ composite fibers.

5.25c and d show a fiber with a section milled with a focused ion beam (FIB) to view the internal structure of the fiber. These images show that the TiO_2 nanoparticles are intercalated throughout the fiber and the structure seems fairly homogeneous. Additionally, there are visible void spaces within the fiber that are not present in neat fibers.

Table 5.5 shows the engineering properties of the fibers produced at each draw ratio. As expected, the fiber diameter decreases with increasing draw ratio. However, the electrical conductivity and tensile strength do not vary with draw ratio. To put these results in context, the fiber properties are compared to the properties of fiber produced at 1 wt% with the same batch of CNTs from Meijo Nanocarbons at the same draw ratio (1.5) without TiO_2 (Table 5.6 and 5.7). There is an $\sim$40% increases in the diameter due to the presence of TiO_2 nanoparticles and additional void spaces. Furthermore, the electrical conductivity and tensile strength decreased by 69% and 57%, respectively. However, these large decreases in properties are expected due to the fact that TiO_2 is not conductive and is not load bearing. In fact, high performance fibers such as carbon fiber tend to be limited in strength due to the presence of inclusions and voids within the fiber [91]. So we would expect to see an immense decrease in fiber strength. Here, we only see a 16% decrease in absolute breaking force between the composite and neat fiber. On the other hand, we see a 67% decrease in resistance. This suggests that packing density and purity have a bigger impact on fiber conductivity than tensile strength. Additionally, although the composite fibers do have significantly decreased engineering properties, they still out perform materials such as A36 structural steel in electrical conductivity and tensile strength (1.5 MS/m and 0.55 GPa). Finally, and perhaps most importantly, these results show that CNTs are still solution processable even with 50 wt% impurities. These results demonstrate

that the processability of CNTs with large quantities of nanoscale catalyst is not hindered by the presence of catalyst itself. Instead, unlike TiO_2, the iron catalyst reacts with the CSA [92] which decreases the acid strength which, in turn, decreases the level of protonation of the CNTs.

5.7   Carbon Nanotube Aspect Ratio and Purity

Previous theoretical [51] and experimental [12] research has demonstrated that increasing the aspect ratio (L/D) of constituent CNTs improves macroscopic fiber properties. However, these experimental studies utilized CNTs from different manufacturers (HiPCO, Meijo Nanocarbons, OCSiAl, Samsung, UniDym, CCNI, and SweNT), so the effect of additional CNT characteristics such as CNT purity are not accounted for and can vary significantly from sample to sample. Furthermore, as discussed in Chapter 3, the method of purification can affect the aspect ratio; as the CNTs are more thoroughly oxidized, the CNTs have a lower aspect ratio. Here, we thermally and mechanically shortened CNTs so that we can control for variances in CNT samples from different manufacturers. By thermally oxidizing the CNTs, the reactive ends of the CNTs will oxidize and shorten the CNTs. However, this technique also removes additional reactive carbon species in the sample. On the other hand, mechanical shearing will shorten the CNTs, but the impurities present in the samples will remain constant.

5.7.1   Experimental Details

CNTs were purchased from Meijo Nanocarbons (Meijo 1.5P, Lot 9300505) and purified before use by oxidizing for 1 hour at 400 °C in a box furnace (Thermolyne, Thermo Scientific). The viscosity averaged aspect ratio of the CNTs was measured

using a capillary breakup extensional rheology method as described previously [12].

The material was then shortened using two different techniques: oxidation in a box
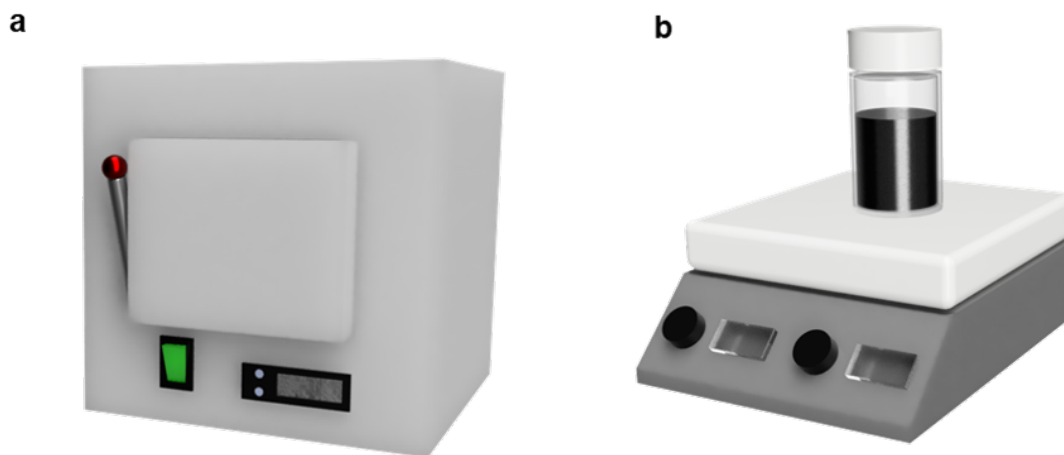
Figure 5.26 : CNTs were shortened by (a) thermal oxidation in a box furnace or (b) mechanical shearing with a rare earth stir bar.

furnace and high shear mechanical mixing (Figure 5.26). For the box furnace technique, the material was oxidized in the box furnace at a temperature of 550 °C and 725 °C resulting in an aspect ratio of 3310 and 2730, respectively. For mechanical shortening, the CNTs were dissolved in CSA at 1 wt% in a vial, speed mixed for 2 hours, and sheared with a rare earth stir bar at 2500 rpm on a stir plate (Fisher Scientific). Small quantities of the solution were removed from the vial periodically and diluted to ~100–170 ppmw to perform aspect ratio measurement. Based on these measurements, the solutions were sheared for 8 hours and 32 hours resulting in an aspect ratio of 2930 and 2160, respectively. For comparison Meijo EC DX301 (Lot 5R79H06C) was thermally oxidized to obtain aspect ratios of ~4300 and ~3500. The solutions were then spun into fibers as described in Section 5.2.1 with an extrusion

rate of 0.036 mL/min and a draw ratio of 1.35. Finally, the fibers were characterized as described in Section 5.2.2.

5.7.2   Results and Discussions
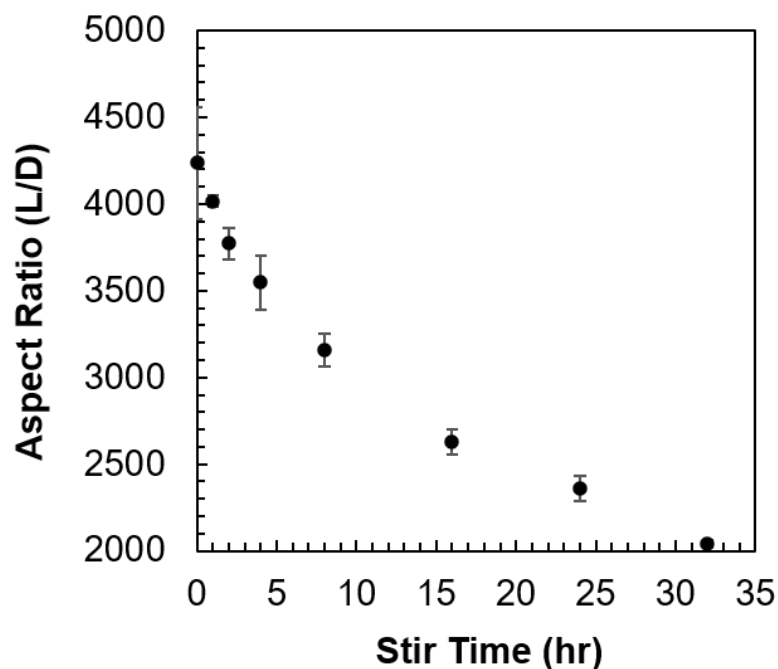
Figure 5.27 : Viscosity averaged aspect ratio of a 1wt% solution of CNTs in CSA over time while stirred with a rare earth stir bar. Data courtesy of R. J. Headrick.

Solutions of 1 wt% CNTs in CSA were subjected to high shear mixing, and the aspect ratio was measured after 1, 2, 4, 8, 16, 24, and 32 hours of mixing (Figure 5.27). This data shows a significant decrease in aspect ratio over time with mechanical mixing. Although these results show a promising method to shorten CNTs without altering CNT diameter distribution or purity content, it can also be problematic if using a stir bar to aid in the dissolution of CNTs. Based on these results, two 1 wt%
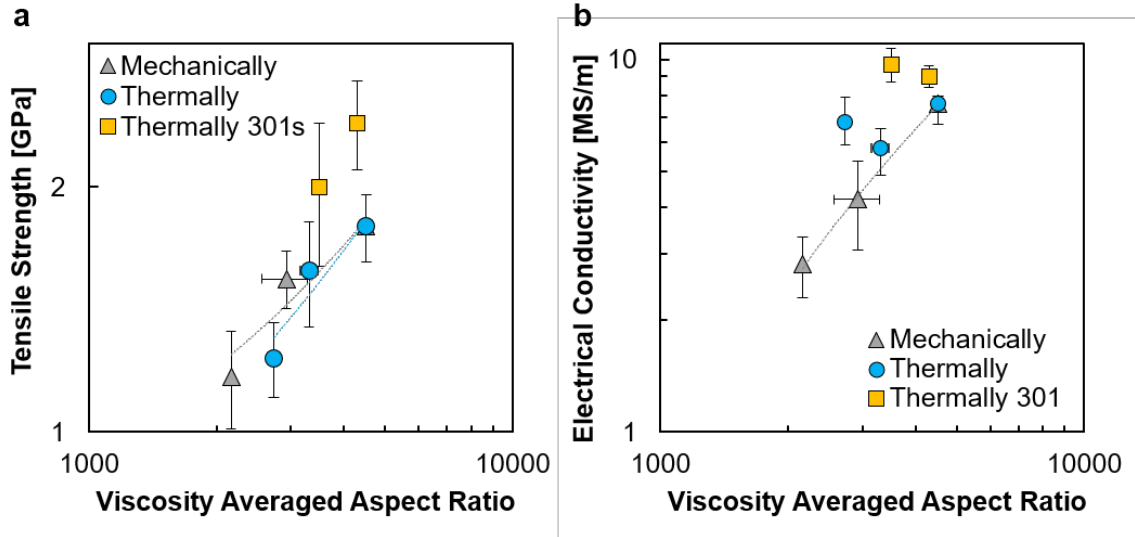
Figure 5.28 : (a) The tensile strength and (b) electrical conductivity for fibers produced with CNTs that were shortened mechanically and thermally.

solutions were speed–mixed for 8 hours and 32 hour to obtain CNTs with an average aspect ratio of ∼3000 and ∼2000, respectively.

The properties of the fibers spun with the maximum aspect ratio CNTs (L/D ∼4500), thermally oxidized CNTs (L/D ∼3300 and ∼2700 and L/D ∼4300 and ∼3500 for Meijo 301), and mechanically shortened CNTs (L/D∼2900 and ∼2200) are shown in Figure 5.28. In agreement with previous results discussed in Section 5.7, the tensile strength trends upward with increasing aspect ratio for both shortening methods (Figure 5.28a). There is a very strong agreement in the trend of tensile strength with aspect ratio for with CNTs spun with both shortening methods from Meijo Lot 9300505, whereas fibers spun with Meijo 301 Lot 5R79H06C have a higher tensile strength for similar aspect ratios. With electrical conductivity, we see a very different trend between the two shortening methods. The fibers spun from mechanically shortened CNTs show an improvement in electrical conductivity with increasing aspect

ratio. Conversely, both sets of thermally shortened CNTs do not show an improvement in electrical conductivity with increased aspect ratio. This suggests that the purity of the CNTs has an important impact on the macroscale electrical conductivity of the fibers. Furthermore, similar to the tensile strength data, we see a discrepancy in properties between the two lots of CNTs with the Meijo 301 having a higher electrical conductivity. These results suggest that another CNT characteristic beyond aspect ratio such as diameter distribution, polydispersity, or number of walls could play an important role to further improve CNT fiber properties.

5.8   Concentration of Carbon Nanotubes in the Spin Dope

As the properties of CNT fibers continue to improve, there is increasing interest in expanding the scale of production. To make the adoption of CNT fiber into applications such as fiber reinforcements and coaxial cable feasible, the process must be energy efficient and cost effective. An important parameter to improve efficiency is to increase the concentration of CNTs in the spin dope as other high performance fibers such as Kevlar only become economically viable when spun at 20 wt% [93]. Previous studies in the Pasquali lab found that the optimal spin dope concentration was ~2.0-3.0 wt% CNTs [11, 36]. Since these studies were performed, there were significant changes in CNT properties used for fiber spinning and changes in the spinning process itself. The original studies used material produced by Continental Carbon Nanotechnologies Inc. These CNTs had an average diameter of 3.2 nm and an average length of 4.3 μm resulting in an average aspect ratio of ~1300. Furthermore, this material had an average of 2.6 walls. Conversely, current fiber spinning studies use CNTs produced by Meijo Nanocarbons. Although there is batch to batch variability, typical CNTs have an average diameter of 1.7–2.0 nm, an aspect ratio of

3500–4500, and an average of 1.5–2 walls. This large increase in aspect ratio increases the viscosity of the spin dope and the phase behavior [94]. Furthermore, the previous studies were performed with small diameter (65 μm) spinnerets, which limited the production of fibers from low concentration spin dopes (1.5 wt%) because the fibers were small in diameter and difficult to measure [36]. Finally, the spin line was altered to directly extrude the spin dope rather than use an oil driven piston. Therefore, we studied fiber properties as a function of CNT concentration and explored the underlying mechanism for property improvement.

5.8.1 Experimental Details

5.8.1.1 Fiber Spinning

CNTs were purchased from Meijo Nanocarbons (Meijo 1.5P Lot 7110205) and used as received. The CNTs were dissolved into CSA at 0.5 wt%, 1 wt%, 1.5 wt%, 2.0 wt% and 3.0 wt% and mixed with a speed mixer (Flaktech). Fibers were produced as described in Section 5.2.1. Fiber was also produced at 3.0 wt% using a 100 μm spinneret with a 30° inlet cone angle to study coagulation affects. For each concentration, the draw ratio and extrusion rate were optimized to obtain fibers with the best tensile strength and electrical conductivity. Additional CNT fibers were produced using Meijo 301 (Lot 5R79H06C) at 1 wt%, 3 wt%, 5 wt% and 10 wt% to validate results and produce fiber for characterization with ultra small neutron scattering (USANS). Finally, Meijo 1.5 P (Lot 8302305, L/D ~3600), Tuball (OC-SiAL, experimental batch provided to Rice University, L/D ~1100), and Meijo 101 (L/D ~6700) were spun at 0.5 wt% to study fiber properties as a function of aspect ratio when spun at low concentration. It should be noted that spinning substantially below 0.5 wt% is limited due to the fact that coagulated fibers become so small that

they are not visible by eye.

5.8.1.2 Additional Fiber Characterization Methods

Fibers were characterized as described in Section 5.2.2. Nano-computed tomography (Xradia UltraXRM-L2000) was performed in Zernike phase contrast mode to increase the phase contrast. Wide-angle X-ray scattering was performed on a single CNT fiber with a wide–angle diffractometer (Molecular Metrology SAXS system). Polarized Raman spectroscopy (Renishaw InVia Confocal Raman microscope 532 nm excitation) was performed to determine surface alignment of CNT fibers. The G peak intensity (I) was measured by three different scattering geometries, and the orientational order parameter, $S_{R\Delta}$ was calculated by the following relation corrected for anisotropic absorbance of incident and scattered light where Δ is the dichroic ratio:

$$S_R\Delta = \frac{6\Delta I_{vv} + 3(1+\Delta)I_{VH} - 8I_{HH}}{6\Delta I_{vv} + 12(1+\Delta)I_{VH} + 16I_{HH}}. \tag{5.1}$$
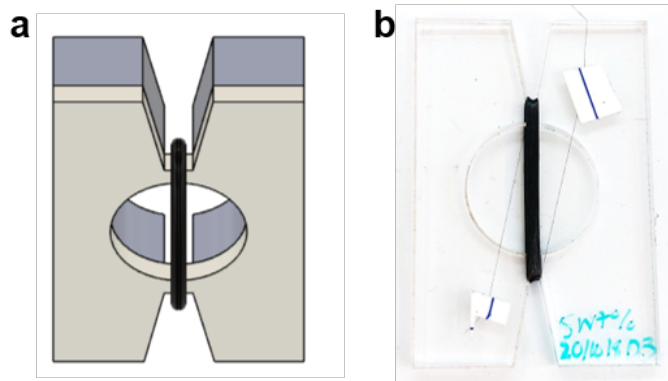
Figure 5.29 : (a) Schematic of a sample holder. The fiber was wrapped around a 1/8 inch acrylic holder. The holder was mounted to 3/8 inch blocks for support. (b) Photograph of 5 wt% fiber wrapped around the sample holder.

USANS sample holders were laser cut from 1/8 inch acrylic (McMaster Carr). Fiber produced at 1 wt%, 3 wt%, 5 wt% and 10 wt% ($\sim$100 m) was wrapped tightly around the holder to form thick bundles. Finally, these holders were mounted on 3/8 inch blocks of acrylic so that they are self-supported in the beam line. A schematic and photograph of the samples are shown in Figure 5.29.

5.8.2 Results and Discussions
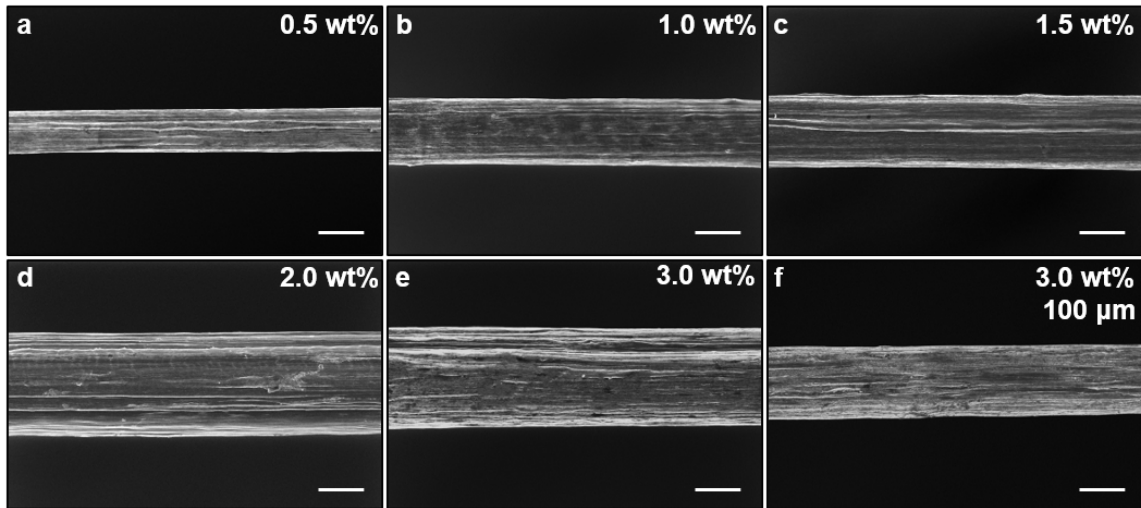
Figure 5.30 : Scanning electron microscopy images of fibers produced with a CNT concentration of (a) 0.5 wt%, (b) 1.0 wt%, (c) 1.5 wt%, (d) 2.0 wt%, and (e) 3.0 wt% from a 150 μm spinneret and (f) 3.0 wt% from a 100 μm spinneret. Scale bars are 10 μm.

Figure 5.30 shows SEM images of fiber produced with varying CNT concentration in the spin dope. All fibers have good alignment in the axial direction and are fairly cylindrical in shape. All images are taken at the same magnification (2,500x) so that visual size comparisons can be made. As expected, the fibers increase in diameter
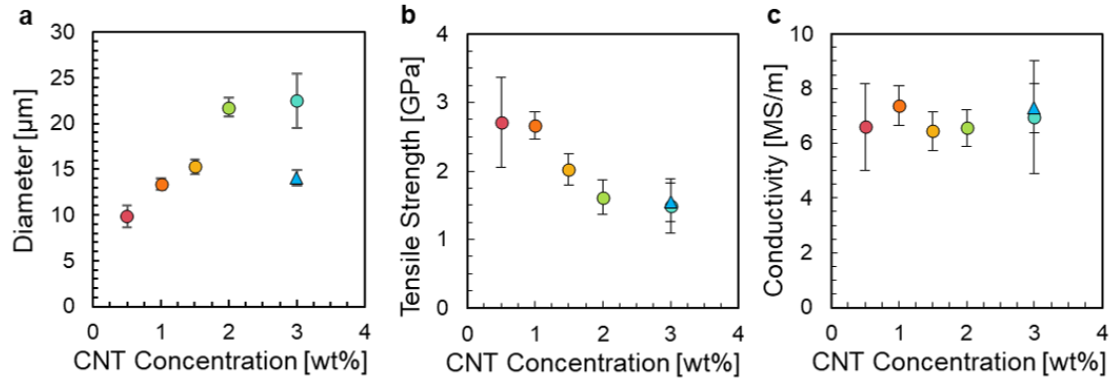
Figure 5.31 : (a) Fiber diameter, (b) tensile strength, and (c) electrical conductivity as a function of CNT concentration in the spin dope. The blue triangle represents 3 wt% spun with a 100 μm spinneret.
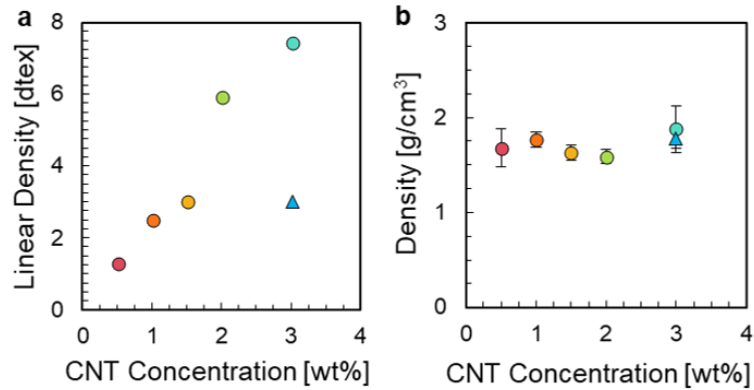
Figure 5.32 : (a) Linear density and (b) density of fibers produced with varying CNT concentration in the spin dope. The linear density of the fibers increases with CNT concentration (with the exception of the blue triangle which represents 3 wt% spun with a 100 μm spinneret). The density is constant with CNT concentration.

with increasing CNT concentration because the throughput of solution is the same for Figures 5.30a–e and the draw ratios are similar. Figure 5.30f shows fiber produced
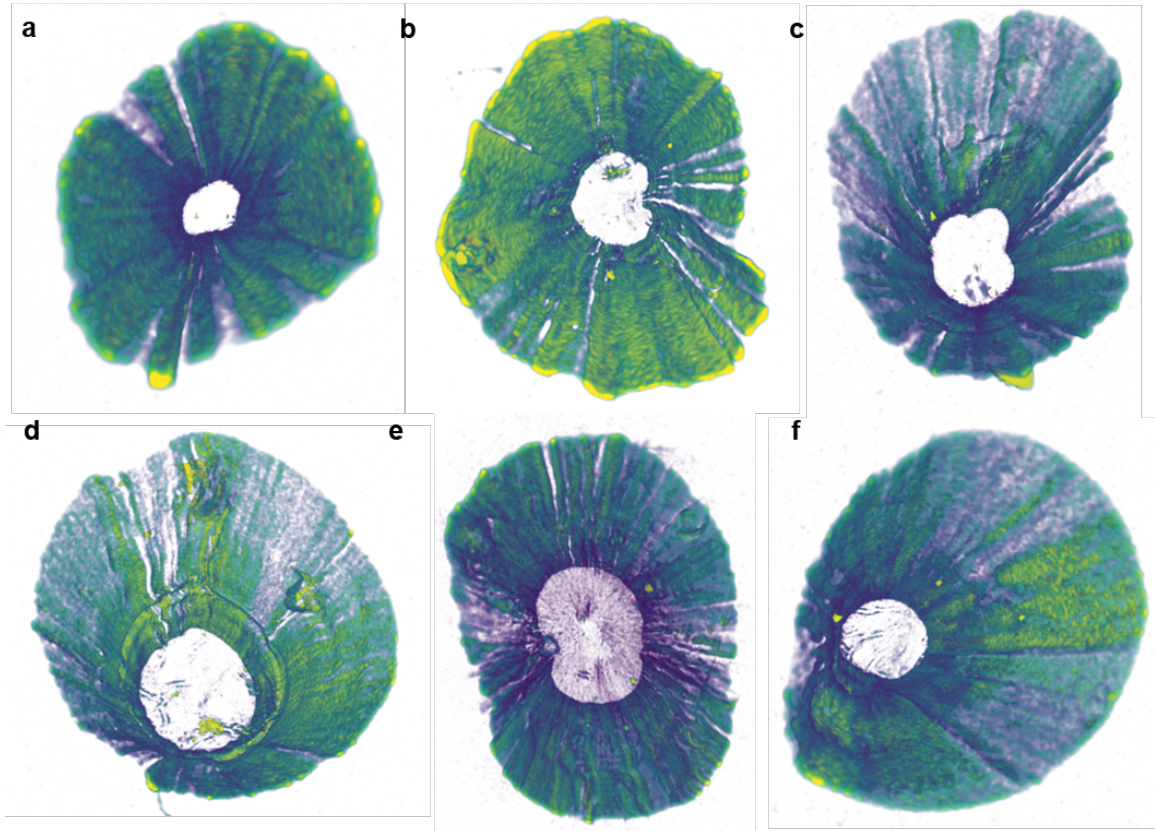
Figure 5.33 : Nano–computed tomography images of fibers produced at (a) 0.5 wt%, (b) 1.0 wt%, (c) 1.5 wt%, (d) 2.0 wt%, and (e) 3.0 wt% from a 150 μm spinneret and (f) 3.0 wt% from a 100 μm spinneret.

with a 3.0 wt% solution with a 100 μm spinneret. The throughput through this spinneret was decreased to study the same linear extrusion rates (0.5 m/min – 2.0 m/min). The trend of fiber diameter is shown in Figure 5.31a. This figure also shows that the average diameter of the fiber produced at 1 wt% with a 150 μm spinneret is similar to the diameter of the fiber produced at 3 wt% with a 100 μm spinneret. Figure 5.31b shows that there is a very strong increasing trend in tensile strength with decreasing CNT concentration. On the other hand, Figure 5.31c shows that electrical

conductivity is not affected by CNT concentration as it is relatively constant across all concentrations tested. Furthermore, the 3 wt% fiber produced with a 150 μm and 100 μm spinneret have nearly identical properties. This indicates two things: First, the decrease in tensile strength with CNT concentration in the spin dope is not a result of increasing fiber diameter. This is an interesting observation as carbon fiber tends to increase in tensile strength with decreasing diameter due to a decrease in defects per unit volume [95]. Secondly, this result suggests that the decrease in strength is not a result of diffusion limitations during coagulation. By decreasing the diameter of the spinneret from 150 μm to 100 μm, the surface area to volume ratio increased by 50% which would improve the diffusion of the acid out of the fiber and the coagulant into the fiber.

To understand the underlying mechanism for tensile strength improvement, additional properties of the CNT fibers were studied. Figure 5.32 shows the linear density and density of the fibers. As with diameter, the linear density of the fibers increases with increasing CNT concentration. This is, of course, with the exception of the 3 wt% fiber spun with the 100 μm spinneret. The linear density of this fiber is similar to the fiber produced at 1.5 wt%. The density is relatively constant with CNT concentration indicating that all of the fibers have similar packing density. This result was explored further with nano–computed tomography. The images in Figure 5.33 show density differences down the length of several microns of fiber. The results from this study indicate that there is not a well-defined trend of packing density on fiber strength; although the 0.5 wt% fiber (Figure 5.33a) has few indications of density differences (i.e. inclusions or void spaces in the fiber) down the axis of the fiber and the 3.0 wt% fiber (Figure 5.33e) has many small density differences, the 3.0 wt% spun with a 100 μm spinneret (Figure 5.33f) has significantly fewer density differences than

the 3.0 wt% fiber spun with a 150 μm spinneret despite having identical properties. Furthermore, the 1.0 wt% (Figure 5.33b) fiber has many density differences and is almost as strong as the 0.5 wt% fiber. These results indicate that there is not a discernible difference in packing density between the fibers.
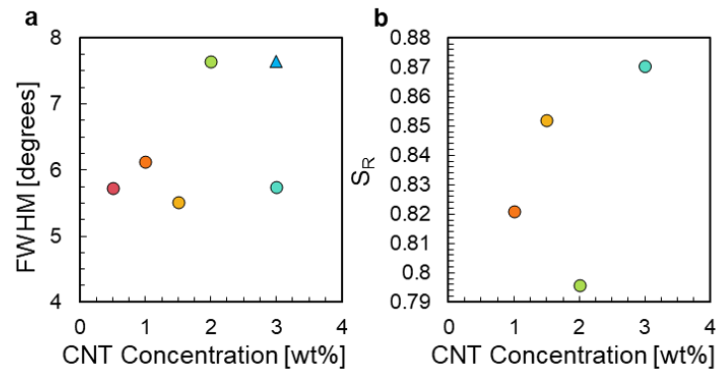
Figure 5.34 : Alignment from (a) wide angle X–ray scattering and (b) polarized raman spectroscopy of fibers produced with varying CNT concentration in the spin dope.

The alignment of the fibers were also compared (Figure 5.34). Wide angle x-ray scattering was used to determine the full width of half maximum (FWHM) for each fiber produced. The FWHM is a measure of the anisotropy of the material; the smaller the FWHM, the higher the anisotropy or alignment of the material. Here, there is no correlation between the FWHM and the CNT concentration. This result is confirmed with polarized Raman spectroscopy; there is no correlation between the orientational order parameter (S_R) (described in Section 5.8.1.2) and CNT concentration. Thus, the increase in tensile strength with decreasing CNT concentration does not depend on the alignment of the fibers. We can also note that the alignment of solution spun CNT fiber has improved over time from 32° in 2004 and 9.4° in 2013 to $\sim$ 6° in this thesis [7, 11].
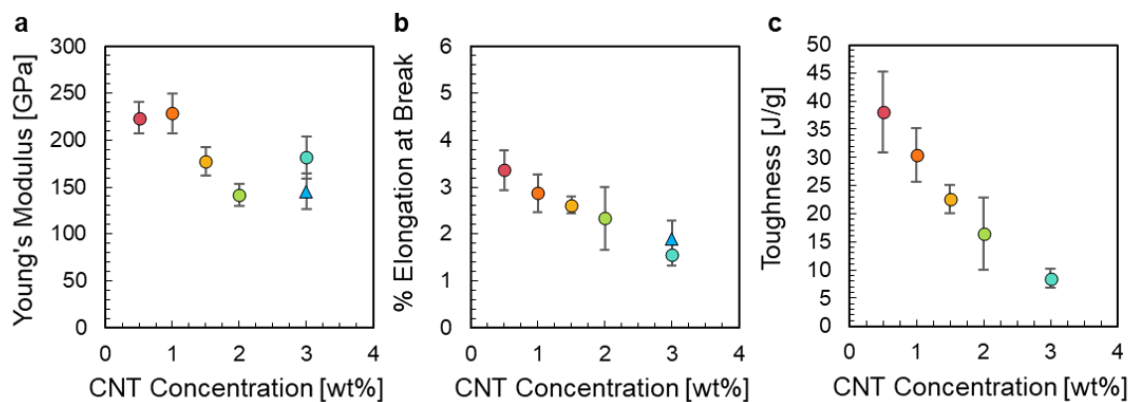
Figure 5.35 : (a) Young's modulus, (b) elongation at break, and (c) toughness of fibers produced with varying CNT concentration in the spin dope.
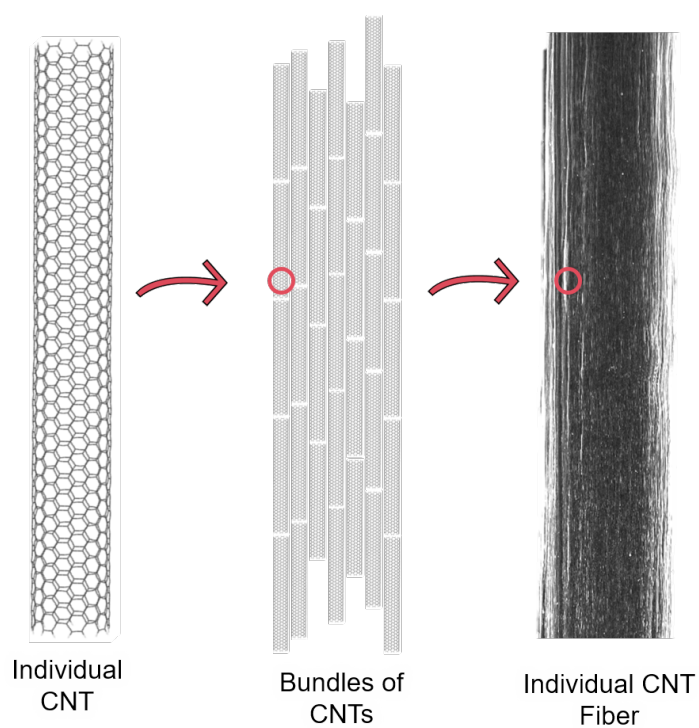
Figure 5.36 : Schematic of the Hierarchical Structure of CNT Fibers.

Additional mechanical properties of the CNT fibers were also compared. Figure 5.35a shows the Young's modulus with increasing CNT concentration. In general, there is an improvement in Young's modulus with decreasing CNT concentration. However, this trend is not as well-established as the trend with tensile strength. This could be attributed to the fact that Young's modulus is sensitive to alignment in fibers - better alignment results in a higher Young's modulus. More interestingly, there is a strong trend with elongation at break (Figure 5.35b). The elongation at break increases with decreasing CNT concentration. These results suggest that the increase in tensile strength could be attributed to the arrangement of the CNTs within the fiber. Figure 5.36 shows a schematic of the hierarchical structure of CNT fibers. CNTs aggregate together to form densely–packed bundles. These bundles then assemble to form the fiber. In the lower concentration solutions, the CNTs have a smaller excluded volume and are able to move more freely. The CNTs may be able to assemble into bundles with a longer effective aspect ratio. This would result in the bundles having further to slide past one another leading to a higher elongation at break. In future studies, USANS will be used to look at large scale ordering within the fibers and CNT/CSA solutions. Finally, Figure 5.35c shows toughness of the fibers with CNT concentration. With a large increase in both tensile strength and elongation at break at low concentration spin dope solutions, the 0.5 wt% fibers have ∼350% increase in toughness over the 3.0 wt% fibers.

Fibers were also spun from a different lot of CNTs (Meijo 301 Lot 5R79H06C) to produce fibers for USANS experiments and confirm the results above. As shown in Figure 5.37, the fibers spun with this material shows similar trends. The diameter increases with increasing CNT concentration, the tensile strength decreases with increasing CNT concentration, and the electrical conductivity is relatively constant.
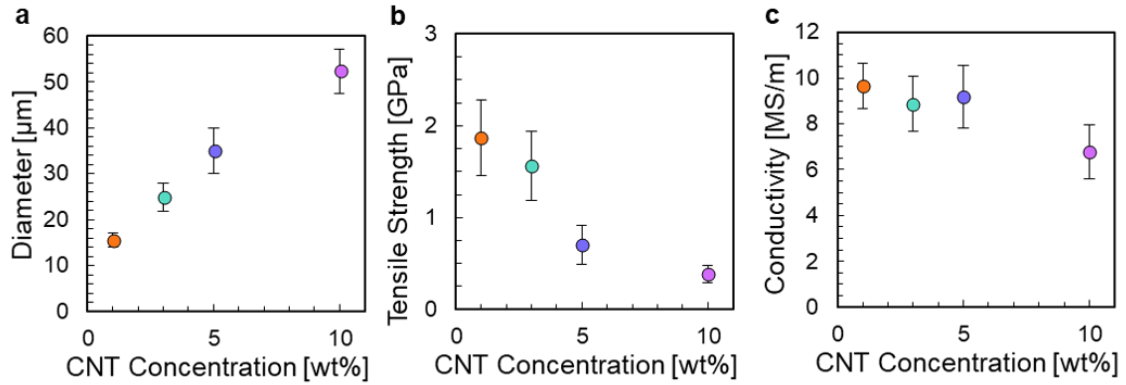
Figure 5.37 : (a) Fiber diameter, (b) tensile strength, and (c) electrical conductivity as a function of CNT concentration in the spin dope.

However, the 10 wt% fiber has a lower conductivity than the other fibers; this can be attributed to the processing difficulties of high concentration CNT/CSA solutions. Solutions at 10 wt% have an extremely high viscosity and do not flow. This can cause void spaces in the fiber due to the presence of air in the high viscosity spin dope. By understanding the mechanism for improvement in tensile strength, post-processing methods can be developed to obtained the desired fiber structure in fibers spun at high concentration.

Due to the promising results of spinning of these experiments, CNTs with different aspect ratios (Tuball - L/D 1100, Meijo Lot 8302305 – L/D 3600, Meijo Lot 7110205 – L/D 4300, and Meijo 101 – L/D 6700) were spun at 0.5 wt% to optimize fiber tensile properties. The results are shown in (Figure 5.38). The tensile strength and electrical conductivity trend with a power law of ∼0.8–0.9 with aspect ratio. This is in good agreement with the results discussed in Section 5.7. Due to the improved processing conditions, the tensile strength has a very strong correlation. However, the conductivity data has more noise likely due to variances in CNT sample purity. Finally,
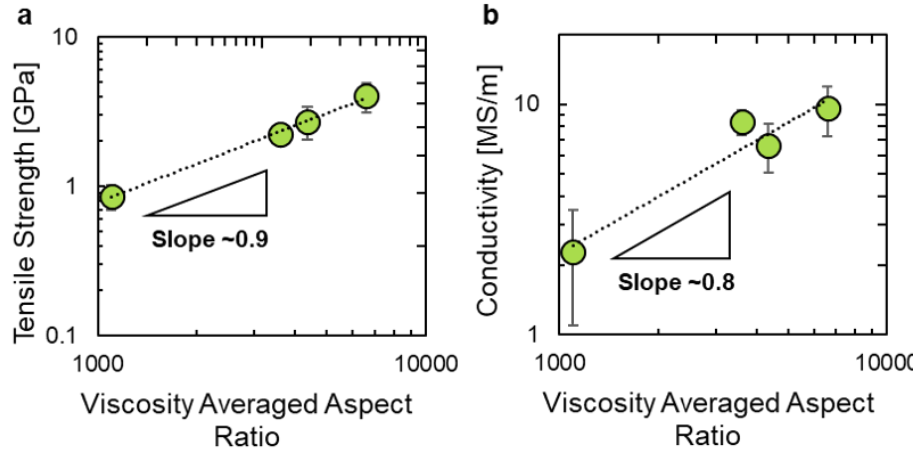
Figure 5.38 : (a) Tensile Strength and (b) Electrical Conductivity of Fibers spun at 0.5 wt% with Various Aspect Ratio CNTs.

these results are compared with data from Ref [59]. In this work, highly aligned films were created by quickly shearing two glass sandwiched with CNT/CSA solution. The films were briefly coagulated, and pieces of film were tightly twisted together to form small fibers. These twisted film based fibers outperformed solution spun fibers when accounting for aspect ratios. However, by decreasing the concentration of CNTs in the spin dope, the gap in properties between these two methods can reconciled.

5.9   Conclusions

In this chapter, improvements in CNT fiber properties and process efficiency (cost and CO_2 footprint) were studied to obtain better understanding of the underlying mechanisms of fiber performance. By studying fiber electrical conductivity over a 3 year period, we demonstrated that post-processing steps such as washing in water or heating in an oven are not necessary for stable fiber performance at room temperature. In fact, these post–processing steps drive off a portion of acid doping which
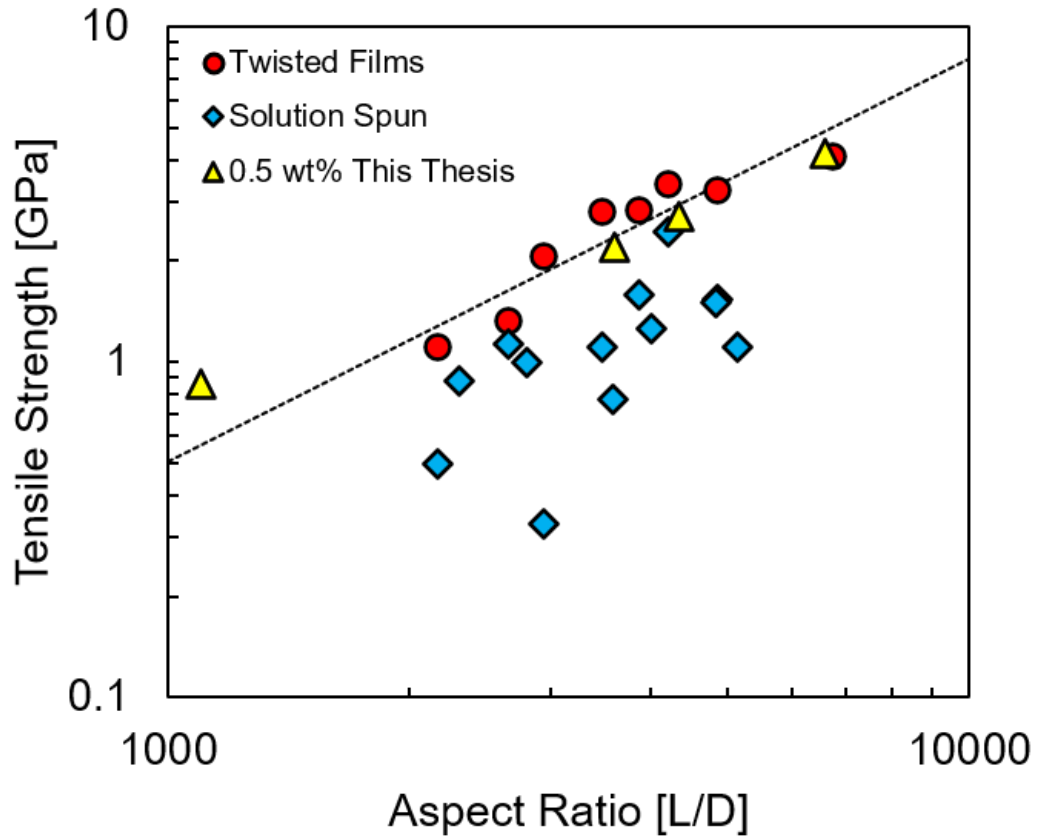
Figure 5.39 : Tensile data from fiber spun at 0.5 wt% compared with results for twisted filaments. The dotted line is the trend line for the twisted films. Figure adapted from Ref [59].

results in lower electrical conductivity. To improve fiber spinning efficiency, the choice of coagulant was studied as acetone is expensive, flammable, and not recyclable as it reacts irreversibly with CSA. These experiments demonstrated that a fast coagulation is necessary to obtain high performance properties without post processing; this suggests that the structure of the fiber is formed within the spinneret. Furthermore, we demonstrated that ammonium acetate can be added to the coagulation bath to

improve the longevity of acetone without hindering fiber performance. We also show promising results towards using water as coagulant. By flushing the interface of the spinneret with water, we are able to suppress the formation of bubbles during the reaction of CSA and water to form a densified fiber. Further studies are necessary to improve the stability of the process.

Research was also performed to understand how the design on the spinneret (i.e. the angle of the inlet cone and diameter of the spinneret) affects fiber formation and ultimate properties. Initial results show that having a smaller inlet cone can improve fiber properties. These results indicate that the fiber may be experiencing die swell and that further property improvements may be obtained by increasing the capillary length of the spinnerets. Furthermore, we demonstrated that CNT purity plays an important role in fiber conductivity, whereas the inclusion of carbon impurities do not have a significant effect on fiber tensile strength. Finally, we see that spinning at low concentration (0.5 wt%) improves the tensile strength of the fibers. Current data suggests that this increase in tensile strength can be attributed to improved structure of CNT bundles within the fiber. These conclusions have driven progress in fiber properties to continue the trend of an average improvement in tensile strength and electrical conductivity of 20% per year to produce CNT fibers with record properties. Continued improvements such as these will allow for the adoption of CNT fibers in a number of important applications with implications for reducing CO_2 emissions.

Chapter 6

Washable, Sewable, All-Carbon Electrodes and Signal Wires for Electronic Clothing*

6.1 Introduction

Wearable electronics are a rapidly growing technology poised to be a $70 billion industry by 2025. The growth of this industry is spurred by consumers' desire to track their daily health and fitness, the expansion of human-machine interfaces driven by the internet of things (IoT), and military and civilian interest to improve monitoring and tracking of personnel performance. Currently, most wearable devices are rigid accessories such as watches, chest straps, or glasses because traditional sensors and signal wires cannot be easily integrated into fabrics [96]. For example, state-of-the-art technology for heart monitoring uses thick, conducting polymer straps that must be worn under athletic clothing (e.g., Polar H10), or indirect sensors that rely on the change in absorbance of flashing light (e.g., Fitbit, Apple Watch). These technologies provide minimal health information because they continuously record heart rate and not electrocardiograms (EKG). High quality EKGs are needed for detecting conditions such as heart conduction disorders and arrhythmias. However, medical grade EKG electrodes cannot be used over an extended period of time. These electrodes require a conductive gel to lower the impedance between the skin-electrode interface. These gels dry out over time ($\sim$5 days), which increases the impedance and degrades the

---

*This chapter is an updated version of a submitted article

quality of EKG recordings [97]. Moreover, commercial EKG electrodes need strong adhesive to achieve good contact with the skin. Both the adhesive and gel can cause skin irritation and allergic reactions [98–100].

To overcome these issues, recent studies have proposed dry EKG electrodes. A common design leverages thin film polymer-based patches that are placed on the skin [101–106]. These patches have good contact impedance because they can conform to the skin surface. However, their ultrathin design can make them difficult to apply, and they must be replaced periodically to limit skin irritation [106]. Fabric-based electrodes are also being developed [107–113]. These electrodes are formed by either dip–coating [107] or screen printing [108–113] conductive inks onto woven textiles. Although fabric-based electrodes are soft and breathable, they are not practical for long-term monitoring because the conductive inks degrade with washing and sweating.

Here, we integrate carbon nanotube thread (CNTT) into stretchable textiles using standard sewing methods to create soft, wearable, dry sensors for noninvasive and continuous EKG monitoring. CNTT is strong and electrically conductive [54], has excellent (low) contact impedance with skin and tissue, [114–116] yet it is also soft and flexible so that it has the mechanical behavior and sensory feeling of a textile thread rather than a thin metal wire [70, 114, 117]. Furthermore, previous work has shown that CNTT is nontoxic on multiple biological scales [118]. CNTT has good cytocompatibility with multiple cell lines, has no impact on immune cells or blood parameters, and no leachable toxicity. We demonstrate that CNTT sensors sewn in a T-shirt can continuously monitor EKG signals as well as commercial (nonwearable) medical electrodes. The same CNTT doubles up as sewable transmission wire, decoupling the placement of sensing, recording, and transmitting electronics, and simplifying signal transmission and fabrication. Finally, the device (T-shirt) can be machine washed

repeatedly without any performance degradation. These properties, combined with recent scaling of CNTT production, make CNTT the material of choice for electrodes and signal wires in wearable sensing, monitoring, and diagnostics.

6.2   Experimental Methods

6.2.1   Fabrication of CNT Thread and Dip–Coated Thread

Fibers were produced via solution spinning as described in the previous chapter. In short, CNTs (EC 1.5 P, Meijo Nano Carbon Co., Ltd.) were used as received and dissolved at 2 wt% in chlorosulfonic acid (99%, Sigma-Aldrich). The solution was extruded through a seven-filament spinneret into a coagulation bath of acetone (99.9%, Sigma-Aldrich). The coagulated fibers were collected on a rotating drum. The drums of fiber were then soaked in room temperature water for 1 hour, heated in oven at 115 °C overnight, and soaked in 60 °C water for 3 hours. The fiber was removed from the drums and plyed together using a custom rope-making device to form thread (Figure 6.1). CNT ink was fabricated by tip sonicating (Qsonica Q55) 0.2 wt% CNTs (EC 1.5 P, Meijo Nano Carbon Co., Ltd.) in 10mL of 1 wt% aqueous sodium deoxycholate (Fisher Scientific) for 60 minutes at 15 W. The CNT ink was then centrifuged at 10000g (Thermo Scientific Sorvall Legend x1) for 2 hours to remove undispersed solids. Cotton thread (Coats & Clark) was dip-coated in the CNT ink and washed with ethanol (200 proof, Decon Laboratories) to remove sodium deoxycholate before being allowed to air dry.
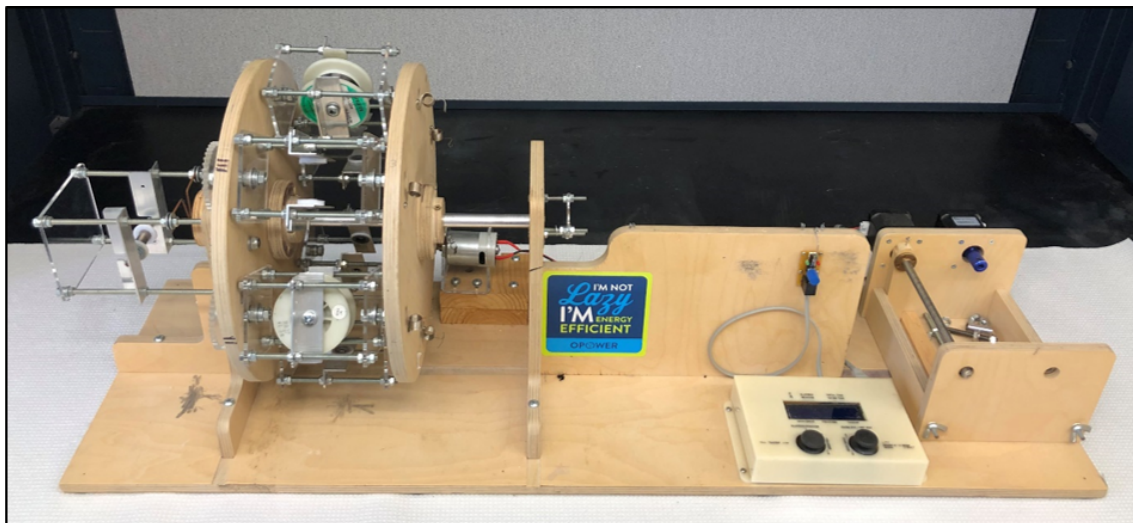
Figure 6.1 : Custom-built continuous rope plying machine. Bundles of 7 filaments of fiber twisted together and three of these twisted bundles are plyed together with an opposite twist to create 21-filament threads.

6.2.2 Characterization of CNTs and CNT Fiber

The raw CNTs were imaged using transmission electron microscopy (JOEL 2100–F HR TEM). The G/D ratios of the CNTs are averages from three measurements for three different lasers (532 nm, 633 nm, and 785 nm wavelength lasers) using a Renishaw InVia Confocal Raman microscope. The viscosity averaged aspect ratio (L/D) was measured via a capillary breakup extensional rheometer using a dilute solution (79 ppmw) of CNTs in chlorosulfonic acid (Trimaster Capillary Thinning Rheometer) as described in Ref [49]. The diameter of the fiber was measured by taking top-down SEM images of 36 segments of fiber (FEI Helios NanoLab 660 DualBeam). The tensile strength was determined by averaging the breaking strength of 42 samples using a 20 mm gauge length at a speed of 0.1 mm/s (TA Instruments ARES G2 Rheome-

ter). The DC resistance of the CNT fiber and dip-coated thread was measured using a custom-built four-point probe connected to a multimeter (HP 34401A). The diameter of the dip-coated thread was measured using an optical microscope (Zeiss Axioplan light microscope). Nitrogen adsorption isotherms of CNTT were measured on a Quantachrome Autosorb iQ3 BET Surface Analyzer at 77K.

6.2.3 Fabrication of CNTT Electrode

CNTT was sewn into elastic textiles using a Singer 2277 Tradition sewing machine. Cotton thread (Coats & Clark, Inc.) was used as the secondary thread and electrodes were sewn using a zigzag stitch to form patches of CNTT. Electrodes were sewn with 2, 15, 30 and 60 cm of fiber. CNT dip-coated thread was sewn into electrodes using 30 cm of thread with the same process described above. Wearable electronic textiles were also fabricated by sewing CNTT inside of athletic t-shirts so that the thread could contact the skin. One shirt was sewn with 5 (4 working electrodes and 1 ground electrode), 15 cm electrodes into the chest of a shirt. CNTT transmission wires were sewn to carry the EKG signal from the sensors to standard electrode clips on the right side of the body. A second shirt was sewn with 2, 15 cm electrodes under the chest area of the shirt. In this shirt, CNTT data transmission wires were sewn on the top of the shirt from the electrodes to the back of the neck. At the neck, snaps (Prym) were inserted and connected to the terminal of the CNT transmission wire.

6.2.4 Characterization and Testing of Electrodes

Electrochemical impedance spectroscopy of the skin-electrode interface was acquired using a Gamry Reference 600 Potentiostat-Galvanostat from 1 to 10,000 Hz. EKG measurements were obtained using a Ganglion Board from OpenBCI using a

sampling rate of 200 Hz. EKGs from 3M™ Red Dot™ electrodes and CNTT electrodes were acquired simultaneously. Studies were performed with two sets of CNTT electrodes on 3 authors (2 males and 1 female). A Savitzky-Golay filter was used offline to correct the baseline of the raw data for analyzing. Data was analyzed by calculating the amplitude of the QRS complex and the variance of the noise over 1000 data point regions. This was repeated for each data set and duplicated for a second

Device	Subject 1	Subject 2	Subject 3
2 cm CNT Devices	0.017	–	0.004
15 cm CNT Devices	0.16	0.31	0.057
30 cm CNT Devices	0.14	0.16	0.097
60 cm CNT Devices	0.28	0.40	0.39
Dip–Coated Devices	0.45	0.55	0.15
Washed Dip–Coated Devices	0.0069	0.013	0.00017
Washed 30 cm CNT Devices	0.30	0.58	0.82
Stretched 30 cm CNT Devices	0.54	0.43	0.92

Table 6.1 : P values for each set of testing conditions from an unpaired t–test. Significant results are highlighted in light blue ($P<0.05$).

set of devices to determine a mean signal–to–noise ratio (SNR) and standard deviation for each category of device tested. The textile electrodes were washed using a portable washing machine (Panda) with Tide® Free and Gentle™ detergent. Bands were spun dry and heated in an oven at 45 °C for 1 hour to remove residual water. 30 cm CNTT electrodes were subjected to cyclic stretching on an electric motor. Devices
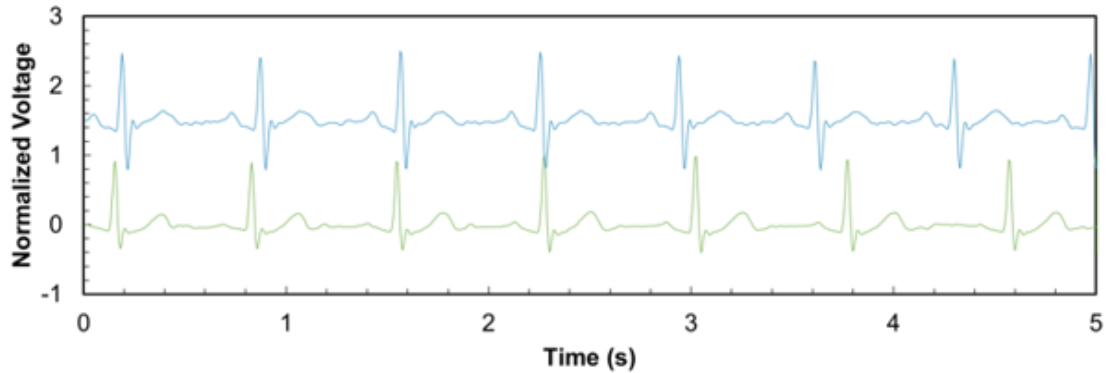
Figure 6.2 : Blinded EKG signals sent to three cardiologists to evaluate. The cardiologists were asked which of the following statements best described the data:

1. The blue is much better than the green.

2. The blue is slightly better than the green.

3. The blue and the green are about the same quality.

4. The green is slightly better than the blue.

5. The green is much better than the blue.

All three cardiologists selected option 2, that the CNT shirt (blue) is slightly better than the 3M electrode (green).

were stretched to 60% strain at a frequency of $\sim$20 min^{-1} for over 1000 cycles. Results from all tests were analyzed by unpaired t–test with an alpha value of 0.05. All P values are shown in Table 6.1. A Bluetooth transmitter from a commercial heart rate monitor (Polar H10) was connected via the snaps into the neck of the athletic t-shirt sewn with 2 CNTT electrodes. The Polar Beat app was downloaded onto a smartphone and synced with a Polar H10. An author wore the shirt and periodically ran and walked to vary his heart rate. Running, jogging, and walking refer to speeds of $\sim$12, 5, and and 2 miles per hour. The heart rate was transmitted to a smartphone

via Bluetooth. An FDA–approved [119] Holter (TLC5007, CONTEC Med) was used to record EKGs from the 5-electrode shirt. Then, commercial electrodes were placed at the same testing sites and EKGs were taken directly afterwards for comparison. Three cardiologists were sent blinded signals to evaluate the quality of the EKGs (Figure 6.2).

6.3   Results and Discussions

6.3.1   CNT and CNTT Characterization

Neat, monofilament CNT fibers were produced by solution spinning [11, 12, 54]. The constituent CNTs had an average diameter of 1.8 nm and 1.5 walls (measured by transmission electron microscopy, Figure 6.3) and a viscosity-average aspect ratio (length to diameter ratio) of 4100, corresponding to an average length of $\sim 7.4\,\mu$m [49]. The crystallinity of the CNTs was measured by comparing the relative intensity of
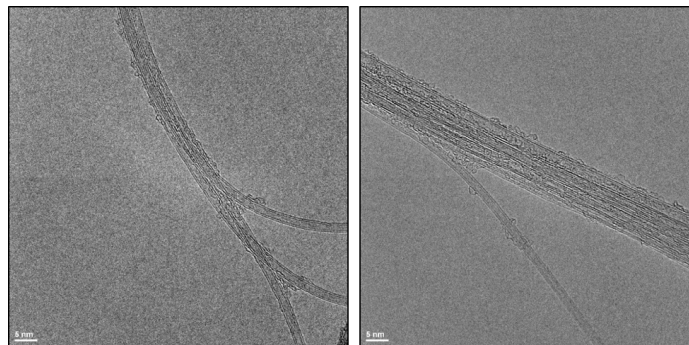
Figure 6.3 : Transmission electron microscopy images of Meijo 1.5 P CNTs used for this study. The CNTs have an average diameter of 1.8 nm with an average of 1.5 walls. Images courtesy of O. S. Dewey.

the Raman G peak (arising from sp^2 hybridized carbon-carbon stretching) to the
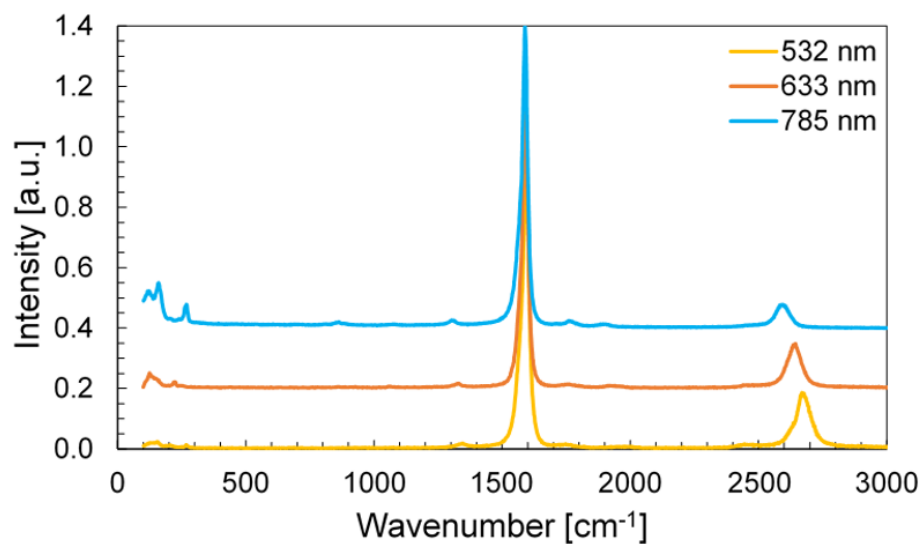
Figure 6.4 : Representative Raman spectra of raw CNTs using a 532 nm, 633 nm, and 785 nm laser. The G peak is located at ∼1590 cm^{-1} and the D peak is located at ∼1350 cm^{-1}. Spectra are shifted 0.2 a.u. for visualization of the D peak. The G/D ratios of 70, 65, and 44 for 532 nm, 633 nm, and 785 nm lasers, respectively demonstrate the high crystallinity of the CNTs.
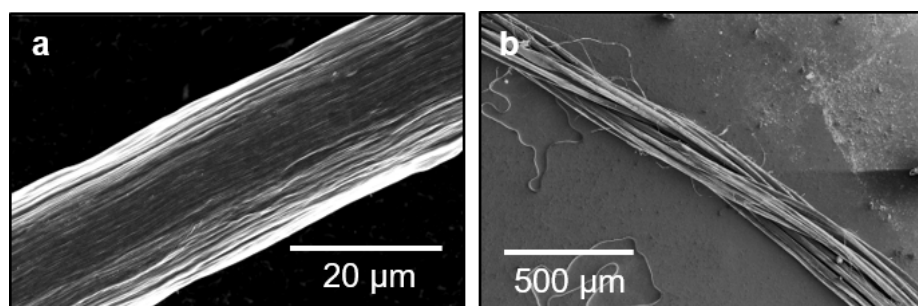
Figure 6.5 : (a) Scanning electron microscopy images of a single filament of CNT fiber and (b) 21 filament CNTT.

Raman D peak (arising from defected six–member rings or sp^3 hybridized carbon–carbon stretching). The CNTs had average Raman G to D ratios of 70, 65, and 44 for 532 nm, 633 nm, and 785 nm lasers, respectively, indicating the CNTs were highly crystalline (Figure 6.4). A scanning electron microscopy (SEM) image of a single, continuous filament of CNT fiber is shown in Figure 6.5a, indicating high CNTs axial alignment. The fiber filament was cylindrical in shape with 22.0 ± 1.0 μm diameter, 1570 kg/m^3 density, 6.6 ± 0.7 MS/m electrical conductivity (specific conductivity of 4.2 ± 0.1 kS m^2/kg) and 1.7 ± 0.2 GPa tensile strength (tenacity of 1.1 ± 0.1 N/tex). Figure 6.6 shows representative stress–strain curves of single filaments of fiber. A custom–built rope making device (Figure 6.1) was used to ply 21 filaments of
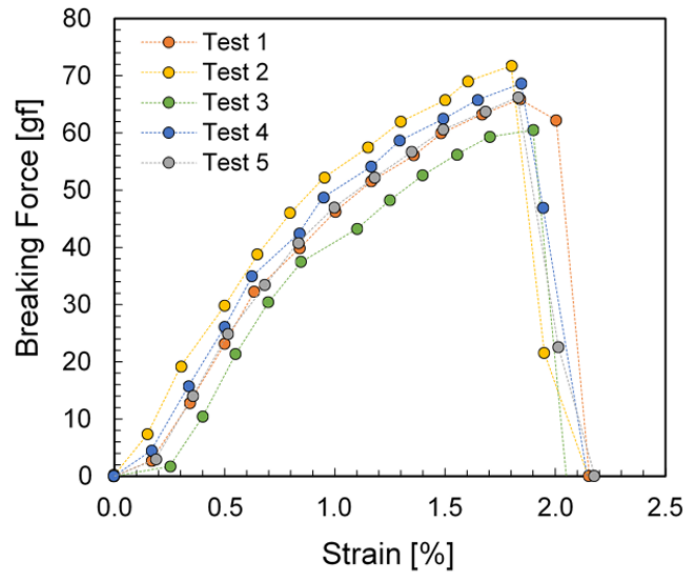
Figure 6.6 : Representative stress–strain curves for individual filaments of CNTF used to create the CNT EKG electrodes. The ultimate tensile strength is ~1.7 GPa and the elongation at break for the filaments is ~2%.

CNT fiber to form a sewing thread; an SEM image of the CNTT is shown in Figure

6.5b. Finally, the specific surface area of the CNTT using Brunauer–Emmett–Teller (BET) theory was 630 m^2/g, with an external surface area (i.e., excluding the internal CNT cavities) of 470 m^2/g and a geometrical surface area of 0.116 m^2/g (Figure 6.7).
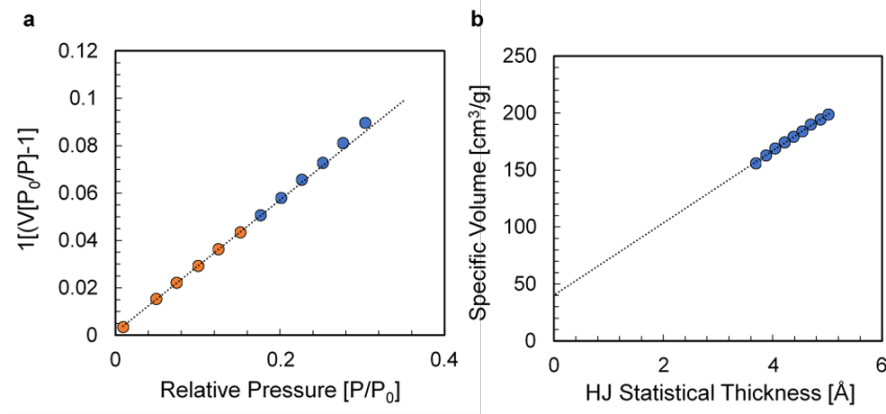
Figure 6.7 : (a) Brunauer–Emmett–Teller (BET) plot of N_2 adsorption isotherms for typical CNT thread used in these studies. A reduced BET region was used to avoid overestimation of the surface area by micropore filling. The BET surface area is estimated as 630 m^2/g. (b) Corresponding N_2 adsorption t–plot using the Harkins–Jura isotherm. The y–intercept indicates a micropore volume of 0.98 cm^3/g demonstrating the highly microporous nature of the CNT thread. The specific external surface area is 470m^2/g. Data courtesy of S. M. Williams.

6.3.2 Evaluation of CNTT Electrodes

We sewed CNTT into stretchable textiles to create electrodes that can be worn on the wrists (Figure 6.8a). From left to right in Figure 6.8a, the 1.5 cm wide textiles were sewn with 2 cm, 15 cm, 30 cm, and 60 cm of CNTT corresponding to a macroscopic geometric surface area of 0.1 cm^2, 0.9 cm^2, 1.8 cm^2, and 3.6 cm^2, respectively. As the individual CNT fiber filaments have high axial stiffness ($\sim$140 GPa, $\sim$2% elongation
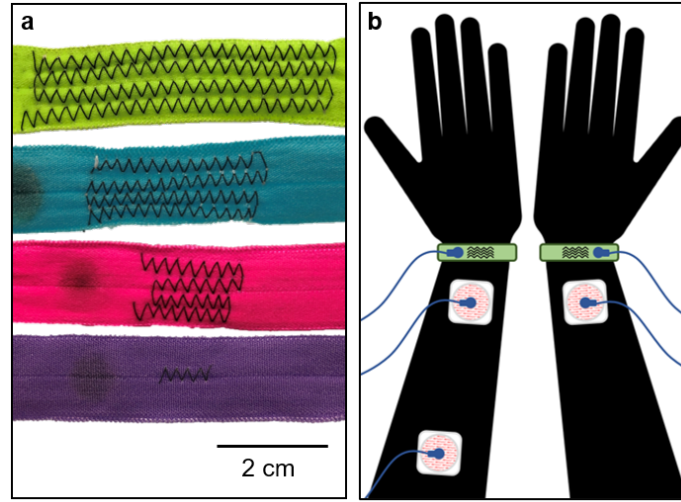
Figure 6.8 : (a) A photograph of CNTT sewn into elastic textiles. CNTT was sewn at 2 cm (purple), 15 cm (pink), 30 cm (teal) and 60 cm (green) lengths. (b) A diagram of the placement of the CNT and commercial electrodes during testing. The commercial electrode closer to the elbow was used as a ground electrode.

to break) but low bending stiffness [70], they were sewn in a zigzag pattern which enabled the CNTT structure to stretch together with the textile (Figure 6.6).

The elastic textiles were tied on the wrists to test the sensor impedance and to collect EKG signals. A 3M™ Red Dot™ ground electrode was placed in the arm cubital fossa and two additional 3M™ Red Dot™ electrodes were placed adjacent to the CNTT electrodes for side-by-side comparison of the acquired signals. Figure 6.8b shows the EKG recording setup, and Figure 6.9a shows the skin-electrode impedance over a frequency range of 1 Hz to 10 kHz for the CNTT electrodes, and the commercial electrodes. Increasing the size of the CNTT electrode does not significantly reduce the impedance, and the higher impedance for the CNTT electrodes compared to the commercial electrodes does not negatively affect sensor performance. Figure
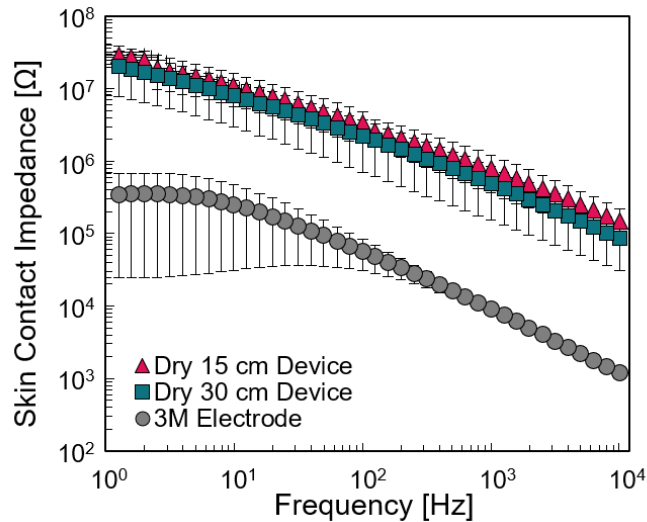
Figure 6.9 : Impedance spectra of CNTT electrodes and commercial electrodes.

6.10 shows a representative EKG signal collected simultaneously from a 3 cm by 1.5 cm patch containing 30 cm (1.8 cm^2) of CNTT (top) and 3M^{TM} Red Dot^{TM} electrode (bottom). The signals were collected using a Ganglion board equipped with a 100 MΩ instrumentation amplifier. Both sets of electrodes can clearly detect the P wave (atrial depolarization), QRS complex (ventricular depolarization), and T wave (ventricular repolarization) which are important for assessing the heart rhythm. The EKGs from the CNTT and commercial electrodes are indistinguishable, demonstrating the high quality of the signal obtained with CNTT electrodes. CNTT electrodes were also used to collect a surface electromyogram (EMG). For this experiment, a CNTT electrode was placed on the wrist and on the forearm and a commercial ground electrode was placed near the elbow (Figure 6.11). The subject then engaged the muscles in his forearm by clenching his fist. Figure 6.11 shows the EMG collected by the CNTT electrodes where the white arrows denote the subject engaging the muscles and the black arrows denote the subject relaxing the muscles. The activation potential of the
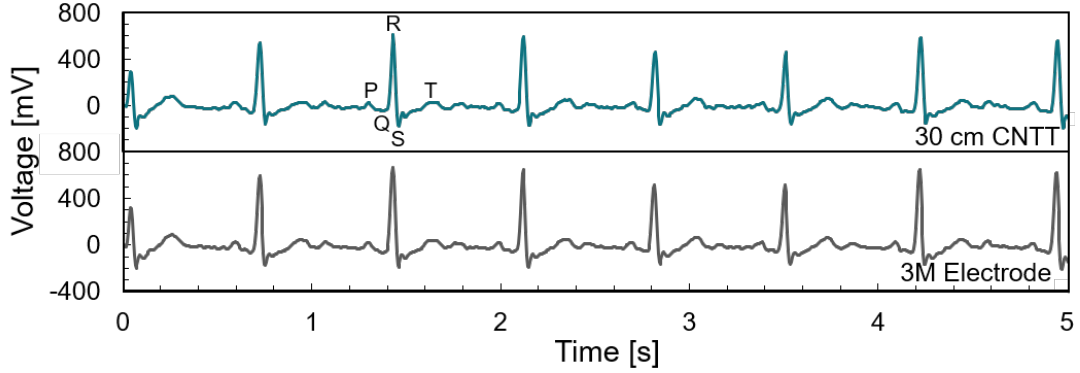
Figure 6.10 : Representative EKG signals over time from 30 cm CNTT electrodes (top) and commercial electrodes (bottom). The signals show no significant differences, and both clearly show the QRS complex, T-wave, and P-wave.

muscles is clearly distinguishable from the baseline signal demonstrating that CNTT electrodes can function as noninvasive EMG electrodes.

The signal quality of various lengths of CNTT were tested using two identical sets of electrodes on three subjects. The SNR of the EKG was calculated as

$$SNR = \frac{A_{signal}}{\sigma_{noise}}, \tag{6.1}$$

where A_{signal} is the amplitude of the RS complex, and σ_{noise} is the variance in the noise of the baseline (the region between the T and P wave). SNR can vary drastically from subject to subject and day to day, due to variations in environmental and skin conditions such as humidity and skin dryness, as well as natural differences in cardiac rhythm. Therefore, the SNR for the CNTT electrodes and 3M™ Red Dot™ electrodes were compared for each electrode type and each subject and are shown in Figure 6.12. For CNTT electrodes with 15 cm (0.9 cm^2) of thread and longer, there is no significant difference between the SNR acquired from the CNTT electrodes and the
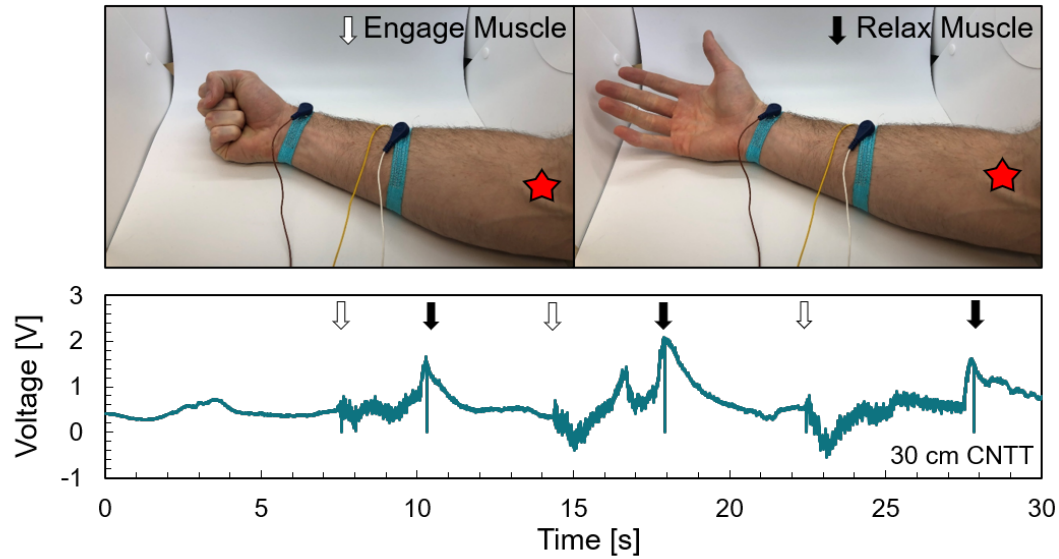
Figure 6.11 : Top: Placement of the CNT thread electrodes during EMG testing. The clinched fist (left) demonstrates muscle contraction, and the hand open (right) demonstrates the relaxed state. The red stars denote the placement of the commercial ground electrode on the elbow. Bottom: EMG signals recorded from activating muscles in the forearm. The white arrows indicate the beginning of the muscle contraction and the black arrows indicate the end of the contraction and the beginning of the relaxation phase.

commercial electrodes for any of the subjects (P>0.05)–the signal quality degrades once the electrode is smaller than ~ 2 cm (0.1 cm^2).

6.3.3 Comparison with Dip–Coated Materials and Performance Under Stress

We compared our CNTT electrodes to devices sewn with cotton thread dip–coated in surfactant–dispersed CNT solution to demonstrate the practicality of neat CNTT.
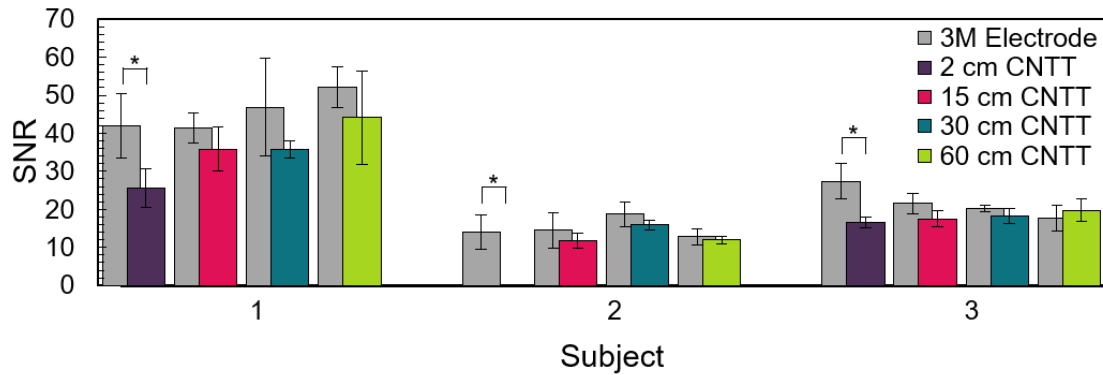
Figure 6.12 : SNRs for each length of the CNTT electrode for three subjects (* P<0.05).

The dip–coated cotton thread had a diameter of ∼240 μm and a conductivity of ∼0.01 MS/m. Each of the electrodes used ∼30 cm of dip–coated cotton thread. The same experimental protocol was followed for the dip–coated thread devices. Figure 6.13 shows that the CNTT and dip-coated thread electrodes had a SNR statistically identical to the commercial wet electrode (P>0.05). The electrodes were then
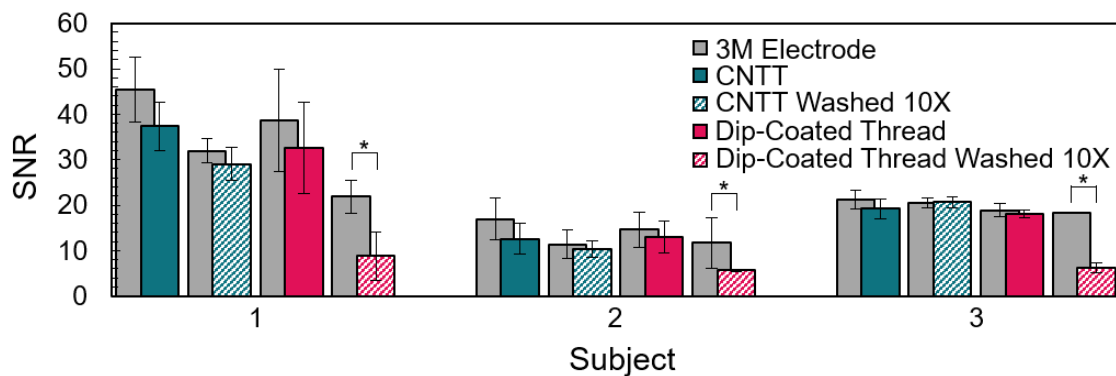
Figure 6.13 : SNR of pristine CNTT electrodes and CNT dip–coated thread compared to CNTT and dip–coated thread that was washed 10 times. There was a noticeable degradation in SNR for the dip-coated thread after washing (* P<0.05).
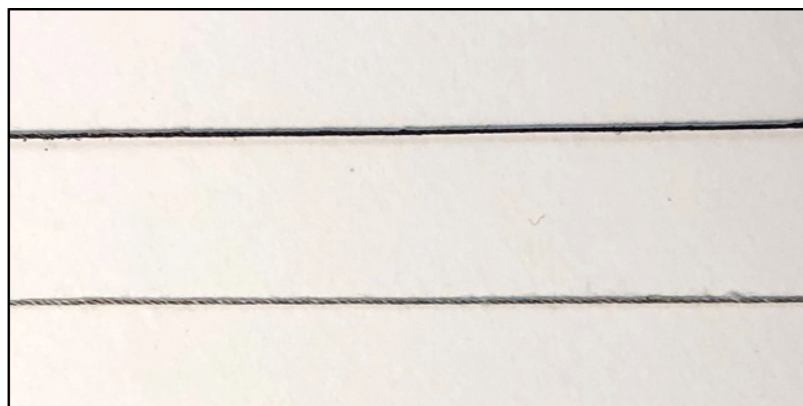
Figure 6.14 : Image of a pristine dip–coated cotton thread (top) and dip–coated cotton thread after 10 washing cycles (bottom). The pristine thread is uniformly black in color. After the washing cycles, the CNT coating is now nonuniform and noticeably lighter in color.
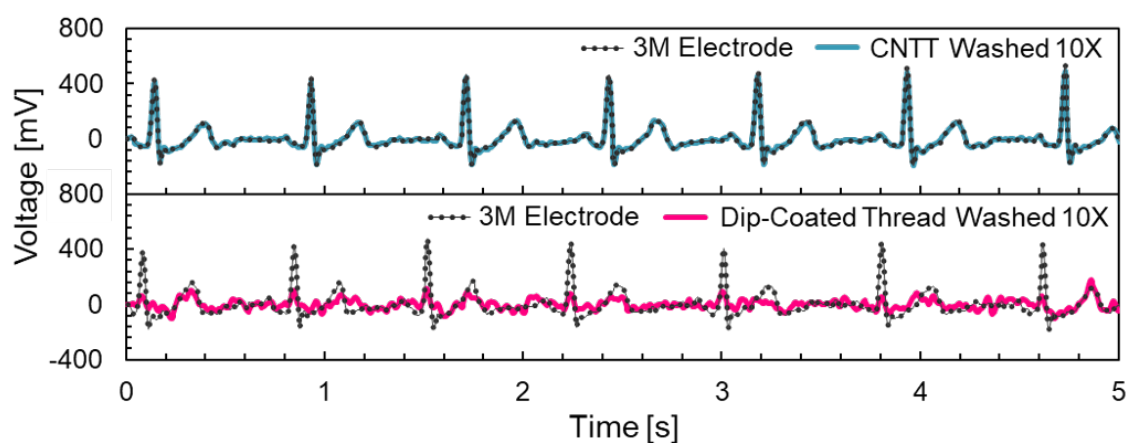
Figure 6.15 : EKG signal for washed dip-coated thread electrodes compared to commercial electrodes. The P-wave and T-wave are indistinguishable from the noise for the dip-coated thread.

washed in a washing machine using commercial detergent and dried in an oven at 45 °C. This process was repeated 10 times, and the electrodes were retested. The CNTT electrodes maintained a SNR comparable to the commercial electrode in all of the experiments (P>0.05). However, the dip–coated thread showed noticeable degradation after washing (P<0.05). Visually, the cotton thread was lighter in color indicating that the CNTs do not adhere strongly to the cotton and were partially removed during washing (Figure 6.14). Additionally, a direct comparison of the signal obtained by the washed CNTT electrodes and dip-coated electrodes versus the commercial electrodes is shown in Figure 6.15 The RS complex was still somewhat discernible for the dip–coated signal but the lower–amplitude features such as the P–wave and T–wave were lost in the background noise. Finally, the CNTT electrodes were strained to the textile's maximum strain (∼60%) and relaxed over 1000 times. The CNTT electrodes showed no discernible degradation in SNR after repeated strain (Figure 6.16).

6.3.4 CNTT Electrode Shirts

CNTT was sewn into the chest of athletic shirts to demonstrate functioning electronic textiles. In Figure 6.17a, we connected two CNTT electrodes to the Bluetooth transmitter of a commercial heart rate monitor (Polar H10) that is designed to work with a polymeric strap and embedded silicon sensors that is worn across the user's chest (Figure 6.17a inset). The electrodes were sewn into the inside of the shirt around the rib area to allow contact with the skin. Additionally, CNTT was sewn on the outside of the shirt from the electrodes on the chest to the back of the neck. At the neck of the shirt, the CNTT thread was connected via standard electrode buttons to the Bluetooth transmitter (Figure 6.18) that sent heart rate data to a
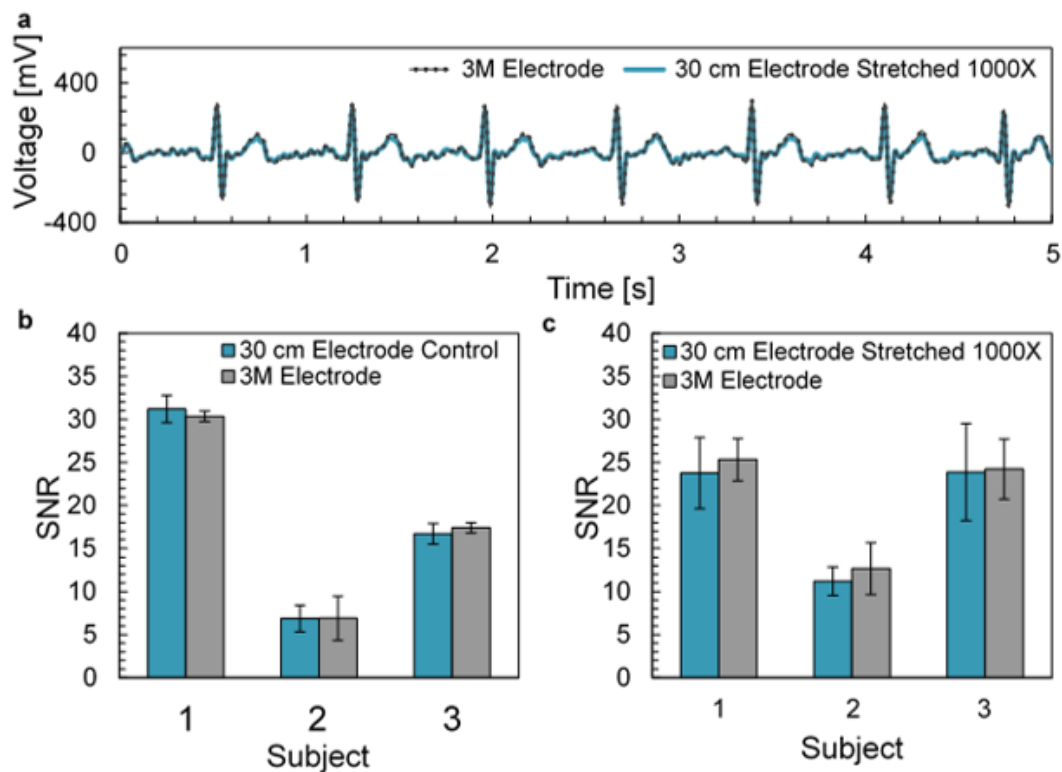
Figure 6.16 : (a) Representative EKG signals from 30 cm CNTT electrodes stretched 1000 times and commercial 3M electrodes. Signal to noise ratio of 30 cm CNT devices before stretching (b) and after 1000 stretch cycles (c). In both cases, the signal to noise ratio is within error of the 3M electrode (P<0.05).

smart phone (Figure 6.17a) while the subject ran and walked. Figure 6.17b shows EKG signals obtained from a Holter monitor using a CNTT electrode athletic shirt and commercial electrodes. CNTT carries the signal to the side of the shirt so that the electronics can fit into a pocket. In a blinded study, three cardiologists evaluated the signals and independently determined that signal from the CNT shirt was slightly better than the 3M electrodes due to better definition of the p-wave (Figure 6.2). These results demonstrate that CNTT sensors and wires integrate seamlessly
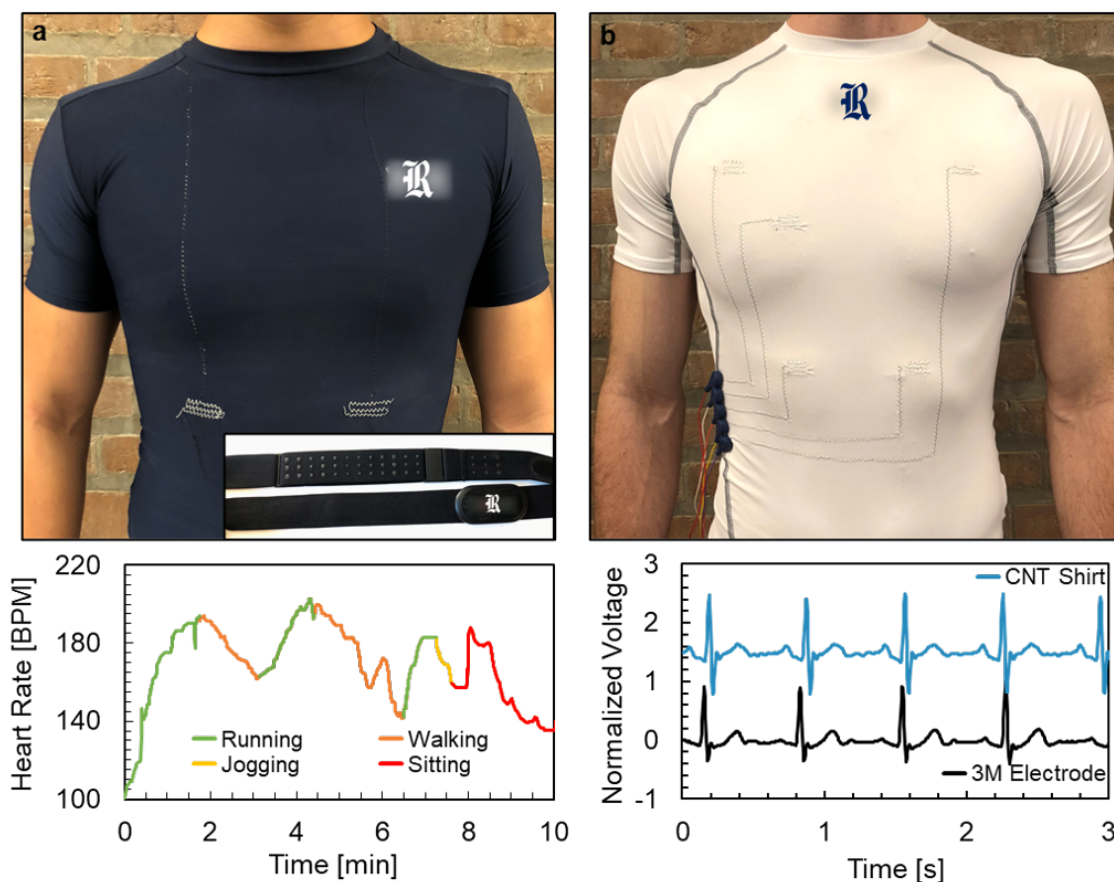
Figure 6.17 : (a) An athletic shirt sewn with 2 CNTT electrodes. The electrodes are connected to a commercial wireless heart rate monitor using CNTT transmission wires. The shirt was worn by an author, and the heart rate while running, jogging, walking, and sitting was recorded overtime and transmitted to a cell phone. The inset shows a commercial Polar H10 chest strap. (b) An athletic shirt sewn with 5 CNTT electrodes. The electrodes are connected to standard clips to measure an EKG signal (shown below). The electrodes can acquire a quality signal with all of the features easily discernable. Note: The commercial logos have been blurred and replaced with Rice University logos.

Figure 6.18 : Placement of the Polar H10 Bluetooth transmitter on CNTT shirt.

into preexisting systems while functioning as both electrodes and a data transmission line while also allowing transmitting electronics to be placed anywhere on the body to optimize user comfort.

6.4   Conclusions

CNTT is ideal for wearable textiles; it is soft and flexible, machine washable, and is easily integrated into clothing or textiles, like standard thread. Its electrical conductivity is on par with metals, yet has better chemical resistance, can withstand greater flex fatigue, and has a higher tensile strength. We have demonstrated that neat CNTT can be sewn into textiles and used to obtain EKGs similar in quality to commercially available, adhesive, wet electrodes. Moreover, CNTT electrodes function as sensors for surface EMG. Finally, CNTT can also be used as transmission wires to carry signal to other locations on the body, allowing the placement of transmitters in convenient locations away from the signal collection sites. The results demonstrated in this work open a number of possibilities for future studies of CNTT in textile–based

electronics and health monitoring systems. CNTT can be used to bridge soft components and sensors to traditional electronic components making them a key component towards development of fully textile-based circuits. CNTT-derived technologies such as fiber-based antennas [15], light emitting diodes [17], or semiconducting fibers [16] can be similarly sewn into textiles. Moreover, minor modifications to CNTT geometry and microelectronics could allow other health-monitoring applications including blood pressure, force exertion, and respiratory rate sensing capabilities. CNTT could transform the next generation military uniforms as ballistic protection [82], vitals monitoring, and location tracking could be easily incorporated into a single platform. Moreover, woven electronics could also improve human-machine interfaces in car upholstery and soft robotics. As demonstrated here, the integration of multiple functionalities would be straightforward as minimal engineering is needed to combine like-materials. The unique combination of sewablity, durability, and functionality demonstrated in this work represents a major step forward towards truly wearable electronic textiles.

Chapter 7

Conclusions

Most as produced CNTs contain a significant amount of impurities in the form of amorphous carbon and catalyst. Amorphous carbon adheres to the sidewalls of the CNTs which impedes protonation by CSA molecules, limiting CNT dissolution. By heating CNTs to moderate temperatures (400-460 °C) in air, the amorphous carbon can be removed which allows for CNT solubility. Beyond enhanced solubility, purification plays an important role in CNT fiber properties. We demonstrated that sample purity has a large effect on fiber electrical conductivity, whereas it does not have a significant effect on tensile strength. While increasing oxidation temperature or oxidation time will remove additional carbonaceous impurities, it also will decrease the aspect ratio of the CNTs. This is an important consideration when selecting purification conditions because shorter CNTs will decrease both fiber electrical conductivity and tensile strength.

We also show that improvements in tensile strength can be obtained by decreasing the concentration of CNTs in the spin dope. We attribute this enhancement in tensile strength to improved ordering of CNTs within the fiber. By understanding the structure-property relationships of CNT fibers, we can develop post processing methods to mimic the structure of fibers spun at low concentration with fibers spun at higher concentration. This is essential for improving fiber spinning efficiency. We also demonstrate that additional gains in properties can be achieved by decreasing the angle of the spinneret inlet cone. This result indicates that the fiber is under-

going die–swell and that further improvements in fiber properties may be possible by increasing the length of spinneret to provide additional stress dissipation by viscous forces. These developments in fiber spinning has lead to the production of CNT fibers with a tensile strength of 4.2 GPa and an electrical conductivity of 10.9 MS/m, the highest electrical conductivity for CNT fibers in literature. These advancements have continued an impressive trend in solution spun CNT fiber properties over time; the tensile strength and electrical conductivity have improved an average of $\sim$20% per year. With continued progress, CNT fibers will soon become the strongest fiber material with conductivity on par with the best metals.

Finally, we demonstrate the application of CNT fiber for wearable health monitoring. CNT fiber was able to be sewn into textiles and athletic shirts to be used as washable EKG electrodes. An athletic shirt was sewn with five CNTT. These electrodes were connected to CNTT transmission lines that carried the signal to a convenient position to connect with a Holter. The shirt was able to obtain EKG signals of similar quality to commercial electrodes. These results are exciting for additional applications of CNT thread for electronic textiles. This material has the potential to be used for additional monitoring applications such as blood pressure, force exertion, and respiratory rate sensing as well as be a key component to develop fully integrated textile circuits.

Bibliography

[1] R. S. Ruoff and D. C. Lorents, "Mechanical and thermal properties of carbon nanotubes," Carbon, vol. 33, no. 7, pp. 925–930, 1995.

[2] J.-P. Salvetat, J.-M. Bonard, N. H. Thomson, A. J. Kulik, L. Forró, W. Benoit, and L. Zuppiroli, "Mechanical properties of carbon nanotubes," Applied Physics A, vol. 69, pp. 255–260, Sept. 1999.

[3] M. M. J. Treacy, T. W. Ebbesen, and J. M. Gibson, "Exceptionally high Young's modulus observed for individual carbon nanotubes," Nature, vol. 381, pp. 678–680, June 1996.

[4] T. Ando, "The electronic properties of graphene and carbon nanotubes," NPG Asia Materials, vol. 1, pp. 17–21, Oct. 2009.

[5] T. W. Odom, J.-L. Huang, P. Kim, and C. M. Lieber, "Atomic structure and electronic properties of single-walled carbon nanotubes," Nature, vol. 391, pp. 62–64, Jan. 1998.

[6] N. Borisenko, S. Zein El Abedin, and F. Endres, "In Situ STM Investigation of Gold Reconstruction and of Silicon Electrodeposition on Au(111) in the Room Temperature Ionic Liquid 1-Butyl-1-methylpyrrolidinium Bis(trifluoromethylsulfonyl)imide," The Journal of Physical Chemistry B, vol. 110, pp. 6250–6256, Mar. 2006.

[7] L. M. Ericson, H. Fan, H. Peng, V. A. Davis, W. Zhou, J. Sulpizio, Y. Wang, R. Booker, J. Vavro, C. Guthy, A. N. G. Parra-Vasquez, M. J. Kim, S. Ramesh, R. K. Saini, C. Kittrell, G. Lavin, H. Schmidt, W. W. Adams, W. E. Billups, M. Pasquali, W.-F. Hwang, R. H. Hauge, J. E. Fischer, and R. E. Smalley, "Macroscopic, Neat, Single-Walled Carbon Nanotube Fibers," <u>Science</u>, vol. 305, pp. 1447–1450, Sept. 2004.

[8] B. Vigolo, A. Pénicaud, C. Coulon, C. Sauder, R. Pailler, C. Journet, P. Bernier, and P. Poulin, "Macroscopic Fibers and Ribbons of Oriented Carbon Nanotubes," <u>Science</u>, vol. 290, pp. 1331–1334, Nov. 2000.

[9] J. Boyd, "Rice lab overcomes supply issue in nanotube commercialization," Feb. 2003.

[10] M. Zhang, K. R. Atkinson, and R. H. Baughman, "Multifunctional Carbon Nanotube Yarns by Downsizing an Ancient Technology," <u>Science</u>, vol. 306, pp. 1358–1361, Nov. 2004.

[11] N. Behabtu, C. C. Young, D. E. Tsentalovich, O. Kleinerman, X. Wang, A. W. K. Ma, E. A. Bengio, R. F. ter Waarbeek, J. J. de Jong, R. E. Hoogerwerf, S. B. Fairchild, J. B. Ferguson, B. Maruyama, J. Kono, Y. Talmon, Y. Cohen, M. J. Otto, and M. Pasquali, "Strong, Light, Multifunctional Fibers of Carbon Nanotubes with Ultrahigh Conductivity," <u>Science</u>, vol. 339, pp. 182–186, Jan. 2013.

[12] D. E. Tsentalovich, R. J. Headrick, F. Mirri, J. Hao, N. Behabtu, C. C. Young, and M. Pasquali, "Influence of Carbon Nanotube Characteristics on Macroscopic Fiber Properties," <u>ACS Applied Materials & Interfaces</u>, vol. 9, pp. 36189–

36198, Oct. 2017.

[13] V. A. Davis, A. N. G. Parra-Vasquez, M. J. Green, P. K. Rai, N. Behabtu, V. Prieto, R. D. Booker, J. Schmidt, E. Kesselman, W. Zhou, H. Fan, W. W. Adams, R. H. Hauge, J. E. Fischer, Y. Cohen, Y. Talmon, R. E. Smalley, and M. Pasquali, "True solutions of single-walled carbon nanotubes for assembly into macroscopic materials," Nature Nanotechnology, vol. 4, pp. 830–834, Dec. 2009.

[14] S. Ramesh, L. M. Ericson, V. A. Davis, R. K. Saini, C. Kittrell, M. Pasquali, W. E. Billups, W. W. Adams, R. H. Hauge, and R. E. Smalley, "Dissolution of Pristine Single Walled Carbon Nanotubes in Superacids by Direct Protonation," The Journal of Physical Chemistry B, vol. 108, pp. 8794–8798, July 2004.

[15] E. Amram Bengio, D. Senic, L. W. Taylor, D. E. Tsentalovich, P. Chen, C. L. Holloway, A. Babakhani, C. J. Long, D. R. Novotny, J. C. Booth, N. D. Orloff, and M. Pasquali, "High efficiency carbon nanotube thread antennas," Applied Physics Letters, vol. 111, p. 163109, Oct. 2017.

[16] O. S. Dewey, R. J. Headrick, L. W. Taylor, M. Pasquali, G. Prestopino, G. Verona Rinati, M. Lucci, and M. Cirillo, "Transport and photo-conduction in carbon nanotube fibers," Applied Physics Letters, vol. 115, p. 023101, July 2019. Publisher: American Institute of Physics.

[17] V. Jamali, F. Niroui, L. W. Taylor, O. S. Dewey, B. A. Koscher, M. Pasquali, and A. P. Alivisatos, "Perovskite-Carbon Nanotube Light-Emitting Fibers," Nano Letters, vol. 20, pp. 3178–3184, May 2020. Publisher: American Chemical Society.

[18] S. Iijima, "Helical microtules of graphitic carbon," Nature, vol. 354, pp. 56–58, Nov. 1991.

[19] M. Fujii, X. Zhang, H. Xie, H. Ago, K. Takahashi, T. Ikuta, H. Abe, and T. Shimizu, "Measuring the Thermal Conductivity of a Single Carbon Nanotube," Physical Review Letters, vol. 95, p. 065502, Aug. 2005.

[20] M.-F. Yu, B. S. Files, S. Arepalli, and R. S. Ruoff, "Tensile Loading of Ropes of Single Wall Carbon Nanotubes and their Mechanical Properties," Physical Review Letters, vol. 84, pp. 5552–5555, June 2000.

[21] M. S. Dresselhaus, G. Dresselhaus, R. Saito, and A. Jorio, "Raman spectroscopy of carbon nanotubes," Physics Reports, vol. 409, pp. 47–99, Mar. 2005.

[22] K. Liu, J. Deslippe, F. Xiao, R. B. Capaz, X. Hong, S. Aloni, A. Zettl, W. Wang, X. Bai, S. G. Louie, E. Wang, and F. Wang, "An atlas of carbon nanotube optical transitions," Nature Nanotechnology, vol. 7, pp. 325–329, May 2012.

[23] M. Endo, M. S. Strano, and P. M. Ajayan, "Potential Applications of Carbon Nanotubes," in Carbon Nanotubes (A. Jorio, G. Dresselhaus, and M. S. Dresselhaus, eds.), no. 111 in Topics in Applied Physics, pp. 13–62, Springer Berlin Heidelberg, 2007.

[24] L. A. Girifalco, M. Hodak, and R. S. Lee, "Carbon nanotubes, buckyballs, ropes, and a universal graphitic potential," Physical Review B, vol. 62, pp. 13104–13110, Nov. 2000.

[25] L. Vaisman, H. D. Wagner, and G. Marom, "The role of surfactants in dispersion of carbon nanotubes," Advances in Colloid and Interface Science, vol. 128–130, pp. 37–46, Dec. 2006.

[26] M. F. Islam, E. Rojas, D. M. Bergey, A. T. Johnson, and A. G. Yodh, "High Weight Fraction Surfactant Solubilization of Single-Wall Carbon Nanotubes in Water," Nano Letters, vol. 3, pp. 269–273, Feb. 2003.

[27] M. S. Strano, V. C. Moore, M. K. Miller, M. J. Allen, E. H. Haroz, C. Kittrell, R. H. Hauge, and R. E. Smalley, "The Role of Surfactant Adsorption during Ultrasonication in the Dispersion of Single-Walled Carbon Nanotubes," Journal of Nanoscience and Nanotechnology, vol. 3, pp. 81–86, Feb. 2003.

[28] C. A. Dyke and J. M. Tour, "Unbundled and Highly Functionalized Carbon Nanotubes from Aqueous Reactions," Nano Letters, vol. 3, pp. 1215–1218, Sept. 2003.

[29] R. K. Saini, I. W. Chiang, H. Peng, R. E. Smalley, W. E. Billups, R. H. Hauge, and J. L. Margrave, "Covalent Sidewall Functionalization of Single Wall Carbon Nanotubes," Journal of the American Chemical Society, vol. 125, pp. 3617–3621, Mar. 2003.

[30] J. L. Bahr and J. M. Tour, "Highly Functionalized Carbon Nanotubes Using in Situ Generated Diazonium Compounds," Chemistry of Materials, vol. 13, pp. 3823–3824, Nov. 2001.

[31] V. A. Davis, L. M. Ericson, A. N. G. Parra-Vasquez, H. Fan, Y. Wang, V. Prieto, J. A. Longoria, S. Ramesh, R. K. Saini, C. Kittrell, W. E. Billups, W. W. Adams, R. H. Hauge, R. E. Smalley, and M. Pasquali, "Phase Behavior and Rheology of SWNTs in Superacids," Macromolecules, vol. 37, pp. 154–160, Jan. 2004.

[32] M. J. Green, A. N. G. Parra-Vasquez, N. Behabtu, and M. Pasquali, "Modeling

the phase behavior of polydisperse rigid rods with attractive interactions with applications to single-walled carbon nanotubes in superacids," The Journal of Chemical Physics, vol. 131, p. 084901, Aug. 2009.

[33] L. Onsager, "The Effects of Shape on the Interaction of Colloidal Particles," Annals of the New York Academy of Sciences, vol. 51, pp. 627–659, May 1949.

[34] P. J. Flory, "Phase Equilibria in Solutions of Rod-Like Particles," Proceedings of the Royal Society of London A: Mathematical, Physical and Engineering Sciences, vol. 234, pp. 73–89, Jan. 1956.

[35] H. H. Wensink and G. J. Vroege, "Isotropic–nematic phase behavior of length-polydisperse hard rods," The Journal of Chemical Physics, vol. 119, pp. 6868–6882, Oct. 2003.

[36] N. Behabtu, Dissolution, processing and fluid structure of graphene and carbon nanotube in superacids: The route toward high performance multifunctional materials. Thesis, Rice University, Sept. 2012. Accepted: 2012-09-06T04:06:10Z.

[37] V. Jamali, N. Behabtu, B. Senyuk, J. A. Lee, I. I. Smalyukh, P. van der Schoot, and M. Pasquali, "Experimental realization of crossover in shape and director field of nematic tactoids," Physical Review E, vol. 91, p. 042507, Apr. 2015.

[38] A. Lucas, C. Zakri, M. Maugey, M. Pasquali, P. v. d. Schoot, and P. Poulin, "Kinetics of Nanotube and Microfiber Scission under Sonication," The Journal of Physical Chemistry C, vol. 113, pp. 20599–20605, Dec. 2009.

[39] G. Pagani, M. J. Green, P. Poulin, and M. Pasquali, "Competing mechanisms and scaling laws for carbon nanotube scission by ultrasonication," Proceedings

of the National Academy of Sciences of the United States of America, vol. 109, pp. 11599–11604, July 2012.

[40] A. N. G. Parra-Vasquez, N. Behabtu, M. J. Green, C. L. Pint, C. C. Young, J. Schmidt, E. Kesselman, A. Goyal, P. M. Ajayan, Y. Cohen, Y. Talmon, R. H. Hauge, and M. Pasquali, "Spontaneous Dissolution of Ultralong Single- and Multiwalled Carbon Nanotubes," ACS Nano, vol. 4, pp. 3969–3978, July 2010.

[41] G. U. Sumanasekera, J. L. Allen, S. L. Fang, A. L. Loper, A. M. Rao, and P. C. Eklund, "Electrochemical Oxidation of Single Wall Carbon Nanotube Bundles in Sulfuric Acid," The Journal of Physical Chemistry B, vol. 103, pp. 4292–4297, May 1999.

[42] A. N. G. Parra-Vasquez, Solubility, length characterization, and cryo-TEM of pristine and functionalized single-walled carbon nanotubes in surfactant and superacid systems, with application to spinning SWNT fibers. Thesis, Rice University, 2010.

[43] L. Weller, F. R. Smail, J. A. Elliott, A. H. Windle, A. M. Boies, and S. Hochgreb, "Mapping the parameter space for direct-spun carbon nanotube aerogels," Carbon, vol. 146, pp. 789–812, May 2019.

[44] T. I. Bair and L. W. G. Jr, "Aramid spinning process," Aug. 1984.

[45] New Carbons - Control of Structure and Functions. Elsevier, 2000.

[46] J. Lee, D.-M. Lee, Y.-K. Kim, H. S. Jeong, and S. M. Kim, "Significantly Increased Solubility of Carbon Nanotubes in Superacid by Oxidation and Their Assembly into High Performance Fibers," p. 8, 2017.

[47] A. R. Bucossi, C. D. Cress, C. M. Schauerman, J. E. Rossi, I. Puchades, and B. J. Landi, "Enhanced Electrical Conductivity in Extruded Single-Wall Carbon Nanotube Wires from Modified Coagulation Parameters and Mechanical Processing," ACS Applied Materials & Interfaces, vol. 7, pp. 27299–27305, Dec. 2015. Publisher: American Chemical Society.

[48] K. L. Strong, D. P. Anderson, K. Lafdi, and J. N. Kuhn, "Purification process for single-wall carbon nanotubes," Carbon, vol. 41, pp. 1477–1488, Jan. 2003.

[49] D. E. Tsentalovich, A. W. K. Ma, J. A. Lee, N. Behabtu, E. A. Bengio, A. Choi, J. Hao, Y. Luo, R. J. Headrick, M. J. Green, Y. Talmon, and M. Pasquali, "Relationship of Extensional Viscosity and Liquid Crystalline Transition to Length Distribution in Carbon Nanotube Solutions," Macromolecules, vol. 49, pp. 681–689, Jan. 2016.

[50] K. Rhodes, "Application Note: Analysis of Iron Oxidation States by XPS," Modern Microscopy, Dec. 2015.

[51] B. I. Yakobson, G. Samsonidze, and G. G. Samsonidze, "Atomistic theory of mechanical relaxation in fullerene nanotubes," Carbon, vol. 38, pp. 1675–1680, Jan. 2000.

[52] I.-W. Wang, D. A. Kutteri, B. Gao, H. Tian, and J. Hu, "Methane Pyrolysis for Carbon Nanotubes and COx-Free H2 over Transition-Metal Catalysts," Energy & Fuels, vol. 33, pp. 197–205, Jan. 2019.

[53] E. Yedinak and R. Meidl, "Measuring the True Cost of Sustainability A Case Study in a Green Energy Approach," Issue Brief no. 04.28.20. Rice University's Baker Institute for Public Policy, p. 7, 2020.

[54] L. W. Taylor, O. S. Dewey, R. J. Headrick, N. Komatsu, N. M. Peraca, G. Wehmeyer, J. Kono, and M. Pasquali, "Improved properties, increased production, and the path to broad adoption of carbon nanotube fibers," Carbon, vol. 171, pp. 689–694, Jan. 2021.

[55] K. Koziol, J. Vilatela, A. Moisala, M. Motta, P. Cunniff, M. Sennett, and A. Windle, "High-Performance Carbon Nanotube Fiber," Science, vol. 318, pp. 1892–1895, Dec. 2007. 00865.

[56] J. Stallard, W. Tan, F. Smail, T. Gspann, A. Boies, and N. Fleck, "The mechanical and electrical properties of direct-spun carbon nanotube mats," Extreme Mechanics Letters, vol. 21, pp. 65–75, May 2018.

[57] D. Conroy, A. Moisala, S. Cardoso, A. Windle, and J. Davidson, "Carbon nanotube reactor: Ferrocene decomposition, iron particle growth, nanotube aggregation and scale-up," Chemical Engineering Science, vol. 65, pp. 2965–2977, May 2010.

[58] N. Behabtu, M. Green, and M. Pasquali, "Carbon nanotube-based neat fibers," Nano Today, vol. 3, pp. 24–34, Oct. 2008.

[59] R. J. Headrick, D. E. Tsentalovich, J. BerdeguÃ©, E. A. Bengio, L. Liberman, O. Kleinerman, M. S. Lucas, Y. Talmon, and M. Pasquali, "Structure-Property Relations in Carbon Nanotube Fibers by Downscaling Solution Processing," Advanced Materials, vol. 30, p. 1704482, Mar. 2018.

[60] H. Corporation, "HexTow IM10 Data Sheet," 2016.

[61] Toray Composite Materials America, Inc., "T700G Standard Modulus Fiber," Apr. 2018.

[62] Mitsubishi Rayown Co. Ltd., "Coal Tar Pitch-based Carbon Fiber (CF) Dialead," Sept. 2016.

[63] T. Q. Tran, Z. Fan, P. Liu, S. M. Myint, and H. M. Duong, "Super-strong and highly conductive carbon nanotube ribbons from post-treatment methods," Carbon, vol. 99, pp. 407–415, Apr. 2016.

[64] J. Lee, D. Lee, Y. Jung, J. Park, H. S. Lee, Y. Kim, C. R. Park, H. S. Jeong, and S. M. Kim, "Direct spinning and densification method for high-performance carbon nanotube fibers," Nature Communications, vol. 10, pp. 1–10, July 2019.

[65] J. N. Wang, X. G. Luo, T. Wu, and Y. Chen, "High-strength carbon nanotube fibre-like ribbon with high ductility and high electrical conductivity," Nature Communications, vol. 5, p. 3848, Sept. 2014.

[66] Q. Zhang, K. Li, Q. Fan, X. Xia, N. Zhang, Z. Xiao, W. Zhou, F. Yang, Y. Wang, H. Liu, and W. Zhou, "Performance improvement of continuous carbon nanotube fibers by acid treatment," Chinese Physics B, vol. 26, p. 028802, Feb. 2017.

[67] X. Wang, V. Ho, R. A. Segalman, and D. G. Cahill, "Thermal Conductivity of High-Modulus Polymer Fibers," Macromolecules, vol. 46, pp. 4937–4943, June 2013.

[68] D. E. Tsentalovich, Purification, Length Characterization and Quality Assessment of Carbon Nanotubes: A Roadmap to Spinning Fibers with Superior Electrical Conductivity and Strength. Thesis, Rice University, Apr. 2015. Accepted: 2020-02-05T14:59:55Z.

[69] R. J. Headrick, M. A. Trafford, L. W. Taylor, O. S. Dewey, R. A. Wincheski, and M. Pasquali, "Electrical and acoustic vibroscopic measurements for determining carbon nanotube fiber linear density," Carbon, vol. 144, pp. 417–422, Apr. 2019.

[70] M. Adnan, R. AÂ Pinnick, Z. Tang, L. WÂ Taylor, S. SriÂ Pamulapati, G. RoyerÂ Carfagni, and M. Pasquali, "Bending behavior of CNT fibers and their scaling laws," Soft Matter, vol. 14, no. 41, pp. 8284–8292, 2018.

[71] J. Moon, K. Weaver, B. Feng, H. Gi Chae, S. Kumar, J. Baek, and G. P. Peterson, "Note: Thermal conductivity measurement of individual poly(ether ketone)/carbon nanotube fibers using a steady-state dc thermal bridge method," Review of Scientific Instruments, vol. 83, p. 016103, Jan. 2012.

[72] P. L. McEuen and J. Y. Park, "Electron Transport in Single-Walled Carbon Nanotubes," MRS Bulletin, vol. 29, pp. 272–275, Apr. 2004. Publisher: Cambridge University Press.

[73] Y. Bai, R. Zhang, X. Ye, Z. Zhu, H. Xie, B. Shen, D. Cai, B. Liu, C. Zhang, Z. Jia, S. Zhang, X. Li, and F. Wei, "Carbon nanotube bundles with tensile strength over 80 GPa," Nature Nanotechnology, vol. 13, pp. 589–595, July 2018. Number: 7 Publisher: Nature Publishing Group.

[74] S. Iijima and T. Ichihashi, "Single-shell carbon nanotubes of 1-nm diameter," Nature, vol. 363, pp. 603–605, June 1993.

[75] D. T. Colbert, J. Zhang, S. M. McClure, P. Nikolaev, Z. Chen, J. H. Hafner, D. W. Owens, P. G. Kotula, C. B. Carter, J. H. Weaver, A. G. Rinzler, and R. E. Smalley, "Growth and Sintering of Fullerene Nanotubes," Science, vol. 266,

pp. 1218–1222, Nov. 1994. Publisher: American Association for the Advancement of Science Section: Reports.

[76] T. A. Edison, "Electric lamp," Jan. 1880.

[77] J. Swan, "Incandescent Light Bulb," 1881.

[78] R. Bacon, "Growth, Structure, and Properties of Graphite Whiskers," Journal of Applied Physics, vol. 31, pp. 283–290, Feb. 1960.

[79] J. J. Vilatela and A. H. Windle, "Yarn-Like Carbon Nanotube Fibers," Advanced Materials, vol. 22, no. 44, pp. 4959–4963, 2010.

[80] J. Kim, G. Sauti, R. A. Wincheski, R. J. Cano, B. D. Jensen, J. G. Smith, K. E. Wise, and E. J. Siochi, "Undirectional Carbon Nanotube Yarn/Polymer Composites," Technical Report NASA/TM-2018-220081, L-20949, NF1676L-30688, NASA, July 2018.

[81] J. Kim, G. Sauti, R. J. Cano, R. A. Wincheski, J. G. Ratcliffe, M. Czabaj, N. W. Gardner, and E. J. Siochi, "Assessment of carbon nanotube yarns as reinforcement for composite overwrapped pressure vessels," Composites Part A: Applied Science and Manufacturing, vol. 84, pp. 256–265, May 2016.

[82] W. Xie, R. Zhang, R. J. Headrick, L. W. Taylor, S. Kooi, M. Pasquali, S. Müftü, and J.-H. Lee, "Dynamic Strengthening of Carbon Nanotube Fibers under Extreme Mechanical Impulses," Nano Letters, vol. 19, pp. 3519–3526, June 2019. Publisher: American Chemical Society.

[83] E. Oh, H. Cho, J. Kim, J. E. Kim, Y. Yi, J. Choi, H. Lee, Y. H. Im, K.-H. Lee, and W. J. Lee, "Super-Strong Carbon Nanotube Fibers Achieved by

Engineering Gas Flow and Postsynthesis Treatment," <u>ACS Applied Materials & Interfaces</u>, vol. 12, pp. 13107–13115, Mar. 2020. 6.6 N/Tex.

[84] J. D. Buckley and D. D. Edie, <u>Carbon Carbon Materials and Composites</u>. William Andrew, 1993. Google-Books-ID: sqfWSwDdVOMC.

[85] M. Azadi, S. A. Northey, S. H. Ali, and M. Edraki, "Transparency on greenhouse gas emissions from mining to enable climate change mitigation," <u>Nature Geoscience</u>, vol. 13, pp. 100–104, Feb. 2020. Number: 2 Publisher: Nature Publishing Group.

[86] F. Su and M. Miao, "Asymmetric carbon nanotube MnO 2 two ply yarn supercapacitors for wearable electronics," <u>Nanotechnology</u>, vol. 25, no. 13, p. 135401, 2014.

[87] T.-W. Chou, L. Gao, E. T. Thostenson, Z. Zhang, and J.-H. Byun, "An assessment of the science and technology of carbon nanotube-based fibers and composites," <u>Composites Science and Technology</u>, vol. 70, pp. 1–19, Jan. 2010.

[88] N. D. Alexopoulos, C. Bartholome, P. Poulin, and Z. Marioli-Riga, "Damage detection of glass fiber reinforced composites using embedded PVA carbon nanotube (CNT) fibers," <u>Composites Science and Technology</u>, vol. 70, pp. 1733–1741, Oct. 2010.

[89] J. Moma and J. Baloyi, <u>Modified Titanium Dioxide for Photocatalytic Applications</u>. IntechOpen, Nov. 2018. Publication Title: Photocatalysts - Applications and Attributes.

[90] Y. Dong, D. Tang, and C. Li, "Photocatalytic oxidation of methyl orange in

water phase by immobilized TiO2-carbon nanotube nanocomposite photocatalyst," Applied Surface Science, vol. 296, pp. 1–7, Mar. 2014.

[91] E. A. Morris and M. C. Weisenberger, "Solution Spinning of PAN-Based Polymers for Carbon Fiber Precursors," in Polymer Precursor-Derived Carbon, vol. 1173 of ACS Symposium Series, pp. 189–213, American Chemical Society, Jan. 2014. Section: 9.

[92] R. J. Cremlyn, Chlorosulfonic Acid. June 2002.

[93] D. Tanner, J. A. Fitzgerald, and B. R. Phillips, "The Kevlar Story–An Advanced Materials Case Study," Angewandte Chemie, vol. 101, no. 5, pp. 665–670, 1989. _eprint: https://onlinelibrary.wiley.com/doi/pdf/10.1002/ange.19891010539.

[94] F. Mirri, R. Ashkar, V. Jamali, L. Liberman, R. A. Pinnick, P. van der Schoot, Y. Talmon, P. D. Butler, and M. Pasquali, "Quantification of Carbon Nanotube Liquid Crystal Morphology via Neutron Scattering," Macromolecules, vol. 51, pp. 6892–6900, Sept. 2018.

[95] Y. Liu and S. Kumar, "Recent Progress in Fabrication, Structure, and Properties of Carbon Fibers," Polymer Reviews, vol. 52, pp. 234–258, July 2012. Publisher: Taylor & Francis _eprint: https://doi.org/10.1080/15583724.2012.705410.

[96] Z. Yin, M. Jian, C. Wang, K. Xia, Z. Liu, Q. Wang, M. Zhang, H. Wang, X. Liang, X. Liang, Y. Long, X. Yu, and Y. Zhang, "Splash-Resistant and Light-Weight Silk-Sheathed Wires for Textile Electronics," Nano Letters, vol. 18, pp. 7085–7091, Nov. 2018. Publisher: American Chemical Society.

[97] K.-P. Hoffmann and R. Ruff, "Flexible dry surface-electrodes for ECG long-term monitoring," in <u>2007 29th Annual International Conference of the IEEE Engineering in Medicine and Biology Society</u>, pp. 5739–5742, Aug. 2007. ISSN: 1558-4615.

[98] R. Cochran and T. Rosen, "Contact Dermatitis Caused by ECG Electrode Paste," <u>Southern Medical Association</u>, vol. 73, no. 12, pp. 1667–1668, 1980.

[99] W. Uter and H. J. Schwanitz, "Contact dermatitis from propylene glycol in ECG electrode gel," <u>Contact Dermatitis</u>, vol. 34, pp. 230–231, Mar. 1996.

[100] R. J. Coskey, "Contact Dermatitis Caused by ECG Electrode Jelly," <u>Archives of Dermatology</u>, vol. 113, pp. 839–840, June 1977.

[101] A. C. Myers, H. Huang, and Y. Zhu, "Wearable silver nanowire dry electrodes for electrophysiological sensing," <u>RSC Advances</u>, vol. 5, pp. 11627–11632, Jan. 2015.

[102] H.-C. Jung, J.-H. Moon, D.-H. Baek, J.-H. Lee, Y.-Y. Choi, J.-S. Hong, and S.-H. Lee, "CNT/PDMS composite flexible dry electrodes for long-term ECG monitoring," <u>IEEE transactions on bio-medical engineering</u>, vol. 59, pp. 1472–1479, May 2012.

[103] J.-Y. Baek, J.-H. An, J.-M. Choi, K.-S. Park, and S.-H. Lee, "Flexible polymeric dry electrodes for the long-term monitoring of ECG," <u>Sensors and Actuators A: Physical</u>, vol. 143, pp. 423–429, May 2008.

[104] R. Ma, D.-H. Kim, M. McCormick, T. Coleman, and J. Rogers, "A stretchable electrode array for non-invasive, skin-mounted measurement of electrocardiography (ECG), electromyography (EMG) and electroencephalography (EEG),"

in *2010 Annual International Conference of the IEEE Engineering in Medicine and Biology*, pp. 6405–6408, Aug. 2010. ISSN: 1558-4615.

[105] K. Zheng, S. Chen, L. Zhu, J. Zhao, and X. Guo, "Large Area Solution Processed Poly (Dimethylsiloxane)-Based Thin Film Sensor Patch for Wearable Electrocardiogram Detection," *IEEE Electron Device Letters*, vol. 39, pp. 424–427, Mar. 2018.

[106] Y. Yamamoto, D. Yamamoto, M. Takada, H. Naito, T. Arie, S. Akita, and K. Takei, "Efficient Skin Temperature Sensor and Stable Gel-Less Sticky ECG Sensor for a Wearable Flexible Healthcare Patch," *Advanced Healthcare Materials*, vol. 6, no. 17, p. 1700495, 2017.

[107] M. K. Yapici, T. Alkhidir, Y. A. Samad, and K. Liao, "Graphene–clad textile electrodes for electrocardiogram monitoring," *Sensors and Actuators B: Chemical*, vol. 221, pp. 1469–1474, Dec. 2015.

[108] L. Rattfält, F. Björefors, D. Nilsson, X. Wang, P. Norberg, and P. Ask, "Properties of screen printed electrocardiography smartware electrodes investigated in an electro-chemical cell," *BioMedical Engineering OnLine*, vol. 12, p. 64, July 2013.

[109] S. Takamatsu, T. Lonjaret, D. Crisp, J.-M. Badier, G. G. Malliaras, and E. Ismailova, "Direct patterning of organic conductors on knitted textiles for long-term electrocardiography," *Scientific Reports*, vol. 5, p. 15003, Oct. 2015.

[110] S. K. Sinha, Y. Noh, N. Reljin, G. M. Treich, S. Hajeb-Mohammadalipour, Y. Guo, K. H. Chon, and G. A. Sotzing, "Screen–Printed PEDOT:PSS Electrodes on Commercial Finished Textiles for Electrocardiography," *ACS Applied*

Materials & Interfaces, vol. 9, pp. 37524–37528, Nov. 2017.

[111] G. Paul, R. Torah, S. Beeby, and J. Tudor, "The development of screen printed conductive networks on textiles for biopotential monitoring applications," Sensors and Actuators A: Physical, vol. 206, pp. 35–41, Feb. 2014.

[112] C. R. Merritt, H. Troy Nagle, and E. Grant, "Fabric–Based Active Electrode Design and Fabrication for Health Monitoring Clothing," IEEE Transactions on Information Technology in Biomedicine, vol. 13, pp. 274–280, Mar. 2009.

[113] G. Paul, R. Torah, S. Beeby, and J. Tudor, "Novel active electrodes for ECG monitoring on woven textiles fabricated by screen and stencil printing," Sensors and Actuators A: Physical, vol. 221, pp. 60–66, Jan. 2015.

[114] F. Vitale, S. R. Summerson, B. Aazhang, C. Kemere, and M. Pasquali, "Neural Stimulation and Recording with Bidirectional, Soft Carbon Nanotube Fiber Microelectrodes," ACS Nano, vol. 9, pp. 4465–4474, Apr. 2015.

[115] McCauley Mark D., Vitale Flavia, Yan J. Stephen, Young Colin C., Greet Brian, Orecchioni Marco, Perike Srikanth, Elgalad Abdelmotagaly, Coco Julia A., John Mathews, Taylor Doris A., Sampaio Luiz C., Delogu Lucia G., Razavi Mehdi, and Pasquali Matteo, "In Vivo Restoration of Myocardial Conduction With Carbon Nanotube Fibers," Circulation: Arrhythmia and Electrophysiology, vol. 12, p. e007256, Aug. 2019.

[116] J. Wang, R. P. Deo, P. Poulin, and M. Mangey, "Carbon Nanotube Fiber Microelectrodes," Journal of the American Chemical Society, vol. 125, pp. 14706–14707, Dec. 2003. Publisher: American Chemical Society.

[117] J. Di, X. Zhang, Z. Yong, Y. Zhang, D. Li, R. Li, and Q. Li, "Carbon-Nanotube Fibers for Wearable Devices and Smart Textiles," Advanced Materials, vol. 28, no. 47, pp. 10529–10538, 2016. _eprint: https://onlinelibrary.wiley.com/doi/pdf/10.1002/adma.201601186.

[118] J. S. Yan, M. Orecchioni, F. Vitale, J. A. Coco, G. Duret, S. Antonucci, S. S. Pamulapati, L. W. Taylor, O. S. Dewey, M. Di Sante, A. M. Segura, C. Gurcan, F. Di Lisa, A. Yilmazer, M. D. McCauley, J. T. Robinson, M. Razavi, K. Ley, L. G. Delogu, and M. Pasquali, "Biocompatibility studies of macroscopic fibers made from carbon nanotubes: Implications for carbon nanotube macrostructures in biomedical applications," Carbon, vol. 173, pp. 462–476, Mar. 2021.

[119] "U.s. food and drug administration, department of health & human services, dynamic EGG Systems, TLC5000, 1K101273 approval letter," Aug. 2011.